MICROSCOPY

Microscopy, 2021, 75–115
doi:10.1093/jmicro/dfaa070
Advance Access Publication Date: 15 November 2020

Special Issue Paper

Phase plates in the transmission electron microscope: operating principles and applications

Marek Malac[1,2,*], Simon Hettler[3], Misa Hayashida[1], Emi Kano[4], Ray F. Egerton[2] and Marco Beleggia[5]

[1]NRC-NANO, National Research Council, 11421 Saskatchewan Drive, Edmonton, Alberta T6G 2M9, Canada; [2]Department of Physics, University of Alberta, Edmonton, Alberta T6G 2E1, Canada; [3]Laboratorio de Microscopías Avanzadas (LMA), Instituto de Nanociencia y Materiales de Aragon (INMA), Universidad de Zaragoza, Campus Río Ebro, 50018 Zaragoza, España; [4]Institute of Materials and Systems for Sustainability, Nagoya University, Nagoya, Aichi 464-8601, Japan, and [5]DTU Nanolab, Technical University of Denmark, 2800 Kgs. Lyngby, Denmark

*To whom correspondence should be addressed. E-mail: marek.malac@nrc-cnrc.gc.ca/mmalac@ualberta.ca

Received 14 July 2020; Revised 30 October 2020; Editorial Decision 2 November 2020; Accepted 11 December 2020

Abstract

In this paper, we review the current state of phase plate imaging in a transmission electron microscope. We focus especially on the hole-free phase plate design, also referred to as the Volta phase plate. We discuss the implementation, operating principles and applications of phase plate imaging. We provide an imaging theory that accounts for inelastic scattering in both the sample and in the hole-free phase plate.

Key words: hole-free phase plate (HFPP), Volta phase plate (VPP), radiation damage, electron beam-induced sample charging, sample contamination, cryo electron microscopy

Acronyms

λ	electron wavelength
λ_e	elastic mean free path
λ_i	inelastic mean free path
λ_t	total mean free path
q	scattering vector in spatial frequency units [nm^{-1}]
BFP	back focal plane
BFTEM	bright field transmission electron microscopy
CL	condenser lens
CTF	contrast transfer function
DLR	dose-limited resolution
EH	electron holography
HFPP	hole-free phase plate
MIP	mean inner potential, V_0
MTC	mass thickness contrast
OA	objective aperture
OL	objective lens
PCTF	phase- contrast transfer function
SAA	selected area aperture
SE	secondary electron. SE_α propagating in vacuum outside sample. SE_β propagating within sample
SPO	strong phase object
VPP	Volta phase plate
WPO	weak phase object
ZPP	Zernike phase plate

Introduction

Our objective is to provide readers with an overview of the present understanding of the principles and applications involved in phase plate (PP) imaging in a transmission electron microscope (TEM). After an introduction to PP theory, we review the large variety of PP designs and then focus on the hole-free phase late (HFPP) [1–3], sometimes referred to as the Volta phase plate (VPP) [4–7].

Phase plates are electron-optical elements placed in the beam path to modulate the phase of the electron wave. Their primary function is to increase the contrast when imaging weak phase objects (WPOs), thereby reducing the irradiation damage needed to detect these objects [1,8,9]. The need for improved phase-contrast transfer in electron microscopy has long been recognized and is based on the work of Zernike in the field of light microscopy [10]. In 1947, Hans Börsch proposed methods for phase-contrast enhancement in a TEM [11] that already encompassed the two main PP types in use nowadays: thin-film-based and electrostatic PPs. The improved phase-contrast transfer is achieved by placing a phase-shifting device (PP) in the back focal plane (BFP) of the objective lens, or in a conjugated diffraction plane [12]. The device then applies a phase shift between the direct beam ($q = 0$) and diffracted beams at $q > 0$. Here, q is the scattering vector corresponding to a spatial frequency in nm^{-1} units. Early experimental work on the realization of such a PP mainly explored the possibility of placing an amorphous carbon (*a*C) film in the BFP [13–15]. Unwin proposed the use of a spider thread [16]. The ideas of Börsch were further pursued by Tonomura's group [17]. An overview of early PP attempts can be found in [18].

Artifacts introduced by those early PPs spoiled their beneficial phase-contrast enhancement. Advances in microstructuring techniques, especially the focused ion beam technique, finally led to the first PP that made an impact in the community at the turn of the last century. The implementation of a thin aC film with a small hole in the BFP is very similar to the proposal of Zernike and thus has been termed the Zernike phase plate (ZPP) [19]. Its success enticed researchers to investigate other kinds of phase-shifting devices that include the electrostatic Börsch-PP [20–26] and its derivatives [27,28] as well as other more exotic types [29–31]. In addition to thin-film and electrostatic devices, PPs that exploit other means of interactions, e.g. light-electron or magnetic fields, have been proposed [31,32]. Despite the variety of different PP types, their widespread success was inhibited by problems, including contamination and spurious charging, film aging, undesirable obstruction of electrons in the BFP, image artifacts caused by sharp phase jumps, complex fabrication processes and extensive modifications of the electron-optical system. Many of these problems are solved by the HFPP design, consisting of a uniform thin film in which the necessary relative phase shift is created by the direct beam itself [1,4].

The primary goal of PPs is to increase image contrast at low spatial frequencies [8,33]. PPs do not provide an increase in the ultimate spatial resolution of an instrument. On the other hand, when correctly implemented, they do not have a detrimental effect on high-resolution information transfer. The image formation process in a TEM can be understood as interference between the direct beam, containing the unscattered part of the electron wave (in the vicinity of $q = 0$), and the portion of the electron wave scattered elastically by the sample within a certain angular range ($q > 0$). Image contrast arises when the interference between the scattered and unscattered electrons is controlled and suitably tuned by the action of a PP.

This review is divided into seven main sections. We first present a theory of PP imaging in Section 'A brief theory of phase plate imaging,' before providing an overview of the variety of PP design (Section 'Hole-free phase plate implementation') being considered or implemented. In the following sections, we focus on a particular PP design that utilizes an uniform thin film modified by the high-energy electron beam itself: the HFPP [1]. The same design was reported later and referred to as the VPP [4]. In the text below, we use the terms 'HFPP' and 'VPP' interchangeably.

While originally demonstrated on organic samples [1,3], HFPPs have also been used to image interfaces in radiation-sensitive samples for material science and to image magnetic and electric fields in-focus, etc. The latter is of interest when relating the sample microstructure to its magnetic properties.

HFPPs have been successfully utilized for electron tomographic imaging [34,35], providing sufficient stability and reproducibility [35]. In contrast to electron holography (EH), PPs should not be considered *quantitative* tools, because the image contrast cannot be related to the object phase shift in a straightforward manner. However, recent progress indicates that in the case of a WPO, phase information from the sample can be extracted quantitatively [36]. Furthermore, a *strong phase object* that contains discrete spatial frequencies allows the quantitative PP imaging extraction of *both* the phase shift of the object and the phase shift at the HFPP [37]. While contrast quantification using HFPP images is currently challenging, the ease of operation, ability to image a large field of view and the possibility of observing dynamic changes in the sample are all beneficial.

A brief theory of PP imaging

We begin by giving a brief survey of the electron–matter interactions relevant to PP imaging. Fig. 1 illustrates schematically the two types of electron interactions within the sample: elastic and inelastic. Arising from electron-nucleus scattering, elastic interactions change the momentum, and hence the phase, of an incident electron without significantly affecting its kinetic energy; inelastic interactions, arising from electron–electron scattering, result in a significant energy transfer between the incident electron and the sample and hence a loss of coherence. Since PP imaging belongs to the family of coherent imaging techniques, elastic interactions are more relevant. In this paper, we discuss specifically the optimization of image contrast C arising from elastic interactions. We refer to the sample-induced elastic contrast as the *phase contrast* and to the elastically scattered electron intensity as 'I_e'.

Scattering and wave amplitudes

In this section, we introduce aspects of imaging theory that are applicable to PP imaging and briefly summarize the discussion in previous papers [1,37,38], which all adopt the same sign convention in [39, p. 71], that we use here. In particular, the incident electron plane wave is taken as $e^{\mathrm{i}k_z z}$ with the phase shift of the electron wave increasing along the direction of electron propagation z. The amplitude of the incident plane wave is related to the beam current density, i.e. the number of electrons per unit area and time propagating along the optic axis. Assuming a circular illumination patch of radius R_{ill}, denoting I_p the primary beam current, and choosing a Cartesian reference system with the x- and y-axes on the sample and the z-axis along the beam propagation direction (i.e. pointing 'down' from the source to the detector), we can define the incident electron wave as

$$\psi_{ill}(x,y,z) = a_0\, e^{\mathrm{i}k_z z}, \quad \text{for} \quad r = \sqrt{x^2+y^2} < R_{ill}, \tag{1}$$

where $k_z = 2\pi/\lambda$ is the wave number. The de Broglie electron wavelength $\lambda = h/p = \lambda_C/\gamma\beta$, where $\lambda_C = h/mc = 2.426\,\mathrm{pm}$ is the Compton wavelength, depends on the accelerating voltage U via the relativistic factor $\gamma = \sqrt{1-\beta^2} = 1 + eU/mc^2$. Some values of λ at various accelerating voltages are shown in Table 1. Above m is the electron mass, c is the speed of light in vacuum and e is the electron charge.

The wave amplitude a_0 is related to the beam current density (or electron flux) $J_p = I_p/\pi R_{ill}^2$ via $a_0^2 = J_p/ev$ [39], with

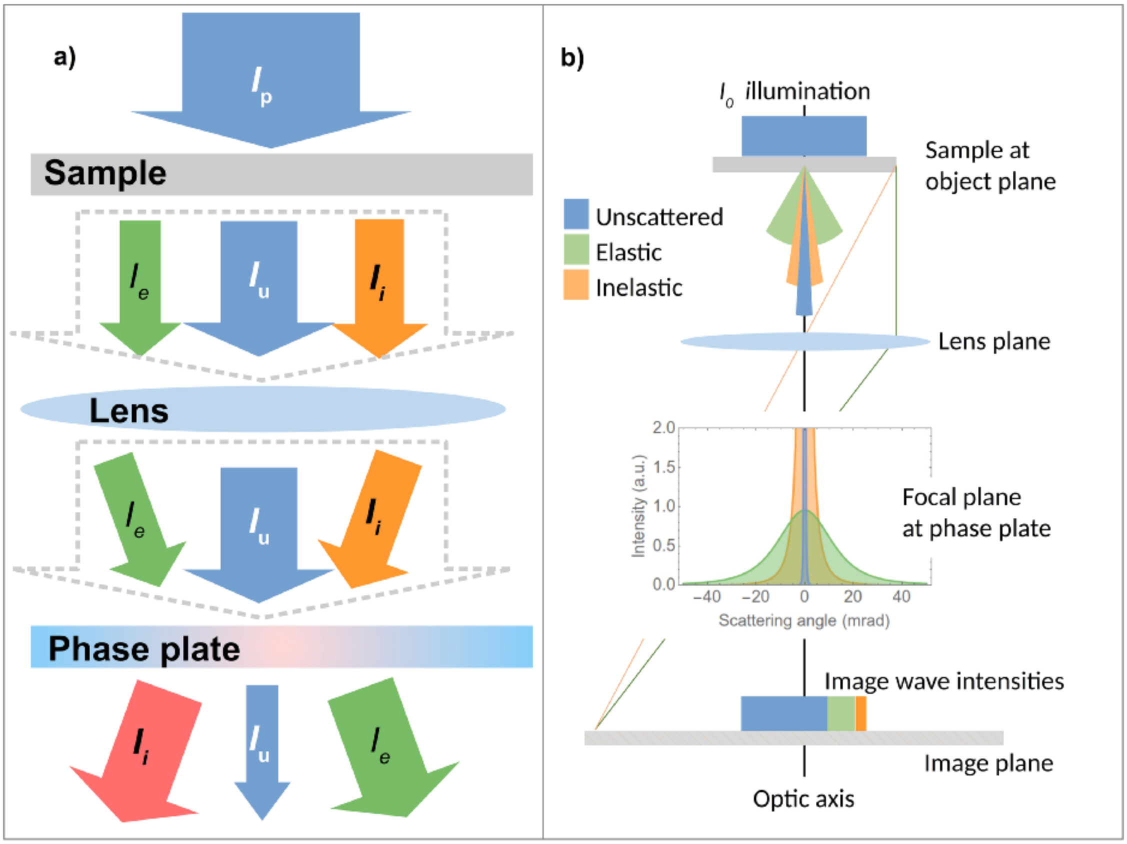

Fig. 1. Schematic of various electron–solid interactions and the corresponding channels for a transmission electron microscope column with two planes containing scattering objects: a sample and a phase plate in (a). (b) qualitatively illustrates the angular distribution for the sample. The outcome of the primary beam I_p elastic I_e and inelastic I_i interactions is indicated in (b) and the unscatttered beam I_u impinge onto the phase plate. At the phase plate, elastic and inelastic interactions further decrease the unscattered intensity I_u and increase the elastically scattered channel I_e and inelastically scattered channel I_i. The mean energy loss due to inelastic scattering further increases after the phase plate as compared to the sample only, as indicated by the I_i arrow becoming darker red after phase plate than after the sample alone. The elastic scattered intensity includes both the phase shift changes arising from the mean inner potential variations in the sample and phase plate as well as the interactions with electric and magnetic fields in the vacuum *outside* the sample and the phase plate. The gray dashed arrows indicate that, in the absence of beam intersecting hardware, all electrons that passed through the sample also pass through the phase plate.

Table 1. Values of the electron velocity β, relativistic factor γ, wavelength λ, phase pre-factor C_E and beam electron density a_0^2 at various accelerating voltages.

U (kV)	β	γ	λ (pm)	C_E (rad/V µm)	a_0^2 (10^{13} m^{-3})
20	0.272	1.04	8.59	18.6	12.3
100	0.548	1.20	3.70	9.24	6.08
200	0.695	1.39	2.51	7.29	4.80
300	0.777	1.59	1.97	6.53	4.29
1000	0.941	2.96	0.872	5.39	3.54
5000	0.996	10.8	0.226	5.09	3.35

The last entry is calculated for a beam current density of 1.6 kA/m^2, corresponding to 100 electrons per square Angstrom per second, which is a reasonable dose rate for TEM imaging in materials science. In biological sciences, the beam current density is 10× to 100× lower.

$v = \beta c = c\sqrt{1-\gamma^{-2}}$ the electron velocity. The chosen normalization for the wave function reflects the number density of electrons within the beam at any given time. The total number of electrons crossing a given plane perpendicular to the optic axis per unit time, i.e. the beam current, is

$$I_p = ev\int |\psi(x,y,z)|^2 \mathrm{d}x\mathrm{d}y \tag{2}$$

and reflects the charge conservation along the beam path. This condition is violated only by hard apertures removing electrons from the beam, as the capture cross section for high-energy electrons is negligible.

The coherent electron wave emerging from the sample after undergoing elastic interactions is termed interchangeably the exit wave or object wave and is represented by its amplitude a and phase $\varphi(x,y)$ as

$$\psi_o(x,y,z) = a e^{\mathrm{i}\varphi(x,y)} e^{\mathrm{i}k_z z} \tag{3}$$

where

$$\varphi(x,y) = C_E \int V(x,y,z)\mathrm{d}z \tag{4}$$

is proportional to the electrostatic potential $V(x,y,z)$ of the sample projected along z, generated by the totality of charges present within and around it, including mobile and immobile charges, nuclei, electrons, ions, polarization charges, charges on nearby electrodes, etc.[1]

---

[1] Here, we do not consider a multi-slice setup and work within the phase object approximation. This is warranted for thin samples composed of light elements (H, C, O).

The proportionality factor C_E is acceleration–voltage-dependent and can be written as

$$C_E = \frac{e}{\hbar v} \tag{5}$$

Some values of C_E at various accelerating voltages are shown in Table 1. The asymptotic limit of C_E for ultra-relativistic electrons with $eU >> mc^2 = 511$ keV is $C_E[\infty]$=5.07 rad/V µm. The existence of a lower bound for C_E but not for λ suggests that ultra-relativistic coherent imaging might be advantageous.[2]

The amplitude term a accounts for the number of elastically scattered electrons contributing to the coherent image formation. If we ignore inelastic scattering, then $a = a_0$. If we take inelastic scattering into consideration, then $a < a_0$ in proportion to the square root of the total elastic and inelastic cross sections of the object. In particular, the total elastic and inelastic currents are $I_e = J_P\sigma_e$ and $I_i = J_P\sigma_i$, where σ_e and σ_i are the total elastic and inelastic cross sections, respectively. This implies that the unscattered current is $I_u = J_P(\pi R_{ill}^2 - \sigma_e - \sigma_i)$. We define the coherent intensity as $I_c = I_u + I_e$.

Accounting for the electrons transferred from the elastic to the inelastic channel in a single-scattering approximation leads to an evaluation of the coherent amplitude as follows

$$\frac{I_c}{I_0} = \frac{a^2}{a_0^2} = \frac{\lambda_t}{\lambda_e} + \frac{\lambda_t}{\lambda_i} e^{-\frac{t}{\lambda_t}} \tag{6}$$

where λ_t is the total mean free path, $\lambda_{e,i} = 1/n\sigma_{e,i}$ are the elastic λ_e and inelastic λ_i mean free paths, respectively, $1/\lambda_t = 1/\lambda_e + 1/\lambda_i$, and n is the number density of atoms or molecules with cross sections $\sigma_{e,i}$ within a sample of thickness t. At this stage, neither apertures nor the angular distribution of scattering play a role. After we introduce the concept of phase contrast (Section 'Phase contrast'), we will revisit the coherent amplitude loss described by Eq. (6) to illustrate how it leads to a loss of signal.

Figure 1 schematically depicts the transfer of intensity between the three channels as the electrons cross the sample and a generic PP positioned in the focal plane of the optical setup.

Image formation

In electron microscopy we measure the intensity of the electron wave ψ_i (termed the 'image wave') reaching the detector, which is generally placed at a conjugate object plane. We use as definition of intensity the number of electrons e^- per unit area of the detector per unit time [39]. Assuming unit magnification, and a perfect imaging system, the image wave is then an identical copy of the object wave, Eq. (3) so the recorded intensity is

$$I = ev|\psi_i|^2 = eva^2 \quad \text{for} \quad r < R_{ill} \tag{7}$$

as neither of the phase terms yields visible contrast.

An electron microscope, however, is not a perfect imaging system. Aberrations of the imaging lens as well as apertures in the beam paths and the partial spatial and temporal coherence of the beam must be taken into account via the transfer function concept. The transfer function is the microscope point spread function in reciprocal representation and describes in a concise manner how the object wave is modified by the imperfections of the imaging system, becoming the image wave at the detector plane. Its canonical form is [39,38]

$$T(\mathbf{q}) = A(\mathbf{q})e^{\mathrm{i}W(\mathbf{q})}e^{-D(\mathbf{q})} \tag{8}$$

where $A(\mathbf{q})$ is a pupil function representing an angle-limiting aperture (usually the objective aperture) and $W(\mathbf{q})$ is the aberration function defined as

$$W(\mathbf{q}) = \pi Z\lambda q^2 - \frac{\pi}{2}C_S\lambda^3 q^4. \tag{9}$$

In Eq. (9), C_S is the spherical aberration coefficient, Z is the defocus parameter and $D(\mathbf{q})$ is the damping envelope defined as

$$D(\mathbf{q}) = \frac{\pi^2\theta_{ill}}{\log 2}\left(Zq + C_S\lambda^2 q^3\right)^2 + \frac{1}{2}\left(\pi\Delta\lambda q^2\right)^2 \tag{10}$$

with θ_{ill} the angular spread of the illumination,

$$\Delta = \frac{\gamma}{\gamma + 1}C_C\delta \tag{11}$$

where C_C is the chromatic aberration coefficient, and the numerical factor δ represents the various relative instabilities of the microscope such as energy spread, high-tension fluctuations, etc. The aberration function $W(\mathbf{q})$ represents the additional phase shift experienced by the electron wave due to spherical aberration and defocus. A negative defocus, corresponding to an overfocus, adds in the same way as a spherical aberration: both add a negative (convergent) phase shift to the electron wave with respect to the direct beam at $q = 0$.

The reciprocal plane coordinate system $\mathbf{q} = (q_x, q_y)$ is defined according to the chosen convention for Fourier transforms (FFTs) [39]

$$\tilde{\psi}(\mathbf{q}) = \int \psi(\mathbf{r})e^{2\pi \mathrm{i}\mathbf{q}\cdot\mathbf{r}}\mathrm{d}^2\mathbf{r} \tag{12}$$

$$\psi(\mathbf{r}) = \int \tilde{\psi}(\mathbf{q})e^{-2\pi \mathrm{i}\mathbf{q}\cdot\mathbf{r}}\mathrm{d}^2\mathbf{q} \tag{13}$$

The transfer function acts as a Fourier filter, affecting the phase and amplitude of the object wave spectrum and establishes the relation between object and image wave as follows:

$$\psi_i(\mathbf{r}) = \mathcal{F}^{-1}\left[T(\mathbf{q})\mathcal{F}\left[\psi_o(\mathbf{r})\right]\right] \tag{14}$$

where $\mathcal{F}$ denotes the FFT operator.

A PP located in the diffraction plane introduces an additional phase term $P(\mathbf{q})$ in the transfer function, which, neglecting damping and apertures, and assuming circular symmetry, becomes

$$T(q) = e^{\mathrm{i}W(q)}e^{\mathrm{i}P(q)}. \tag{15}$$

The phase profile of the plate reflects its design. For example, a ZPP with a hole of radius q_c at the center of a thin film of thickness t and mean inner potential (MIP) V_0, providing a phase shift

$$\phi_Z = C_E V_0 t \tag{16}$$

adds a piecewise continuous phase term to the transfer function

$$P_Z(q) = 1 \quad \text{for} \quad q < q_c \tag{17}$$

representing no effect on the electrons through the hole, and

$$P_Z(q) = e^{\mathrm{i}\phi_Z} \quad \text{for} \quad q > q_c, \tag{18}$$

representing the constant and uniform phase shift added to all other electrons crossing the film.

---

[2] Resolution continues to improve indefinitely with increasing energy, while the loss of signal represented by the drop of C_E with energy stops, which means that the resolution keeps increasing, while the signal stops decreasing.

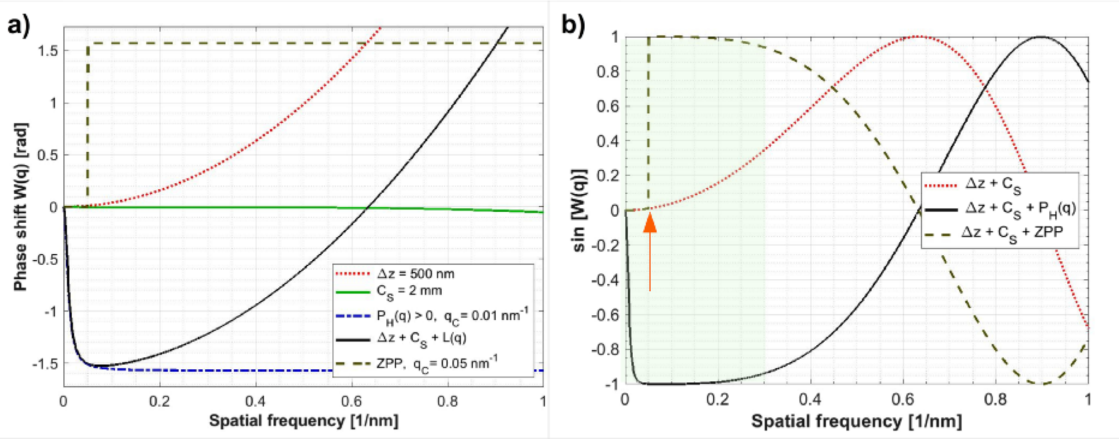

Fig. 2. (a) Wavefront phase shift arising from underfocus $\Delta z = 500$ nm (red dotted) spherical aberration with $C_S = 2$ mm (green solid), Lorentzian phase shift $P_H(q)$ with cut on frequency $q_c = 0.01\ \text{nm}^{-1}$ representing a hole-free phase plate with a positive beam-induced charge screened by distributed negative charges (blue dash-dot), underfocus $\Delta z = 500$ nm combined with $P_H(q)$ (black solid) and thin film type Zernike phase plate also with $q_c = 0.05\ \text{nm}^{-1}$ (brown dashed with cut on frequency marked by a red arrow). (b) Corresponding weak phase object phase-contrast transfer function $\sin(W(q))$. The green shaded area in (b) approximately indicates the region referred to as low spatial frequencies in this paper, see also [8]. All calculations were performed at $U = 200$ kV, adapted from [38] based on model B in [1].

The contribution $P_H(q)$ to the transfer function from a HFPP, where the beam-induced charge redistribution under the direct beam plays the role of the Zernike central aperture, may be approximated by a generic bell-shaped curve. We choose for convenience to describe the phase profile of a HFPP with a Lorenzian function of halfwidth q_c [1,38]

$$P_H(q) = \frac{\phi_H}{1 + \frac{q^2}{q_c^2}} - \phi_H \tag{19}$$

where ϕ_H is the net phase difference between $q = 0$ and $q \to \infty$ and has the same sign of the charge/potential developed on the HFPP that is responsible for its functionality: positive charge/potential gives a positive ϕ_H, which results in a negative phase shift with convergent action. To ensure consistency of the WPO approximation, we have added the $-\phi_H$ phase offset to ensure that $P_H(0) = 0$ [38].

The effect of the various terms in the transfer function, including the PP, is graphically shown in Fig. 2.

Figure 2b illustrates that at low spatial frequencies, transfer is poor in BFTEM and improves when a PP is added to the microscope optics. The region where PPs provide better transfer and where most scattering power is contained for most samples is indicated by the green shaded area in (b) [8]. The extent of the low spatial frequencies transfer region depends on a particular PP implementation but typically goes at least to $q = 0.3\ \text{nm}^{-1}$ or more. With a ZPP, the onset of the improved transfer is at q_C corresponding to the ZPP hole size in reciprocal space [8], $0.05\ \text{nm}^{-1}$ used in Fig. 2b as marked by a red arrow. For HFPPs, the onset is gradual from $q = 0\ \text{nm}^{-1}$.

Figure 2 shows that up to the spatial frequency q_C corresponding to the edge of the ZPP, the contrast transfer is identical with BFTEM in a microscope equipped with ZPP. As discussed in Sections 'Hole-free phase plate implementation' and 'A brief theory of phase plate imaging' it is desirable to avoid PP implementations that have a sharp onset, which are not matched to beam size in Fourier space or that block part of the beam. An ideal PP would not only produce a phase shift between the direct and diffracted beams but would also have a phase shift profile that compensates for C_S at a broad range of spatial frequencies. That implies that a PP should not be a step function, but have tails proportional to $C_S q^4$, assuming that the Zq^2 term can be eliminated by remaining in-focus at $Z = 0$.

To ensure the clarity of the rest of the paper and to ease comparisons with the literature, it is necessary to define the terminology when referring to the advancing or retarding phase or aberrations, the advancing or retarding electron wavefront and the reference point for phase shift $\varphi(\mathbf{q})$. In agreement with [38,39], we use the conventions shown in Table 2.

It is interesting to note that PPs also provide contrast enhancement in instruments equipped with a LaB_6 electron source that have a small lateral coherence length of the electron beam. The origin of the phase contrast in LaB_6 microscopes can be understood in the context of building the image from individual electrons, each representing a wave that has its own phase affected by the PP. The resulting image is the sum of the partially coherent electron waves that provide a contrast-enhanced image as discussed in [40]. As compared to an image acquired in a microscope with a field emission source, a phase-contrast image from a LaB_6 microscope is expected to show less contrast due to its lower partial coherence [40].

Phase contrast

To illustrate how phase contrast arises with a PP, we consider the scenario discussed in [41] where a pure phase object (we set the coherent amplitude $a = \sqrt{I_c}$ of the wave to unity) is imaged in-focus $(Z = 0)$ with a non-aberrated lens $(C_S = 0)$ and an ideal ZPP. The object wave is

$$\psi_o(\mathbf{r}) = e^{i\varphi(\mathbf{r})} = 1 + \left(e^{i\varphi(\mathbf{r})} - 1\right) \tag{20}$$

and its spectrum is

$$\tilde{\psi}_o(\mathbf{q}) = \delta^2(\mathbf{q}) + \mathcal{F}\left[e^{i\varphi(\mathbf{r})} - 1\right] \tag{21}$$

Assuming that the hole is 'small enough', a statement that can be formalized by the requirement $q_c << 1/d$, where d represents the size of the object, and the ZPP leaves the central delta representing the

Table 2. Contribution to contrast transfer and the shape of terms contributing to aberration function W(q) according to the convention in [39]. The second column indicates the shape of the individual terms. Here, *U* character indicates a U-shaped contribution when plotted as a function of q, i.e. the aberration function W($q>0$) is higher than W(q=0) and the phase at $q>0$ is retarded relative to the phase at q=0. The ∩ character indicates a term that contributes contrary to the U-shaped term, i.e. W($q>0$) is lower than W(q=0) and the phase at $q>0$ is advanced relative to phase at q=0. The third column indicates whether the phase shift at $q>0$ is positive (advanced) or negative (retarded) relative to the wave front phase at q=0. The fourth column indicates the bright or dark appearance of a positive potential object (such as an atom) imaged using only the term indicated in the first column. The last column clarifies the designation of positive and negative phase contrast. Adapted from [38].

	Shape of the phase shift term	Phase shift sign at q>0 relative to phase shift at q=0	Image appearance for positive potential object such as an atom	Phase contrast designation
Spherical aberration, C_s	∩	−	Bright	Negative
Overfocus, objective lens stronger than for in-focus image	∩	−	Bright	Negative
Underfocus, objective lens weaker than for in-focus image	∪	+	Dark	Positive
HFPP+ phase plate with *positive* patch of beam generated phase	∩	−	Bright	Negative
HFPP- phase plate with *negative* patch of beam generated phase	∪	+	Dark	Positive
Thin film type ZPP with hole	∪	+	Dark	Positive
Mass thickness (scattering) bright field TEM contrast	Not applicable	Not applicable	Not applicable	Positive

unperturbed direct beam. The rest of the spectrum is phase-shifted by ϕ_Z. Therefore, the image spectrum is

$$\tilde{\psi}_i(\mathbf{q}) = \delta^2(\mathbf{q}) + e^{i\phi_Z}\mathcal{F}\left[e^{i\varphi(\mathbf{r})} - 1\right] \tag{22}$$

which by inverse Fourier transformation yields the image wave

$$\psi_i(\mathbf{r}) = 1 + e^{i\phi_Z}\left(e^{i\varphi(\mathbf{r})} - 1\right) \tag{23}$$

The image intensity is then

$$I(\mathbf{r},\phi_Z) = 3 - 2\cos\phi_Z - 2\cos\varphi(\mathbf{r}) + 2\cos\left(\phi_Z + \varphi(\mathbf{r})\right) \tag{24}$$

showing that in the presence of a ZPP the object phase becomes observable as intensity modulation or contrast. Note, however, that the image intensity is not linearly related to the object phase, which may lead to potential misinterpretations of the image contrast from a generic strong phase object. For example, while a maximum in phase always corresponds to either a maximum or a minimum of the intensity (depending on the sign of ϕ_Z), there can be many intensity maxima or minima, i.e. fringes, that do not correspond to phase extrema. This can be seen by noting that

$$\nabla I(\mathbf{r},\phi_Z) = 2\nabla\varphi(\mathbf{r})\left(\sin\varphi(\mathbf{r}) - \sin(\phi_Z + \varphi(\mathbf{r}))\right) \tag{25}$$

vanishes wherever $\nabla\varphi(\mathbf{r})$ does; and, at all points that satisfy

$$\sin\varphi(\mathbf{r}) = \sin(\phi_Z + \varphi(\mathbf{r})) \tag{26}$$

or

$$\varphi(\mathbf{r}) = k\pi + \frac{\pi}{2} - \phi_Z \tag{27}$$

with k any integer number. Eq. (27) reveals that fringes appear in the image following the isophase contours spaced by π. As an illustrative example, we consider the phase object $\varphi(x) = C_E V_0 x \tan\alpha$ representing a wedge of angle α, which is imaged with a PP as a sinusoid of periodicity $2\pi/C_E V_0 \tan\alpha$: for every π of phase shift, a max or a min of intensity develops indicating a thickness variation of $\pi/C_E V_0$. This is the phase contrast equivalent of thickness fringes in diffraction contrast and allows quantitative thickness profiling, although with poor sensitivity of about 50 nm at 300 kV and $V_0 = 10\,\mathrm{V}$.

If the PP thickness is chosen such that $\phi_Z = \pi/2$ and assuming that the object phase is smaller than $\pi/4$ (WPO approximation), Eq. (24) simplifies to

$$I(\mathbf{r},\pi/2) = 1 - 2\varphi(\mathbf{r}) \tag{28}$$

showing the best possible form of phase contrast, where the intensity is linearly proportional to the object phase, and the factor of 2 provides a 2-fold phase amplification.

Influence of inelastic scattering on image contrast

The reduction in coherent amplitude leads to a loss in phase contrast. Suppose we are imaging the edge of a thin-film sample. The part of the electron wave traveling through the vacuum, say $x<0$, has an amplitude a_0 and a constant phase, which we take as zero. The electrons at $x>0$ crossing the sample experience a phase shift ϕ_Z from thickness, Eq. (16), and at the same time a coherent amplitude reduction as in Eq. (6). Therefore, the exit wave can be written as

$$\begin{aligned}\psi_o(x) &= a_0 \quad \text{for} \quad x<0\\ &= ae^{i\phi_Z} + \Sigma\psi_{\text{in}} \quad \text{for} \quad x>0\end{aligned} \tag{29}$$

where $\Sigma\psi_{\text{in}}$ represents the totality of inelastic waves emerging from the sample, whose amplitudes sum incoherently up to the total intensity I_i. The coherent portion, instead, has $a^2 = I_u + I_e = I_c$. Without PP or apertures, there is no contrast between the vacuum and the sample: inelastic electrons reach the detector (perhaps with some defocus) and add I_i to the measured intensity; elastic electrons, not filtered out by any aperture, contribute with I_c; and in total, we have $I_c + I_i = I_0$ on the sample and I_0 in the vacuum, i.e. no contrast.

With an ideal PP and WPO, we would record the following on the detector

$$\begin{aligned} I(x) &= I_0 \quad \text{for} \quad x<0 \\ &= I_c(1-2\phi_Z)+I_i = I_0 - 2\phi_Z I_c \quad \text{for} \quad x>0 \end{aligned} \tag{30}$$

which gives a phase contrast ${}^pC = \phi_Z I_c/I_0$, where I_c/I_0 is given by Eq. (6). Since $I_c = I_0 - I_i$, we conclude that every electron in the inelastic channel decreases phase contrast.

It is worthwhile noting that mass thickness contrast (MTC), which originates from the removal of some beam electrons with an aperture, is primarily established by a loss of coherent electrons. In fact, generally, the apertures used to produce MTC are large enough to leave I_u and I_i untouched, and affect mainly I_e. Naming f the fraction of elastic electrons intercepted by an aperture, a quantity that can be easily related to its size and to the angular distribution of elastic scattering, MTC can be described by

$$\begin{aligned} I(x) &= I_0 \quad \text{for} \quad x<0 \\ &= I_u + (1-f)I_e + I_i = I_0 - fI_e \quad \text{for} \quad x>0 \end{aligned} \tag{31}$$

giving ${}^aC = \frac{1}{2}fI_e/I_0$, which, since $I_e = I_0 - I_u - I_i$ is maximal for $I_i = 0$, once again illustrates the detrimental role of inelastic scattering in image contrast and explains the benefit of zero-loss filtering.

Implementation of PP imaging

In this section, we first discuss the criteria that a PP should fulfill for a successful implementation. Following this, we discuss the possible types of PPs that have been proposed or realized, grouping them mainly in thin-film based, electrostatic and beam-induced approaches. Further concepts are also explored in the discussion.

Requirements for successful PP implementation

To achieve broad impact, a particular PP implementation either has to be convenient to implement and operate or it has to provide such a significant improvement that it motivates users to put considerable effort into its use. The PP implementation should also satisfy as many as possible of the criteria below.

1. Minimization of PP hardware
   - Conserve the transfer of all spatial frequencies
     Placing PP hardware in the BFP of a lens can result in the obstruction of electrons leading to missing (radial or azimuthal) ranges of spatial frequencies. If a radial range of spatial frequencies is blocked, e.g. by the annular shape of a Börsch PP [8,21], those spatial frequencies will be missing in the image giving rise to artifacts. Additionally, if the PP hardware lacks radial symmetry, for example from support arms of a Börsch lens, single-sideband contrast occurs (see also next item).
   - Leave sample symmetry unaltered
     The PP hardware should be such that it does not block or affect particular directions in the BFP. Hardware that is not centrosymmetric around the direct beam at $q = 0$ results in images that do not, in general, reflect the symmetry of the sample. Moreover, the location of features in the image can be displaced and distorted.
   - Avoid electron scattering in transparent parts
     Although they do not obstruct electrons, electron beam transparent objects in the BFP lead to electron scattering. Electrons scattered at the BFP will not contribute to phase contrast but will either form part of the background of the image or may even be taken out of the image formation process by apertures if scattered to high angles (see Section ‘A brief theory of phase plate imaging’).
   - Minimize necessary imaging dose
     Any effect of the PP that goes beyond phase shifting will increase the necessary dose to image the sample. This is evident for obstructing PP parts and is true as well for electrons scattered in the PP that either reduce the contrast (if they contribute to the image background intensity) or increase the necessary dose on the sample if scattered to such high angles that they are intercepted by microscope hardware and do not reach the camera.
2. Optimum spatial phase shift distribution
   - PP should be accurately centered relative to the direct beam at $q = 0$
     This can be done either by utilizing a self-centering method, such as a HFPP, in which the PP center is determined by the position of the direct beam on a pristine film or by the mechanical or electron-optical alignment of the direct beam relative to a pre-existing hardware or hole in a film. Lateral drift has to be kept to a minimum for any PP device.
   - A sharp onset of the phase shift should be avoided
     A sharp onset, i.e. step function-like, of the phase shift at a particular *cut on* spatial frequency q_C results in contrast ringing artifacts in the image. Moreover, the phase-contrast transfer between $q = 0$ and the PP onset spatial frequency q_C is identical to that of bright field transmission electron microscopy imaging, maintaining the poor phase contrast of bright field transmission electron microscopy. Therefore, a smooth phase profile starting at $q = 0$ is preferable.
   - The phase shift profile should be closely matched to the beam profile.
     The ideal phase shift profile is smooth and commensurate with the beam size in the plane of the PP. This typically coincides with the BFP where the beam size is determined by the angular width of the incident beam and the focal length of the objective lens. It is possible to place the PP hardware at any plane in the microscope column that is conjugate with the BFP of the objective lens, i.e. with the Fourier plane of the image.
   - Absence of additional phase shifts
     Additional phase shifts, e.g. those caused by electrostatic charging or contamination, should be avoided. Although this aspect is evident, we mention it here because some types of PPs can be prone to these spurious effects in varying degrees.
3. Optimum sign and amount of the phase shift distribution
   - Adjustable phase shift
     For many samples, the ability to adjust the phase shift to maximize the phase-contrast transfer for a particular sample can be advantageous. An adjustable phase shift also allows for different electron beam energies. Furthermore, the ability to alter the PP-induced phase shifts during an experiment could make it possible to eliminate gaps in the phase-contrast transfer function. The acquisition of multiple images with varying phase shift paves the way for object wave reconstruction [42] (see Section ‘Object-wave reconstruction using phase plates’).
   - Suitable polarity of the phase shift
     Depending on its sign, the phase shift of the PP can either add to the MTC (see Table 2) or it can act in the opposite

Table 3. Overview of different phase plate designs grouped as thin-film based phase plates, electrostatic phase plates, beam-induced phase plates, further phase plate concepts and obstructing devices. The advantage sand drawbacks of the individual concepts are depicted by icons and a red + indicates more pronounced effects. For less common PPs we aimed for a complete literature reference list: for the Zernike and HFPP charge types the huge number of publications makes it impracticable. Pictogram legend: (a) PP needs alignment, (b) scattering in PP, (c)obstruction by PP, (d) complicated PP symmetry, (e) sharp phase cut on, (f) smooth phase profile, (g) adjustable phase shift, (h) TEM modification needed, (i)complex fabrication,(j) missing experimental results.

PP family	PP type	Advantages	Drawbacks	Ref.
Thin-film based PPs	Zernike		(b) (e) (a)	[19, 41, 43–50]
	Hilbert		(b) (e) (a) (d)	[51–60]
Electrostatic PPs	Börsch	(g)	(c)+ (i) (a) (d)	[17, 21, 27] [61–64]
	Zach	(f) (g)	(c) (i) (a) (d)	[28, 40, 65–69]
	Anamorphotic	(f) (g)	(i) (h) (a)	[29, 70, 71, 72]
	$I \perp e^{-}$	(f) (g)	(j) (i) (h) (a)	[73]
Beam-induced PPs	HFPP charge	(f)	(b)	[1, 4]
	HFPP contamination	(f)	(b)+	[74]
Further PP concepts	Laser	(f) (g)	(h) (a)	[30, 32]
	Tunable Ampere	(g)	(c) (a) (j)	[75]
	Magnetic PPs	all HVs	(c) (b) (a) (j)	[31]
Obstructing devices	Tulip		(c) (d)	[76, 77]
	Foucault		(c)+ (d)	[78, 79]

a) b) c) d) φ e) φ f) φ g) h) i) j) ?

direction [38]. When acting in the same direction as the MTC, the total PP induced contrast plus the mass contrast are limited to the interval 0 to 1. However, when the PP acts so as to generate bright contrast, i.e. a negative phase shift at $q > 0$ with respect to $q = 0$, the PP contrast can exceed 1 and provide significantly higher total contrast [8,33] (see Table 2). An example where bright PP induced contrast is advantageous is where MTC is weak but sample induced phase shift is large, e.g. magnetic fields in a vacuum or in the imaging of hard magnetic materials.

4. Convenient operation
   A PP presents an additional electron optical element in the TEM that needs to be correctly aligned relative to the beam, with the illumination adjusted to optimize the imaging. In general, two scenarios entice users to utilize an additional optical element: either the PP provides a modest advantage and is very convenient to implement and operate, or some advantage commensurate with the effort to include a PP has to be achieved. Alternatively, the inclusion and alignment of a PP has to be fully automated.
5. Quantitative image contrast interpretation
   Ideally, a PP would allow *quantitative* interpretation of the sample phase shift and the PP image contrast, similar to the phase shift measurement in EH. This may be obtained by wave-function reconstruction techniques feasible with PPs that provide an adjustable phase shift [42] (see Sections ‘Quantitative interpretation of single phase plate images’ and ‘Object-wave reconstruction using phase plates’). In the case of a fixed phase shift either the object must produce discrete well separated beam at the HFPP or must be a WPO to allow quantitative extraction of the exit wavefunction. Indeed, the main objective is to achieve contrast enhancement while maintaining sample symmetry in the image.

No known PP implementation satisfies all of the above criteria simultaneously. On the other hand, almost anything that is placed in the BFP (charge or obstruction) leads to an enhanced contrast compared to focused bright field transmission electron microscopy conditions. Table 3 summarizes the various types of PPs as well as their

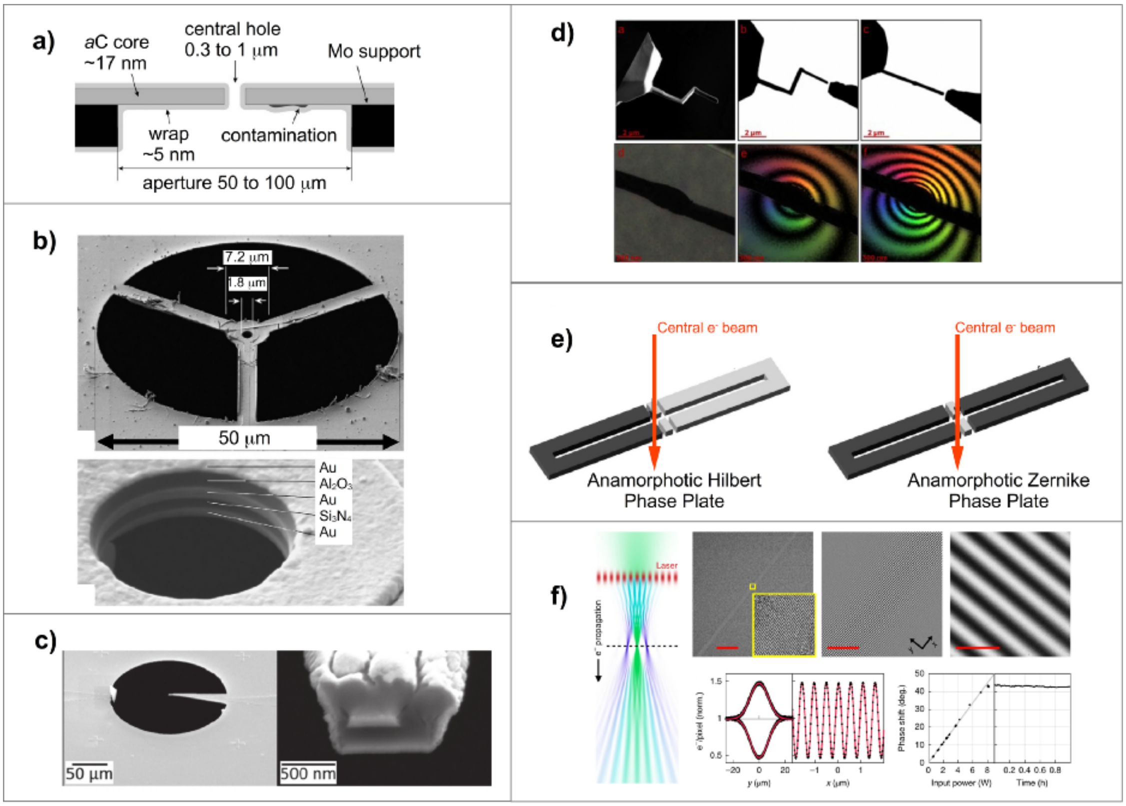

Fig. 3. Images of example implementations of various types of phase plates. (a) Schematic view of a cross section of a Zernike thin film type phase plate consisting of 20 nm thick carbon film with a hole to allow the direct beam at $q = 0$ to pass unaffected. A coating by a fresh carbon film can lead to a reduction in spurious charging [43]. (b) Scanning electron microscopy images of Börsch phase plates that use an einzel lens to vary the phase shift of the unscattered electron beam at $q = 0$ [17,21,62,100,188,283]. (c) Two scanning electron microscopy images of a Zach phase plate. The phase plate has a coaxial-like lead with a biased center electrode and a grounded outer electrode. The resulting electric field in the vicinity of the coaxial lead induces a phase shift on the high energy electron beam. The phase shift depends on the distance from the coaxial electrode and the potential of the central electrode. [28,65,68]. (d) An Ampere phase plate [75] where the phase shift of the high energy electrons arises from its interaction with the magnetic field of a current passed through a wire. (e) Anamorphotic implementations of phase plate. The anamorphotic phase plate requires an additional multipole lens that astigmatically spreads the back focal plane in order that the beam can be passed through the phase plate. It allows the operation of the phase plate in Hilbert (left) or Zernike (right) mode, as determined by the configuration of the biased electrodes [29,71,72,284]. f) Laser-field phase plate [32] that utilizes a Dirac–Kapitza effect to induce phase shift of the high energy electrons [107]. The laser phase plate requires the back focal plane to be enlarged to reach a cut-on frequency suitable for biological applications.

advantages and drawbacks, which are represented by pictograms. Fig. 3 illustrates a selection of PP devices.

Some basic concepts hold true for all PP types. A lateral drift of the phase shift distribution relative to the electron beam leads to phase contrast that does lacks radial symmetry and causes imaging artifacts. It does not matter whether the origin of the relative displacement of the phase-shifting device and the electron beam is caused by mechanical drift of the PP, or by the change in beam tilt resulting in a shift in the BFP. It would appear that PPs that utilize long-range fields and smooth phase profiles are less sensitive because the change in induced phase shift upon drifting may not be as abrupt as in devices that have a step-like onset of the phase shift at a particular frequency q_C.

In PPs where prefabricated hardware is placed in the BFP or where a field is generated by external sources, it may be necessary to magnify the diffraction pattern in the BFP to increase the ratio between the beam size and the size of the hardware. This is achieved by utilizing the objective minilens (sometime called 'Lorentz lens') [80], modifying the electron-optics setup of the microscope [12] or using a dedicated lens [81].

Thin-film based approaches

In this category, we summarize all the PPs that exploit the MIP of thin films to induce a phase shift on transmitting electrons as originally proposed by Börsch [11]. The most prominent type is the ZPP that consists of a thin film with a circular hole [19,82,83] (Fig. 3a). The PP position is adjusted so that the direct beam passes through this hole; and electrons transmitted through the film gain a phase shift depending on the electron energy and the film thickness and material leading to the phase shift as described by Eq. (16). There are several examples of a beneficial application of thin-film based ZPPs in the life sciences [45–47,84] (see also Section 'Biological sciences applications').

This type of PP fulfills important criteria such as avoiding obstructing PP hardware and an uncomplicated fabrication and operation. On the other hand, major drawbacks of this technique include the sharp onset of the phase shift profile corresponding to the hole radius, the susceptibility to spurious charging and contamination, and the fixed phase shift and information transfer damping due to electron scattering in the PP. Several experimental and theoretical studies were performed to determine the optimum parameters in dependence of the investigated samples and their imaging conditions (e.g. diameter of the hole, PP film thickness and phase shift) [41,43,44,49,82,85–87]. One approach, which is also valuable for other PP types, is the use of a transfer lens to create a plane corresponding to the BFP that allows more flexibility for the PP implementation [12,80,81,88]. To overcome the sharp phase jump at the film edge, a software-based enhancement of low spatial frequencies not phase shifted was proposed as well as the fabrication of a thin film with a tapered edge at the hole border [44,89]. Moreover, a continuous circular movement of the electron beam within the PP hole (or a movement of the PP with respect to the direct beam) during the acquisition also leads to a smoothing of the PP edge [90].

A second possible design of a thin-film based PP is the Hilbert PP, achieved by a thin film covering only half the plane of the BFP and with a thickness corresponding to a phase shift of π [51]. The PP is easier to align offering a variable cut on frequency controlled by the distance of the edge to the direct beam and yielding images with a directional, topological contrast. There are applications of Hilbert PP on biological objects [53,54] including an approach to numerically correct for the directional contrast [91]. A detailed study of the possibility of employing a crystalline thin film as PP was conducted using Hilbert PPs [57,92,93]; this showed that in the case of nanocrystallinity the effect of the varying phase shift caused by the locally varying crystal orientation was marginal. This result also holds true for ZPPs. In addition to experimental work, theoretical studies have been performed on optimum Hilbert PP and imaging conditions and the resulting image contrast [59,60].

Amorphous carbon (*a*C) was used in the vast majority of ZPPs, because of both its availability and its properties. A suitable material is amorphous and offers a good compromise between providing a high MIP V_0 while maintaining large electron mean free paths to avoid a large amount of undesired scattering in the PP [19]. The necessary film thickness to reach a phase shift of $\pi/2$ can be calculated using Eq. (16) and lies between 9 nm (20 kV) and 27 nm (300 kV) for aC PPs ($V_0 = 9$ V). At 300 kV this thickness leads to a scattering of 21% of the electrons in a ZPP [43].

While contamination of PPs can be avoided by heating the thin film [43,74], aging and charging of the PP may be more difficult to inhibit completely. Hardware optimizations, e.g. on-chip devices [94] and a specific PP holder including load locks for rapid PP exchange [95], were conducted to improve stability and to decrease contamination and charging of the PP. Several groups investigated the use of alternative materials, including Si and metallic glasses [50,58,96]. Metallic glasses may lower the relative amount of inelastic scattering in the PP due to a higher ratio of elastic to inelastic scattering [58].

Electrostatic devices

Among Hans Börsch's initial concepts was an electrostatic PP that induces a phase shift between scattered and unscattered electrons by a localized electrostatic field [11]. Possibly encouraged by the success of the thin film-based ZPP and their applications demonstrated by Danev and Nagayama [19], several groups fabricated an electrostatic Börsch PP consisting of an einzel lens mounted on three supporting rods (Fig. 3b), and demonstrated the phase-contrast enhancement [20,21,62,88,97]. Based on the same principle, similar devices were proposed using a single, narrow continuous supporting rod [61,98] or a drift tube setup [27]. Alternatively, the contact potential between metals can be utilized to generate an electric field acting on the direct beam [99]. The working principle of these PPs is based on the direct beam passing through a hole in which an electrostatic field is present [17]. Typically, this requires a five-layer device design with a central electrode double encapsulated in insulating material and two shielding metal cover layers (Fig. 3b). Applying a voltage to the central electrode while keeping the shielding layers grounded creates an electrostatic field that induces a phase shift on electrons transmitted through the central hole.

The major benefit of electrostatic PPs is the convenient tunability of the induced phase shift arising from the ability to apply various voltages to the central electrode. This benefit however comes at the expense of a more complex fabrication process and a considerable opaque area obstructing the beam in the BFP. In particular, the inner ring completely blocks an entire range of spatial frequencies introducing strong imaging artifacts. The interplay between the single-sideband contrast caused by the asymmetric supporting rods, the complete obstruction of a spatial frequency range by the central ring and the actual phase contrast caused by the induced phase shift is complex and requires extensive simulations to disentangle. These obstacles have resulted in a modest number of applications [63]. Nevertheless, the facility to tune the phase shift may prove to be critical in some applications.

To minimize artifacts introduced by the obstruction of electrons by the PP hardware, the Zach PP was proposed, which strongly reduces the amount of matter in the BFP by using a single rod with an open end (Fig. 3c), similar to an open coaxial cable [28,65]. Using this approach, the electrostatic field loses its homogeneity, an effect that introduces directional contrast that does not impair the microscope's resolution [68]. The Zach PP was applied in cryo-EM [67] and has been used to study in detail the influence of inelastic scattering on PP imaging revealing that phase contrast is present and controllable in the inelastic signal [40]. A recent study compared Zach PP and HFPP imaging of bacteriophagae. While it revealed similar contrast for small objects (< 10 nm) it also found that the Zach PP had the advantage in electron tomography due to the adjustable phase shift. On the other hand, the contrast of larger objects is higher in HFPP images due to the faster decay of the phase-shifting profile [69]. The concepts of Zach and Börsch PP have been combined by using multiple Zach electrodes to reduce obstruction when compared to the Börsch PP and to increase the homogeneity of the phase-shifting profile when compared to the single electrode Zach PP [97].

The Börsch and Zach PPs were combined with transfer lenses to enlarge the BFP and to improve the cut-on frequency [63,67,69]. A major problem, especially for Börsch PPs, is charging and contamination. Extensive studies revealed several sources of charging that can be linked to contamination, charging of the insulating parts of the PP hardware and a third type of charging whose origin remains unsolved [100,101]. Contamination and charging effects can be reduced by moderate heating of the PP [66,74] and by additional coating of the PP with an aC layer [67]. It is likely that the residual charging is similar to that responsible for the negative-charging variant of the HFPP (Section 'Work function alteration'), i.e. a beam induced change of work function of the PP material. A possibly obstruction-free electrostatic PP can be achieved by the anamorphotic PP [29,72]. For this PP, the electron beam needs to be astigmatically elongated in one direction and transmitted through a nanostructured slit in which a homogeneous potential may be applied in both sides of the slit (Fig. 3e). In this setup, no obstructing hardware is present in the beam path. However, using only a single such PP will leave a rather large range of spatial frequencies perpendicular to the slit direction in the center of the structure unaffected requiring a second anamorphotic PP. Moreover, this PP needs a strong modification of the electron optics of the TEM that so far has not been realized. It is also possible that the electron beam may hit some of the hardware elements, e.g. during the beam alignment, leading to spurious charging as in other designs.

A PP design consisting of two ring electrodes aimed at broadening the passband of the phase-contrast transfer function (CTF) has also been proposed [102]; this design however leads to a weak phase-contrast transfer at low spatial frequencies and requires beam obstructing hardware in the BFP. Another recent obstruction-free proposal is to use an electric current associated with a low energy beam of charged particles perpendicular to the high energy electron beam whose electrostatic potential yields a phase shift distribution that may be used as PP [73]. Although it is free of obstructing elements, this requires substantial modification of the TEM, by adding at least one more electron gun, which must be precisely aligned with the direct beam. Moreover, the resulting phase shift distribution is not ideal making experimental realization improbable.

Phase plates utilizing magnetic fields

The required phase shift between scattered and unscattered electrons may also be induced by a magnetic vector potential based on the Aharonov–Bohm effect [103]. To achieve a phase shift, the magnetic field has to be confined to a ring within the plane of the BFP. The vector potential will circulate around this ring causing a phase shift between electrons passing through the inside and outside of the ring. A practical realization may be achieved using a nano-structured, magnetized Co ring that has to be positioned in the BFP [31], but experimental proof of the enhanced phase contrast has not yet been reported. The small size of the magnetic structure (in the range of a few tens of nm) can be beneficial for creating the phase shift. A further advantage is the independence of the phase shift on the electron energy. Nevertheless, hardware will be needed to support the magnetic ring and this will cause blocking or damping of the electron beam. A recent attempt to utilize a magnetic field employs a magnetized wire [104] or a magnetic ring [105] located in the BFP of the objective lens.

Another novel idea is that of a tunable ampere phase plate (TAPP) reported in [75]. It utilizes the magnetic potential arising from a current carrying conductor. It thus offers an adjustable phase shift at the expense of placing a rather thin current carrying wire in the BFP of the objective lens.

Phase shift utilizing light–electron interaction

Another possibility to induce a phase shift on electrons is to use the interaction between electron and light [30,106]. Electrons passing through a beam of light experience a repulsive ponderomotive force [107,108] that can be theoretically derived from relativistic stimulated Compton scattering [30]. The phase shift of an electron is proportional to the photon density in the light beam and the time interval that the electron remains in that field. The necessary laser intensity is in the range of GW cm^{-2} [32], an intensity that so far has only been reached by pulsed lasers. Although it is an option to use pulsed lasers in combination with pulsed electron sources [109,110], cavity-enhanced continuous wave lasers are more compatible with the current TEM design and thus more promising [30]. Recently, a TEM with a laser PP was realized in practice showing the enhanced contrast transfer [32,111].

The advantage of the laser PP is that no hardware has to be placed close to the direct beam which avoids obstruction and scattering in matter. Moreover, it also offers a tunable and smooth phase shift distribution. However, it requires an alignment of the electron with the laser beam and the phase shift distribution exhibits oscillations. Other technical issues include the need to increase the laser power to reach the desired amount of phase shift of $\pi/2$ and, it requires a transfer lens to enlarge the BFP to reach reasonably low values of the cut-on frequency. The Laser PP is not expected to fit in current TEMs making development of a specific TEM necessary. Nevertheless, once these remaining issues are solved and PP alignment can be made automatically, the phase contrast in such a dedicated TEM could reach almost ideal conditions.

Phase shift induced by the direct electron beam

An early approach to the realization of a PP was to implement a coated spider thread in the BFP that charged under electron beam irradiation resulting in a phase shift distribution [16]. This design, however, did not provide stable conditions and did not have a broad impact.

Rather than trying to avoid contamination and charging on thin-film PPs, it turned out that these effects can actually be exploited to create the desired relative phase shift between the direct and diffracted beams. The concept of the hole-free (HF)PP [1,4] uses a uniform thin film in the BFP and the phase shift is induced by the direct beam itself. Later sections deal explicitly with the implementation (Section 'Hole-free phase plate implementation'), working principles (Section 'Microscopic mechanisms responsible for hole-free phase plate operation') and applications of HFPPs (Section 'Applications of hole-free phase plate').

Obstructing devices

Obstructing electrons in the BFP is a technique commonly applied in bright-field or dark-field TEM where diffraction or mass-thickness contrast may be observed. In addition, it can also lead to phase contrast in the image. Masking out approximately half of the electrons in the BFP using the objective aperture yields a strong topological contrast that is based on the directional scattering of electrons by the object's phase gradients [78], also referred to as 'Foucault imaging'. Milling slits in the mask may allow imaging with a full transfer of spatial frequencies over specific regions if contamination and charging are avoided [79]. Calculating the phase-contrast transfer at spatial frequencies where one half of the electrons have been intercepted in the BFP is equivalent to phase shifting these spatial frequencies by $\pi/2$ at half the amplitude thus yielding exactly half of the ideal Zernike type phase contrast [76]. This effect is also commonly called single-sideband or schlieren contrast and occurs as well for other PPs where parts of the BFP are blocked by a supporting rod [21,28,112,113].

Based on this principle, a PP design simply consisting of a blocking device in the shape of half a circle carried by a supporting rod (resembling a tulip) has been proposed [76,114]. In this form, it leaves high spatial frequencies unaffected and acts only on low spatial frequencies that are weakly transferred under Scherzer or focused conditions. Strictly speaking, these obstructing devices are not actual PPs as they do not actively shift the phase of electrons in the BFP. They increase contrast in images [76], have been used to study contamination and charging of hardware in the BFP in detail [77], and have yielded the same results as the investigations that used Börsch PPs [100]: Charging may be categorized in the following ways: 1.

contamination-induced; 2. charging of non-conductive material and 3. patchy work functions and beam induced modification of work function of metals.

HFPP implementation

The previous section has provided a review of various PP imaging implementations and a brief survey of their advantages and drawbacks. The rest of this review is dedicated to the HFPP, its implementation, the microscopic mechanisms responsible for its operation and example applications. The discussion below applies to any HFPP, even when referred to as VPP, e.g. [4,5,115]. The microscopic mechanisms responsible for contamination, charging and work function variation are applicable to other types of PPs where an electron beam strikes the PP hardware, or to samples examined by TEM and scanning TEM (STEM).

The HFPP offers several practical benefits over alternatives:

Table 4. Known advantages of the hole-free phase plate.

- It is easy to operate.
- It is easily retrofitted to most existing microscopes.
- It is inherently self-centering (alignment of the beam with a particular location on the HFPP is not required).
- The phase shift profile is smooth without step-like onset of phase shift.
- The phase shift area size is matched to the beam size at the BFP (BFP).
- Stability is sufficient for electron tomography over several hours, after an initial settling period. When correctly implemented in a microscope with an adequate vacuum, the HFPP long-term stability limit is set by the mechanical drift of the aperture mechanisms holding the HFPP film.
- The entire HFPP is electron-beam transparent. There is no blocking of particular spatial frequencies or azimuthal angular range by the PP hardware.
- The charge variant of the HFPP utilizes the electric field in the vacuum generated by the charge redistribution in a uniform film rather than the product of the MIP and the thickness a of a thin film. As a result, the HFPP does not exhibit sharp edges of the phase shift and does not suffer from fringing artifacts.

Known drawbacks of HFPP at present include the following:

Table 5. Known drawbacks of the hole-free phase plate.

- There is a lack of control of the HFPP phase shift.
- The phase shift is time-dependent, although this effect can be small enough to allow acquisition of data over many hours when the HFPP is allowed to settle for its mechanical drift, good quality carbon film is used and the microscope vacuum is adequate.
- The phase shift profile is usually unknown and is not an infinitely narrow δ-function as desired for an ideal Zernike PP. However, the incident beam has a finite angular width making this requirement largely irrelevant.
- Scattering in the thin film of the HFPP leads to a damping of the obtainable contrast in comparison with an ideal PP.
- A halo-like contrast is produced at the edges of phase objects in some cases.

Table 4 lists HFPP advantages. The core concept of the HFPP is the use of the high energy electron beam itself to define the location of the PP center, i.e. the position of the $q = 0$ beam. The size of the phase-shifting area is also well matched to the beam size ensuring that all spatial frequencies $q > 0$ experience a phase shift. The fact that there is no beam opaque hardware eliminates imaging artifacts and inefficiencies in the contrast transfer that arise from beam blocking [8]. The disadvantages (See Table 5) of HFPP arise from the inability to control the phase shift of the PP. While understanding of the microscopic mechanisms responsible for HFPP operation has been improving (see Section ‘Microscopic mechanisms responsible for hole-free phase plate operation’), a reliable method to correctly predict the phase shift is not known at this time.

Figure 4(b) shows that a ZPP utilizes the phase shift arising from the MIP of a film relative to the zero phase shift of the direct beam passed through a hole at $q = 0$. Both HFPP and ZPP exhibit film charging in areas irradiated by the electron beam, including scattered beams, which depends on the experimental parameters. In HFPP, the (positive or negative) charging [1,116] is used for the benefit of contrast enhancement. In ZPP, the charging amounts to a spurious effect that can be partially reduced by careful film preparation and coating of excessive contamination by an additional carbon layer [117]. It is possible that heating the ZPP hardware above about 350° C during the operation can eliminate the charging, although the idea has not been tested on ZPPs yet [116]. The ZPP or HFPP heating can affect the imaging of cryo samples by radiating heat energy onto the sample.[3]

The self matching of the phase-shifting patch of HFPP to the beam size at the BFP reduces the contrast ringing when compared to ZPP. This can be seen in Fig. 5 that compares images acquired by standard TEM, a carbon film with hole Zernike type PP and HFPP, all data zero-loss filtered. The HFPP in Fig. 5c provides a contrast that is higher than that in Fig. 5a and comparable to that of Fig. 5b. The lipid bilayer can be observed in the HFPP image in Fig. 5(c) but not in (a) or (b).

When compared to other types of PP images using computer simulations of a 5 nm spherical nanoparticle (Fig. 6), the HFPP with a screening charge located near the primary beam induced charge provides a contrast close to a phase contrast of a hypothetical ideal ZPP with an infinitely small hole and perfectly parallel electron beam [1].

HFPP: desirable thin film properties and preparation

As compared to alternative PP methods, the salient feature of HFPP is the use of a *uniform* thin film locally modified by the electron beam itself [1–4,12,118]. Several microscopic mechanisms can be responsible for HFPP operation (see Section ‘Microscopic mechanisms responsible for hole-free phase plate operation’) and many different types of HFPP films can be utilized. Films such as amorphous carbon (*a*C), Ge, Si, SiN, amorphous metals ($Pd_{77.5}Cu_6Si_{16.5}$ and $Zr_{65}Cu_{7.5}Al_{27.5}$) as well as multilayers and a single crystal Au films have been successfully used. Single crystal Au films were tested to assess the effect of film conductivity on HFPP performance.[4]

All films reported so far provided contrast enhancement although there could be a variation in their final settled state and the rate of

---

[3] In microscopes equipped with transfer lens below the objective lens, the radiative heating of the sample due to the presence of heated PP hardware can be avoided.

[4] The single-crystal Au films diffracted the electron beam, but the effect on the image contrast was limited for the used thickness (13 nm) and the 200 kV incident electron energy. The Bragg diffraction resulted in broad bands across the field of view [1] that did not interfere with the observation of 10 nm diameter elk fibrils.

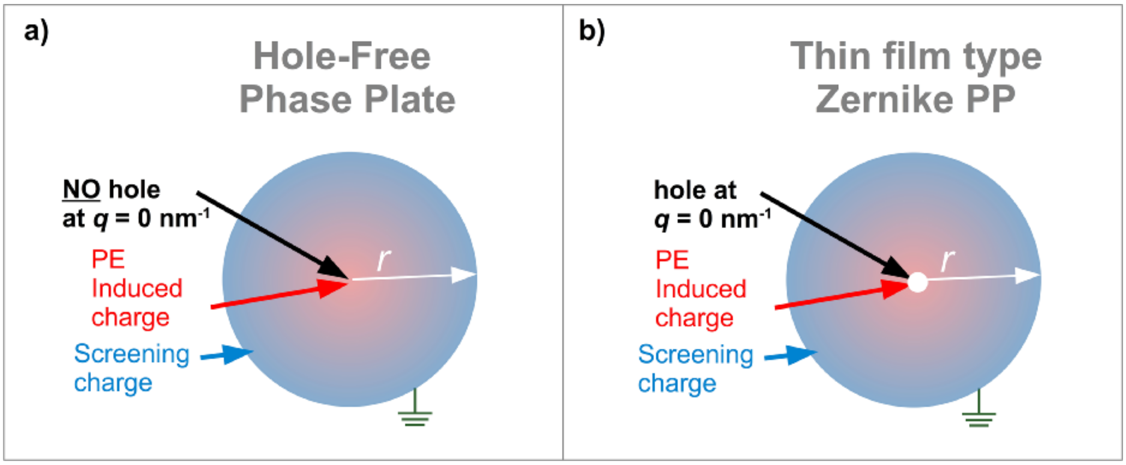

Fig. 4. Comparison of hole-free phase plate and Zernike phase plate concepts. Hole-free phase uses primary-beam generated charging of an arbitrary location of a uniform thin film [1,4]. In both hole-free phase and Zernike phase plate, the film edge is connected to the microscope hardware and therefore is electrically grounded. Zernike phase plate uses an electrically grounded thin film with a prefabricated hole that must be centered relative to the incident electron beam. The phase shift is in principle controlled by the mean inner potential of the carbon film and its thickness [19].

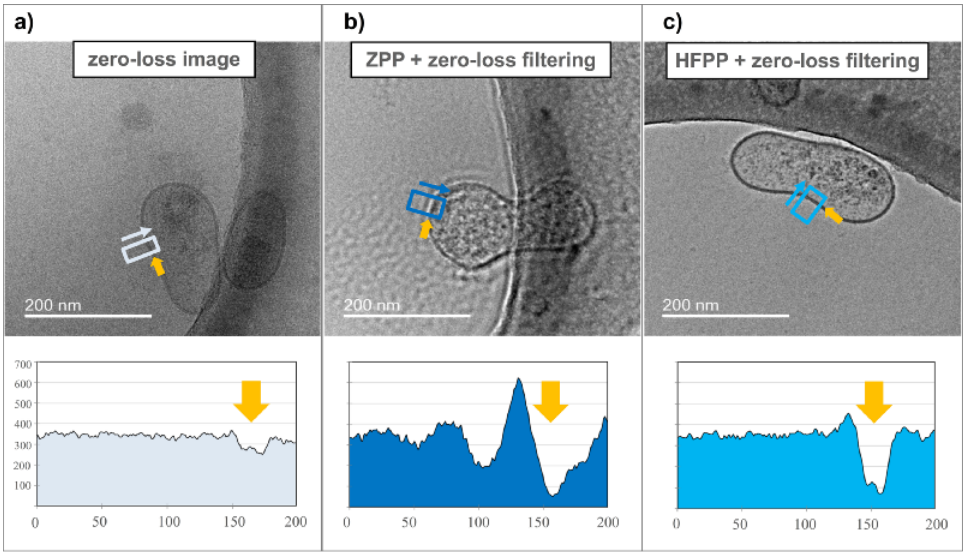

Fig. 5. Comparison of cryo-transmission electron microscope images obtained using (a) a zero-loss filtered bright field transmission electron microscope to provide a baseline, (b) thin film type Zernike phase plate combined with zero loss filtering and (c) zero-loss filtered hole-free phase plate result. The imaging parameters were 200 kV incident energy, energy selecting slit width $\Delta E = 20$ eV, 2 µm underfocus for (a), in-focus for (b) and (c). The imaging dose was 20 $e^-/\text{Å}^2$ for all data sets. The blue arrows next to the profile box in the images indicate the left to right direction of the corresponding intensity profile. The yellow arrows on both images and profiles indicate the position of the cell membrane. The scale bar is 200 nm in images (a)–(c). The data were obtained using a JEOL 2200 FS, a 200 kV transmission electron microscope equipped with in-column Ω energy filter at JEOL Ltd. Akishima, Tokyo, Japan. *Figure courtesy of Dr. Naoki Hosogi, JEOL Ltd*, see [210].

settling toward a steady state, which was not systematically investigated. No qualitative difference in terms of contrast enhancement was observed between Au and other films, such as aC. The fact that the HFPP film material properties have very limited effect suggests that surface phenomena are responsible [1,4,58,74,116]. The above suggests that controlling film surface properties, in particular surface contaminants, is critical.

Two aspects need to be considered when selecting film thickness. First, the thin film needs to provide a sufficient mechanical strength to stretch over a support disc or stripe and to maintain flatness over the area of the HFPP support [119,120]. The film mechanical strength increases with its thickness. However, the film thickness must not exceed a small fraction of the total inelastic mean-free path of the fast electrons in order to avoid excessive inelastic scattering (see Section 'A brief theory of phase plate imaging').[5]

For practical purposes, aC films with a thickness between ≈5 to ≈20 nm appear to be a good choice, arising from the availability of aC film fabrication in EM laboratories and its acceptable mechanical and electrical properties. A 5–20 nm carbon film can be stretched over many µm opening in a HFPP support aperture providing sufficient area for hundreds of HFPP experiments. A numerical example in [1] suggests that for a 10 nm thick carbon

---

[5] The total inelastic scattering cross section depends only weakly on the atomic number Z as $\approx Z^{\frac{1}{3}}$ [121]. Therefore, the choice of the film material does not need to be entirely driven by a need for a low atomic number Z.

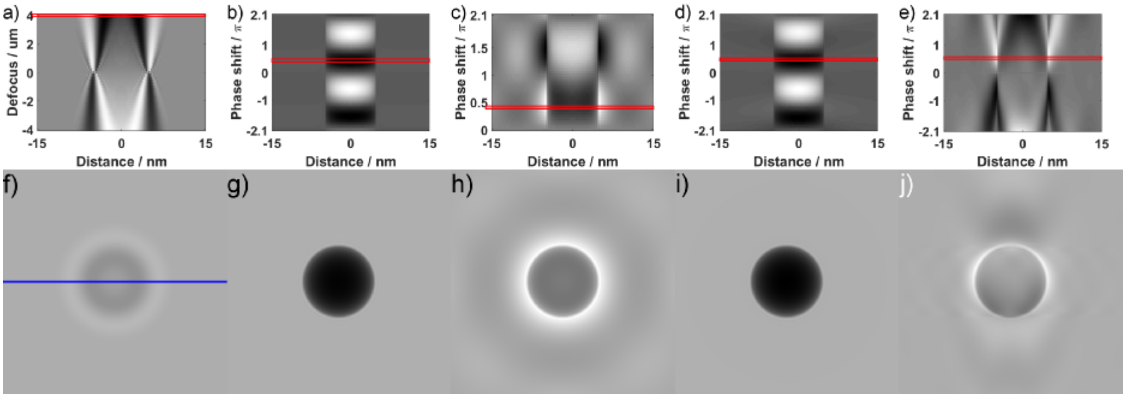

Fig. 6. Image simulations of an aC spherical nanoparticle with 5 nm diameter considering (a,f) conventional bright-field transmission electron microscope, (b,g) an ideal phase plate, (c,h) a thin-film Zernike phase plate with a 750 nm hole diameter (= 0.08 nm^{-1}), (d,i) a hole-free phase plate with q_c=0.01 nm^{-1} and (e,j) a Zach phase plate with a distance of 750 nm of the vertically oriented rod to the direct beam. General parameters were 300 keV electron energy, C_S=5 mm, focal length = 5 mm, focal spread = 8 nm, objective aperture with a radius corresponding to 8 nm^{-1} and an illumination semi-convergence angle of 0.4 mrad. Scattering in the thin-film based phase plates was neglected. The simulations were performed for (a) a defocus between −4 and 4 µm, (b,d,f) a phase shift range between −2.1 - 2.1 π and (c) a phase shift range between 0 and 2.1 π as Zernike thin-film phase plates only provide positive phase shift. Defocus was 0 nm for phase plate images. Figures (a–e) show line profiles across the simulated nanoparticle (the position indicated in (f) for the different parameters and in (f–j) show selected images corresponding to a phase shift of −4 µm or 0.5 π, respectively, with the position marked in red in (a–e). The object size of 5 nm (with a corresponding spatial frequency of 0.2 nm^{-1}) is small enough to be mostly unaffected by the long-ranging tails of the hole-free phase plate leading to a hole-free phase plate image contrast comparable to the ideal case. However, its information is still in the decaying range of the Zach phase plate leading to reduced asymmetric contrast. The sharp edge of the Zernike phase plate leads to bright (or dark) halo around the nanoparticle. The contrast of images (a–e) has been maximized for each image independently, while (f–j) are displayed on the same contrast scale defined by the maximum contrast in the ideal case (b).

film used as a HFPP in a 200 kV TEM less than 10% of the electrons will be affected by inelastic scattering. Since the HFPP in both positive and negative modes of operation [1,4,116] relies on the electric field in the vacuum above and below the film (see Section 'A brief theory of phase plate imaging' and 'Microscope operation in phase plate imaging'), the film thickness should be kept small while maintaining film flatness and mechanical strength.

The thin film growth method can affect the electrical and mechanical properties of the film, its porosity and the amount of adsorbed contaminants in particular [74]. The effect of contamination and means for controlling it are discussed in Section Contamination build up. The film contamination and aging studied in the context of ZPP is also applicable to HFPP [6,120,122–127].

While HFPP films can be commercially microfabricated, it is also possible to prepare adequate quality aC films using a rudimentary carbon coater available in most electron-microscopy laboratories. Fig. 7a and b illustrates the steps needed to prepare a suitable film and to implement a HFPP in a typical TEM. First, ≈10nm thick aC is deposited onto freshly cleaved muscovite mica. An electron-beam evaporation of graphite source has been extensively used in our laboratory, but other methods such as vacuum sputtering in a sputter coater or carbon-rod arc discharge evaporation by passing high current through it are also known to provide acceptable quality aC films [74,116].

The carbon film is then floated onto an objective aperture disc or stripe that is placed in the BFP of the microscope. Floating the aC film onto a support disc or stripe is identical to the aC film preparation for sample support. To limit hydrocarbon contamination of the aC film during preparation, it is desirable to use deionized (or at least distilled) water to float the film. The film can be then left to dry in standard laboratory air. The use of plastic beakers and dishes for film handling and transferring is not recommended so as to reduce the chance of carboneous contamination. The aperture discs or stripes can be transferred on filter paper, glassware or aluminium foil.[6]

Film flatness across the aperture opening is critical to ensure convenient *on-plane* HFPP operation, as discussed below. Since under typical conditions, the beam diameter at the HFPP does not exceed a few µm, a 100 µm diameter aperture covered with a HFPP film provides enough film area for hundreds of HFPP experiments. While the steps above are required to retrofit a HFPP in an existing TEM [95,118], instrument manufacturers offer specialized (heated) aperture support and high quality commercial HFPP films [119,120,126]. Commercial HFPP hardware is often equipped with convenient HFPP positioning software and hardware [127–129].

The use of highly insulating thin films, such as amorphous SiN, is not recommended as it can result in instabilities (likely a micro dielectric breakdown due to excessive charge buildup) during HFPP imaging. As a matter of fact, SiN films were observed to charge sufficiently for a 300 keV electron beam to follow the mechanical movement of the membrane, a phenomenon that suggests strong local positive charging of the SiN film.

Microscope operation in PP imaging

The practical operation of a TEM equipped with a HFPP has been described in detail [1]. In this section, we summarize the procedure and provide additional detail on the practical operation of a microscope with a HFPP. Fig. 7b schematically illustrates the steps needed to prepare a film suitable for HFPP, for microscope set up and operation.

The microscope operation consists of two steps. First, initial alignment of the microscope is performed (Fig. 7b) and Table 6) and then the data can be acquired (Fig. 7c) and Table 7. The initial microscope operation is nearly identical to the alignment used for conventional bright field transmission electron microscopy imaging. However, for HFPP imaging, it is necessary to ensure that the BFP cross over coincides with the HFPP film position in the column, as it does for ZPP imaging [1,118,127].

The typical alignment procedure is as follows:

Following the alignment above, the microscope is ready to collect data (see Fig. 7c). In a stable microscope with a reasonably flat HFPP

---

[6] Food grade Al foil should be avoided due to possible silicon oil contamination. UHV grade Al foil should be used.

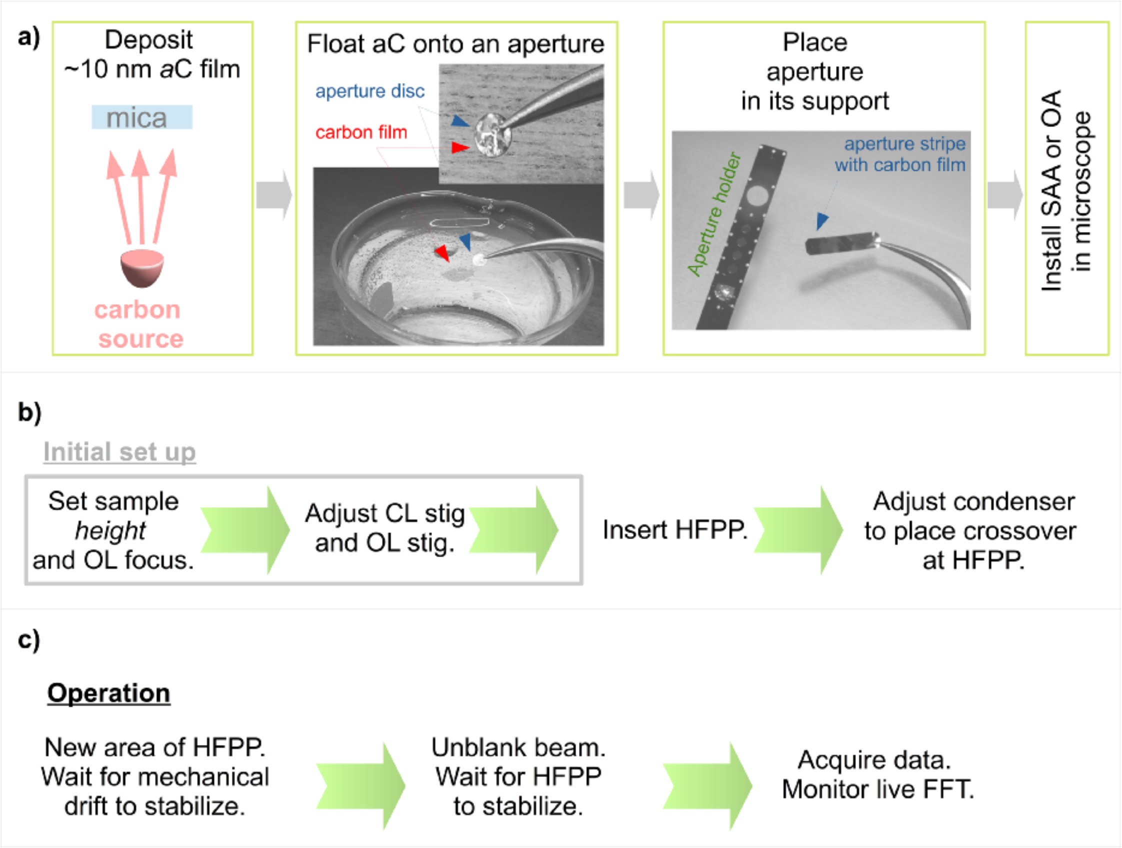

Fig. 7. Implementing hole-free phase plate imaging in a transmission electron microscope consists of three steps. (a) Film preparation, (b) microscope set up and, (c) data acquisition. (a) Schematically depicts the process of amorphous carbon hole-free phase plate film preparation. First, $a \approx 10$ nm carbon film is deposited onto freshly cleaved muscovite mica substrate, for example by electron-beam vacuum evaporation. The film is then floated onto water surface and picked onto aperture disc or an aperture stripe covering the opening in the aperture discs or stripe. The aperture disc is then placed in the (objective) aperture mechanism and inserted in the microscope column. (b) Indicates steps in initial microscope set up for hole-free phase plate imaging. The set up is identical with standard microscope alignment for bright field transmission electron microscopy imaging with an additional step to ensure that diffraction plane coincides with the hole-free phase plate film plane. (c) Microscope operation. During data acquisition an area of the phase plate is initialized by imaging a sacrificial area of the sample. After an initial settling period the phase plate can be typically used for several hours. When imaging performance deteriorates a new area of the film is initialized [1]. Abbreviations used in this figure are SAA: selected area aperture; OA: objective aperture; CL: condenser lens; OL: objective lens.

film, the alignment above only needs to be done infrequently, see Table 7. Small adjustments of the condenser lens may be needed if the HFPP film is not sufficiently flat. Combining the HFPP with energy filtering can lead to an improved signal-to-background ratio in thick samples. An in column Ω filter usually has adequate performance and is easy to operate.

The data collection steps are as follows:

As Fig. 7c and Table 7 indicate, the data acquisition is performed in the same way as for conventional bright field transmission electron microscopy. Note that the objective lens astigmatism affects high spatial frequencies, whereas low spatial frequencies are affected primarily by the symmetry of the electric field at the HFPP (Table 6). Loss of electric field radial symmetry can arise, for example, from the proximity of a dust particle on the HFPP film. Such a defect cannot be compensated by objective or condenser lens stigmator coils and a fresh area of the HFPP film should be utilized.

Adding a small amount of defocus has been reported to improve the contrast transfer for some samples [133–135]. It is, however, desirable to apply this defocus before adjusting the HFPP crossover, or to use a lens downstream from the HFPP plate to ensure that the position of the cross over at the HFPP does not change [2]. Using an objective lens focus moves the cross over above the HFPP plane (objective lens excitation increased) or below the HFPP plane (objective lens excitation decreased) resulting in *off-plane* imaging [38].

Figure 7c and Table 7 outline the steps followed during the acquisition of HFPP images or an image series [1], including electron tomography HFPP data sets [34,136]. The fact that the HFPP aperture is moved with the beam blanked implies that the HFPP film needs to be flat over the distance over which the aperture moves, i.e. no more than a few nm variations of the HFPP height over a few μm [119,126].

The time profile of the HFPP settling depends on the microscopic mechanisms involved, the film properties and temperature, the beam current and possibly the beam current density, but it can be often described as logarithmic or as $(1 - \exp^{\frac{-t}{\tau}})$, the settling constant τ being typically in the order of a few tens of seconds. In some cases a double-asymptotic behavior consisting of two settling constants is observed [4,137]. Therefore, the HFPP phase shift and consequently image contrast typically differs from its asymptotic state at $t \rightarrow \infty$ by only a few percent after the HFPP was allowed to settle for time corresponding to a low multiple of settling constant τ.

A live FFT of the acquired HFPP images should be observed to assess whether the HFPP image change is within acceptable limits,

Table 6. Alignment procedure for hole-free phase plate.

1. Reset the objective lens current to its standard value determined by the instrument manufacturer and perform the usual alignment of the condenser lens and the objective lens current axis, i.e. using objective lens current wobbler, as is done in conventional bright field transmission electron microscopy imaging.
2. Adjust the objective lens astigmatism using the live fast FFT method as is customary in standard bright field transmission electron microscopy.
3. After these basic steps, the (objective) aperture with the HFPP film should be inserted in the column. The stability of the mechanical drift is not critical at this point, as the alignment aims to locate the BFP at the same plane as the HFPP film.
4. Adjust the condenser lens while keeping the objective lens current fixed to ensure that the cross over at the BFP coincides with the plane where the HFPP film has been inserted. This is referred to as the *on-plane* operation indicating that the BFP coincides with the HFPP plane [127]. The placing of the BFP cross over at the HFPP plane is ensured by observing a Ronchigram, a shadow image of the HFPP created by the cross over near the HFPP film. The Ronchigram technique is identical to the one used to align STEM probe at the sample [130].[a]
5. Adjust the condenser lens stigmator coils to obtain a radially symmetric Ronchi pattern of the HFPP film, thus ensuring a radially symmetric response of the HFPP.[b]
6. Fine-tune the objective lens astigmatism to ensure that the FFT of the sample with HFPP in the beam remains radially symmetric. Note that the objective lens astigmatism coils act at high spatial frequencies, i.e. far from the center of the live FFT. The shape of the FFT near $q = 0$ is determined solely by the shape of the beam footprint and the associated fringing field in the vacuum near the HFPP.
7. When low dose cryo-TEM is performed, an additional step has to be taken to ensure that the crossover at the HFPP plane remains at the same location when the low magnification (survey) mode of low dose imaging is used as it does during high magnification [131,132].

[a] When the cross over does not coincide with the HFPP film the imaging artifacts including contrast reversals can appear; this can lead, for example, to an unreliable interpretation of polarity of charge on an irradiated film [38].

[b] In our experience, the HFPP imaging is not overly sensitive to the condenser astigmatism, i.e. to round shape of the cross over at the HFPP plane, presumably due to the long range nature of the electric field in the vacuum outside the HFPP film and to the phase shift being a path integral of the field over a large distance. Extensive elongation of the beam footprint that sometimes arises from the mechanical drift of the HFPP aperture mechanism can result in a loss of radial symmetry of the CTF and can be observed by loss of radial symmetry of live FFT.

Table 7. Steps taken for hole-free phase plate data collection.

1. Following the adjustment in Table 6 and Fig. 7b, the beam should be blanked.
2. The HFPP aperture mechanism is then moved to a new location on the HFPP film at a sufficient distance (a few µm) from previous beam footprints on the HFPP film.
3. The beam is unblanked and the HFPP is allowed to settle to within a few percent of its asymptotic steady state. For most HFPP films and for typical imaging parameters, the settling period takes from a few seconds to a couple of minutes. The steady state can be recognized by observing the live FFT. Initially, the rate of change of the Thon ring positions is high but it gradually decreases with the electron dose. The Thon rings closer to the center of the FFT settle faster than those at high spatial frequencies. Once the Thon rings up to the spatial frequencies of interest for a given experiment cease to evolve, data can be collected.[a]
4. Images are then collected on desired (multiple) locations of the sample while the FFT is continuously monitored for abrupt changes or loss of radial symmetry.
5. Data collection may have to be interrupted and a new location on HFPP film utilized if the FFT indicates a loss of radial symmetry of Thon rings or excessive changes in the Thon rings positions. If a new area of the HFPP needs to be utilized, the steps described above here should be performed from the beginning, starting with item 1.
6. A small adjustment of focus, preferably using the lens downstream from the HFPP, may be required to accommodate the sample height or thickness variations. Large changes of focus should be done using a mechanical z-height adjustment of the sample stage thus leaving the condenser and objective lens excitation unchanged to ensure the crossover position at the HFPP plane.

[a] The rate of change of the Thon rings can sometimes be described by $1 - e^{\frac{-t}{\tau}}$, where t is time and τ is the characteristic time of Thon ring settling. The characteristic time is larger for Thon rings further from the FFT center, possibly due to a decrease in beam current density at the HFPP with the distance from the center of the beam at $q = 0$.

e.g. whether the Thon rings in the FFT are within desired limits [133,1]. In our experience, the mechanical drift of the HFPP aperture mechanism sets the limits of the time interval for which a single footprint area of the HFPP can be utilized, typically in the order of tens of minutes to many hours. When the HFPP mechanically drifts such that the beam footprint at the HFPP film is no longer at the same location as it was when the beam was unblanked, the modified area of the HFPP becomes an extended elliptical streak rather than a radially symmetric area. Consequently, the FFT of a HFPP image exhibits elliptical or hyperbolic features near $q = 0$ rather than a radially symmetric transfer band. As mentioned earlier, the deformed transfer near $q = 0$ can not be corrected by an objective or condenser lens stigmator. The beam should be blanked and a new area of the HFPP should be pre-irradiated and utilized using the same steps as described earlier [1][7]. In our experience, providing the same imaging parameters and film condition is used, the HFPP tends to the same asymptotic state regardless of the area of the HFPP film chosen, leading to imaging repeatability [138,139].

Relations between phase shift distribution and imaging parameters

The form of the phase shift in the HFPP depends on the spatial distribution of the primary beam generated charge and the induced screening charge [1]. Two limiting scenarios can be envisioned. Sometimes, the induced screening charge is on distant grounded objects, such as grid bars and microscope polepieces, as seen in scenario **A** in [1]. Alternatively, the induced screening charge can be located in close proximity to the primary beam generated charge, i.e. scenario **B** in [1]. The distance between the primary beam generated and induced screening charge in scenario **B** is determined by the (Debye) screening length of the thin film material. Taking into account the fact that semiconducting or metallic films are used for

[7] The exact dose needed to achieve the asymptotic state depends on parameters such as the PP material, the history of the PP film (e.g. whether it was in the microscope for a long period of time) and, possibly, on microscope vacuum. Typically, the irradiation dose for HFPP to settle is in the order of 1 Ccm^{-2} to a few hundred Ccm^{-2} [1,74,116,137].

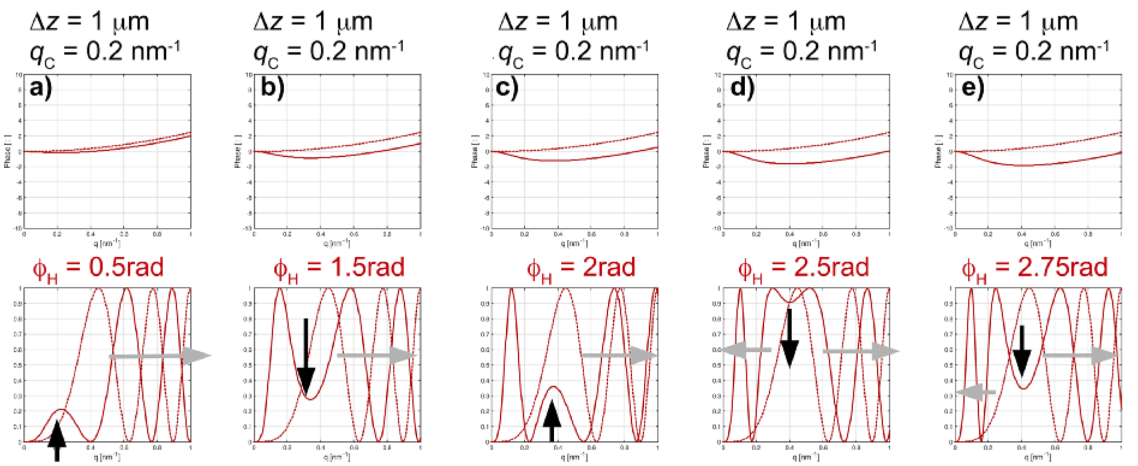

Fig. 8. When the defocus and phase shift of the phase plate act in opposite directions, a flat transfer band appears. The Thon rings move in opposite directions, contracting or expanding to the left and right of the Scherzer-like transfer band. As a result, at too low or too high magnification where only low or high spatial frequencies are observed in live fast Fourier transform, the polarity of charge can be incorrectly determined. The simulations were performed for an underfocused (weakened) objective lens and a positive-charge hole-free phase plate. See [38] and the videos therein for detail and guidance on determining the polarity of the hole-free phase plate phase shift. Upper panels are the phase shift corresponding to an aberration function $W(q)$ arising from defocus Δz, spherical aberration C_S (dashed) (see Eq. (9)). The solid curve captures defocus Δz, spherical aberration C_S and an increasingly positive charge Φ_H on a hole-free phase plate, see Eq. (19). Bottom panels are the corresponding contrast transfer functions taken as $\sin^2(W(q))$.

HFPP, we have concerned ourselves with scenario **B** below. Both scenarios can be solved analytically, scenario **B** leading to an elliptic integral of the second kind [1] that can be approximated by a Lorentzian $P_H(q)$, Eq. (19).

As mentioned above, the HFPP phase-shifting (charged) patch can produce either an advancing or a retarding phase shift (see Table 2) depending on the polarity of the primary beam generated charge. Similarly, the defocus of term of the contrast transfer function can produce an advancing or retarding phase shift, see Table 2. On the other hand, the spherical aberration term is the only one that, in an uncorrected microscope, always advances the phase shift at $q > 0$ relative to $q = 0$.[8] As a result, situations can be frequently encountered where the spherical aberration, defocus term and PP act in opposite directions over a range of spatial frequencies [38].

The opposing action of the defocus, spherical aberration and PP terms leads to a band of flat phase similar to the Scherzer transfer band [39]. The outcome is illustrated in Fig. 8, as discussed in detail in [38] including simulated videos of the contrast transfer function evolution with a charge on the HFPP film. In principle, the transfer band can be utilized to image spatial frequencies of interest. In practical terms, the situations in which the phase shift of the PP acts in opposition to other terms (defocus or spherical aberration) complicate the interpretation of the polarity of the primary beam generated charge; it is not possible to rely on the expansion or contraction of the Thon rings in the live FFT of the image series alone to identify charge polarity [38].

As discussed above and in Section 'A brief theory of phase plate imaging' and [1], it is the difference between the direct and diffracted beam phase shift that results in image contrast enhancement. Most of the phase shift is acquired when the fast electron travels in the electric field in a vacuum near the charged patch of the HFPP film. The electric field in the vacuum arises from the difference in spatial distribution of the primary beam generated charge and the induced screening charge [1,38,116]. The fringing field in vacuum is present even though the *charged patch of the film is a charge neutral object*. That is, the amount of the primary beam generated and the induced screening charge are exactly equal.[9]

Figure 9 illustrates the origin of the fringing field in the vacuum near the HFPP film. Fig. 9a shows the equipotential planes for a nearby-screened charge (scenario **B**) as a function of distance along the beam path and the radial distance from the center of the incident electron beam at $R = 0$, i.e. $q = 0$ in reciprocal space. It also indicates that the charged patch on both the upper and lower surfaces of the HFPP film produce the same fringing field in a vacuum.[10]

Figure 9b schematically shows that the total phase shift ($(\varphi(\mathbf{r})_{\mathrm{tot}}$ in blue on the right-hand side) can be significantly higher than the difference in phase shift between the direct beam at $q = 0$ and the

---

[8] Under typical HFPP imaging conditions, the C_S term contribution to the CTF is smaller than the defocus and PP terms.

[9] In scenario **A** in [1] the field in the vacuum arises as a result of the large separation of the primary beam generated charge and the induced screening charge. The profile of the phase shift in this scenario is somewhat flatter than in scenario **B**; the entire electron beam in scenario **A** passes between the primary beam generated and the induced screening charge. In scenario **B**, the lateral extent of the primary beam generated and the induced screening charge is of the same order of magnitude as the beam size. Scenario **A** is conceptually trivial and not discussed here. Details relevant to scenario **A** can be found in [1,140,141]. Scenario **B** is relevant to HFPP operation.

[10] Note that as a result of the difference between the spatial distribution of the primary beam generated and the induced screening charge, the fringing field in the vacuum is different from the field of a dipole oriented with its dipole moment along the beam path. The phase shift of an electron traveling parallel to a dipole long axis would be exactly zero, because the phase shift acquired above the mid plane of the dipole is exactly cancelled by the phase shift acquired below the mid plane of the dipole. This is clearly not the case for the HFPP.

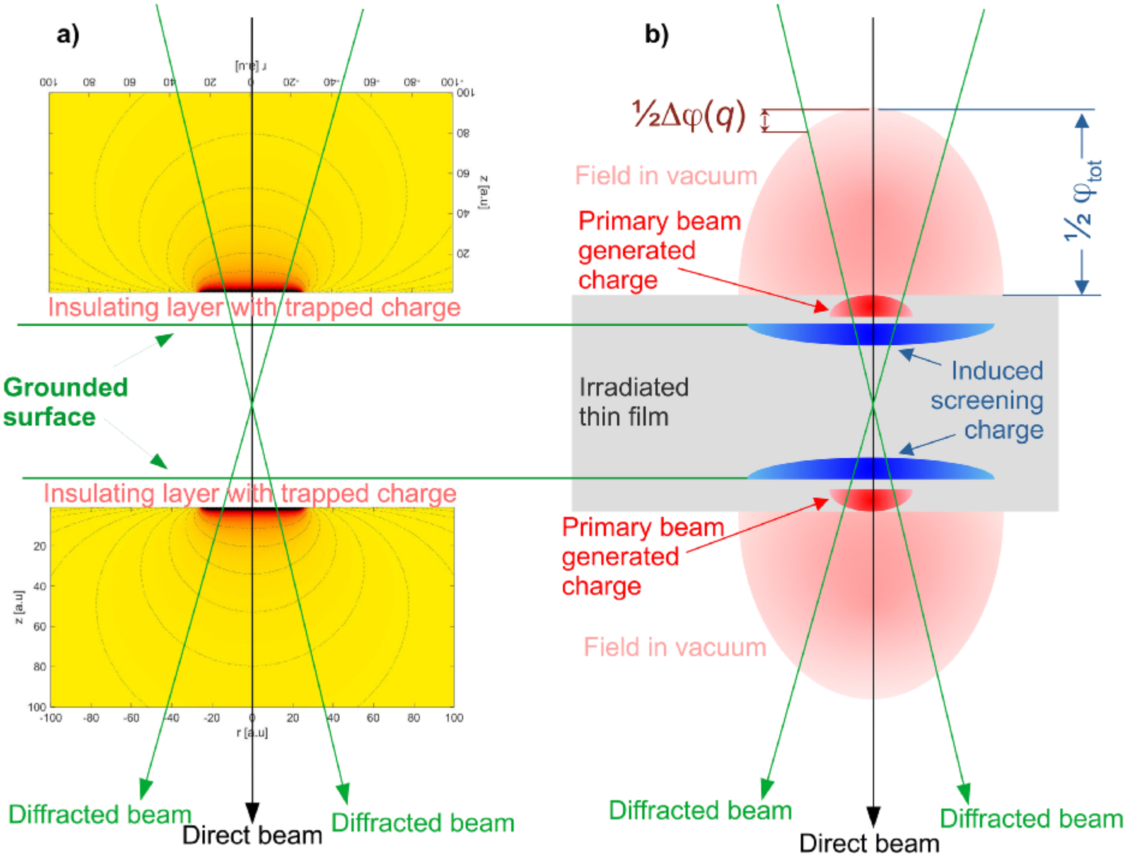

Fig. 9. (a) Equipotential planes (dashed lines) of a fringing field in a vacuum near charged 50 nm diameter patch of the hole-free phase plate with an induced screening charge in close proximity (3 nm) to the primary beam generated charge. The same fringing field appears both above and below the phase plate. Both the diffracted beams and the direct beam pass through the electric field in the vacuum near the phase plate [1,138,139]. (b) Schematically indicates that the total phase shift $\varphi(\mathbf{r})_{\mathrm{tot}}$ can be significantly larger than the phase shift difference $\varphi(\mathbf{r})$ between the direct and diffracted beams at $q = 0$ and $q > 0$, respectively. The small diameter red region indicates the lateral extent of the primary beam induced charge, while the blue, broader region indicates the extent of the induced screening charge. While the charged patch is charge neutral in the sense than the amount of the primary beam generated charge is exactly equal to the amount of the screening charge, the difference in their respective spatial distribution leads to fringing field in vacuum and phase shift difference between beams traveling different paths through the fringing field. The factor $\frac{1}{2}$ accounts for the fact that the same phase shift is acquired both above and below the mid plane of the hole-free phase plate film.

diffracted beams at $q > 0$. The difference between the phase of the direct and diffracted beam ($\varphi(\mathbf{r})$, in red on the left-hand side) arises from the fact that the direct and scattered beam passes through different regions of the fringing field and acquires different phase shifts while passing through the fringing field. The factor of $\frac{1}{2}$ in front of $\varphi(\mathbf{r})$ and $\varphi(\mathbf{r})_{\mathrm{tot}}$ captures the fact that phase shift is acquired in the fringing field both above and below the PP.[11]

The amount of the phase shift is affected by the diameter of the charged patch, the amount of primary beam generated and the equally large amount of induced screening charge and the separation between the screening and primary beam generated charge [1]. Each of the parameters can vary during the PP settling resulting in a time evolution of the associated electric field in the vacuum near the HFPP and a resulting phase shift of the fast electron passing through the field.

Microscopic mechanisms responsible for HFPP operation

In this section, we discuss the physical origins of the HFPP operation as well as the specific properties of the resulting phase shift distribution and evolution. The microscopic mechanisms responsible for the HFPP operation are comparable to those responsible for electron-beam induced damage of irradiated samples [142] particularly in the case of an intense electron beam tightly focused on a thin film. The entire HFPP, just like a sample containing an irradiated area, is a charge-neutral object. That means that any primary beam generated charge is exactly balanced by an induced screening charge located some distance away. It is the difference in the spatial distribution of the charge generated by the primary beam and the induced screening charge that is responsible for the electric field in the vacuum and the resulting phase shift accumulated by an electron passing through the field, as implied by the Aharonov–Bohm formula.

As mentioned above, at least three different microscopic mechanisms are responsible for the HFPP operation. Fig. 10 represents graphically the various modes of the HFPP operation arising from the corresponding underlying microscopic mechanisms [116]. It is likely

---

[11] Note that the simplification in Fig. 9b may be suitable for conceptual purposes, but it is not strictly speaking correct. The detailed treatment in Section ‘A brief theory of phase plate imaging’ should be consulted.

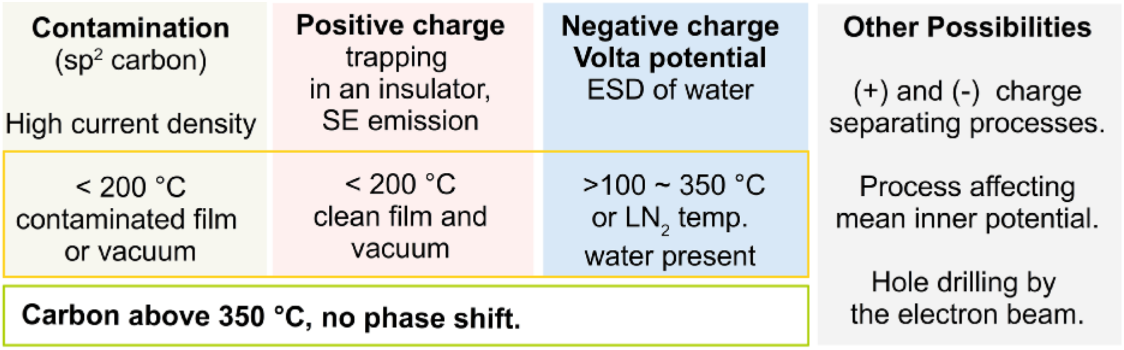

Contamination (sp^2 carbon) High current density	**Positive charge** trapping in an insulator, SE emission	**Negative charge** **Volta potential** ESD of water	**Other Possibilities** (+) and (-) charge separating processes. Process affecting mean inner potential. Hole drilling by the electron beam.
< 200 °C contaminated film or vacuum	< 200 °C clean film and vacuum	>100 ~ 350 °C or LN$_2$ temp. water present	
Carbon above 350 °C, no phase shift.			

Fig. 10. Implementations of the hole-free phase plate [116]. Several beam-induced processes can be utilized to locally modify an uniform thin film to achieve a bell-shaped phase shift profile of the high energy electron beam. For example (from the left column), carboneous contamination can build up on a film near room temperature. When the beam current density is sufficiently high, sp^2 carbon is formed under the direct beam producing phase shift proportional to the (local thickness) × (mean inner potential) [74]. Alternatively, poor conductors or insulating contamination layers can exhibit local positive charging due to an secondary electron emission that leads to an electric field in the vacuum [1]. Such poorly conducting films are typically deposited under modest irradiation doses, e.g. when the crossover with a large diameter and low current density is placed at the hole-free phase plate film. A metallic film, including amorphous carbon films at $\approx 100^\circ$ C to $\approx 350^\circ$ C or at LN$_2$ temperatures can exhibit a negative surface charge arising from the removal of the adsorbed dielectric (water) layer and the subsequent increase of the apparent work function of the hole-free phase plate film [4,116,137]. Hole drilling by a high energy electron beam can be utilized to fabricate thin-film type Zernike phase plate with a hole size well matched to the incident beam profile at the back focal plane [139]. All of the phenomena can be involved simultaneously and their relative strength is determined by parameters such as the hole-free phase plate film temperature and microscope vacuum. Additional mechanisms can be also responsible. Note that at high temperatures (above $\approx 350^\circ$ C), the primary electron beam induced phase shift was *not* observed in carbon films [116], and contamination was not observed while the hole drilling by the high energy electron beam remains [74,116,139].

that more than one of these mechanisms operates simultaneously. A contamination may form, secondary electrons (SEs) are emitted leaving a positive charge within the HFPP film, and surface adsorbants (e.g. water) are removed by electron stimulated desorption (ESD). The relative strengths of these various mechanisms can be influenced by the choice of the HFPP thin film material and its surface properties and by its temperature. It is possible that the beam current density at the HFPP plane also affects the outcome, for example by forming an sp^2 bonded carbon at high current densities rather than an insulating polymer-like contamination at low current densities.

The accumulated phase shift can be calculated via the resulting electric field if the exact beam induced and the screening charge distribution are known, as well as any topographical changes (such as the deposition or removal of PP material). Fig. 9 shows a schematic depiction of a thin film with primary beam generated (red area) and an induced screening charge (blue area) and the resulting calculated potential in the proximity of the thin film. As the beam-induced effects typically occur on both sides of the HFPP film, the phase shift determined by a single dipole (charge separation) has to be multiplied by two.[12]

Inversely, the charge distribution in the space around the PP can be obtained by power spectra analysis (i.e. FFT of image) of TEM images acquired with and without PP present in the BFP [140,141]. Depending on the electrical and microscopic properties of the film and the additional parameters such as irradiation dose or film temperature, the separation between the beam induced and screening charge can be expected to be either rather small (i.e. smaller than the irradiated patch lateral dimensions) or large (i.e. the screening charge may be many micrometers away, for example on grounded grid bars). Both scenarios can be described by a mathematical model as it was done by [1], where the resulting phase shift was calculated for distant (model **A** [1]) and near location (model **B**) of the screening charge.

In addition to the charging of the HFPP, the deposition or removal of material affects the induced phase shift of transmitted electrons. Although matter is composed of separated charges on a very small scale, i.e. electrons and atomic cores, the phase shift accumulated by electrons transmitted through matter is commonly calculated using the MIP often referred to as V_0 (MIP, Eq. (16)). In the case of a clean HFPP film (free of any adsorbents) with sufficient electrical conductivity and beam stability, only a marginal relative phase shift build-up may be observed due to the lack of charge separation or topographical/morphological changes of the film [116].

Three different microscopic mechanisms have been proposed as responsible for the HFPP-induced contrast enhancement reported in recent literature. They are:

1. **Contamination.** The build up of material on samples caused by electron-stimulated dissociation and deposition of adsorbed species has been, and is, a common problem in electron microscopy [144–146]. However, a contamination with a suitable thickness and MIP can be used as a HFPP due to the phase shift accumulated by the direct beam during transmission through the deposited matter [74].
2. **Positive charging.** In the case of a thin film or its surface with insufficient electrical conductivity, the SE emission generated by the primary beam leads to positive holes remaining in the thin film (charging). Although a screening charge may be situated in close proximity, i.e. in the conducting core of a thin film with non-conducting surface, a difference in the spatial distribution of the charge of the positive holes and the negative screening charge leads to a phase shift [1].
3. **Negative charging.** In the absence of non-conductive surface layers and contamination, i.e. where there are no physisorbed hydrocarbon molecules or their diffusion is inhibited at low

---

[12] Harada *et al.* reported that in insulating films such as SiN, the charge on the exit (bottom) surface could be smaller than that on the entrance (top) surface [143].

temperatures, negative charging is observed; this was first reported by Danev *et al.* [6] and later referred to as VPP [4]. Later studies confirmed that this potential arises from a local change in work function of the HFPP in the irradiated area due to the electron-beam induced desorption of chemisorbed (water) molecules [116,137,147], rather than from a change in the aC film structure [6].

Detailed mechanisms will be discussed in the following subsections. Additional processes are possible as any mechanism that leads to an effective charge separation will create an electric field in the surrounding vacuum. This charge separation determines the magnitude and shape of the field in the vacuum and hence the magnitude and shape of the phase shift acquired by electrons propagating through it.

Independent of the underlying mechanism, two general effects can be expected with an increasing irradiation dose: the magnitude of the charge/film modification and the resulting phase shift at $q = 0$ grow until a saturation is reached and the diameter of the charged/contaminated area increases. Both of these outcomes affect the phase shift.

Experimental methods used to analyze the formation of the phase-shifting patch include, but are not limited to, electron energy-loss spectroscopy (local thickness determination), detection of the SE signal emitted during the build up, determination of the size and magnitude of the induced phase shift by analysis of the power spectra of acquired images and imaging of the patches after the formation. Together with a variation of experimental conditions such as temperature and beam size and current density, these techniques enable study of the underlying physics of the involved processes. Nevertheless, a more direct proof of some aspects would be the direct detection of desorbed species upon electron-beam irradiation, e.g. by residual gas analysis. In a TEM under realistic conditions, this currently appears impossible as the amount of desorbed species is very low due to the small size of the irradiated patch.

Contamination build up

Contamination of samples is a very common problem in electron microscopy. The contribution of residual oil molecules in early microscopes equipped with oil pumps [144,148,149] is eliminated in modern dry-pumped microscopes, where adsorbed (hydrocarbon) molecules on the sample surfaces (and sample holder surfaces) are the principal source of contamination [145,150]. The underlying processes responsible for contamination are thus surface diffusion [151] and electron beam stimulated desorption and dissociation of adsorbed molecules [152,153]. A schematic depiction of these processes can be found in Fig. 11a–c. In TEM, the primary electron energy is too high (typically > 80 keV) to directly induce dissociation of the molecules at a noticeable rate, and therefore the induction is ascribed to the generation of SEs (< 50 eV).

The rate and shape of contamination deposition is strongly correlated with the shape and irradiation dose of the irradiating electron beam [145]. While an irradiation of a large area leads to a contamination ring as diffusing molecules are directly deposited at the electron beam border, sharp pillar-like structures result from a focused electron beam (compare Fig. 11b,c and f,h). The height of such pillars can easily be in the range of several tens of nms and thus can exceed the thickness of the underlying sample [154,74].

Multiple mitigation strategies have been proposed and are routinely applied to minimize sample contamination; among these are plasma [155] or UV cleaning [156], sample cooling [157,158] or beam showering [159]. All of these techniques aim to either remove adsorbed molecules on the sample surface or inhibit surface diffusion, but they only provide minimization of contamination for a limited amount of time. A clean sample may only be obtained by sample baking inside the vacuum [74], which of course is not suitable for heat-sensitive samples.

While contamination is primarily a disturbing effect, it can also be exploited to write structures in the nm range [160–162]. By controlling the amount and type of adsorbents on the surface, structures with specific properties (e.g. electric, magnetic) can be written, a technique called 'focused electron beam induced deposition' [163].

In the case of PPs, contamination is generally an effect that should be inhibited as the deposited matter and the potentially involved charging directly affects the phase-shifting behavior of the PP [67,76,164]. Heating to moderate temperatures of 100–200° C has been successfully applied to minimize contamination for various PP types [43,63,66,81]. Furthermore, an additional coating of the PP with amorphous carbon after its fabrication and shortly before implementation in the microscope was reported to reduce contamination issues [165,67]. However, it is probable that additional coating leads to a reduction of effects related to the local work function of the PP, an effect responsible for negative charging (Section 'Work function alteration').

Despite its negative effects on PP imaging, contamination may also contribute to the desired phase shift on a HFPP [74,147]. Consider a situation where a thin film, not necessarily made of amorphous carbon, is placed in the BFP and *not* treated to remove the adsorbed hydrocarbon molecules, and is subsequently irradiated with the direct beam, i.e. a focused electron beam with high dose rate. The deposited material leads to an additional phase shift at $q = 0$ caused by the MIP V_0 of the deposits. If the beam current density is high enough and the carbon film is of high quality (see next paragraph), no additional charging of the deposited contamination occurs, and the deposited material can be described as carbon with a high content of sp^2 bonds [74]. The absence of charging was measured by comparing the deposited contamination thickness measured by electron energy loss spectroscopy (EELS) and the induced phase shift (Fig. 11d, [74]) or the magnitude of the phase shift distribution in the BFP [147], which would be larger if charging occurred (see Section 'Work function alteration'). The studies in [74] were conducted at beam current densities around 200 C cm^{-2} s^{-1} on the HFPP (total beam current of 50–100 pA), up to three magnitudes higher than current densities applied in cryo-TEM.

However, early investigations of contamination and charging effects on a Zernike PP reported a positive electrostatic charging that was ascribed to the charge of the adsorbed hydrocarbon molecule layer [140,141] (see also next section). Although these studies provide insights, they are not directly comparable to the HFPP settings of modern microscopes; the used beam diameter on the HFPP is in the order of several μm implying a low beam current density. Additionally, the lack of data on thickness evolution makes it difficult to clearly differentiate the underlying mechanisms. There are no detailed studies about the build up of the phase-shifting patch in case of contamination under cryo-EM conditions, and it may be possible that additional charging due to insufficient dissociation of hydrocarbon molecules occurs on HFPPs at such electron doses.

A contamination-based, non-charging HFPP probably has the phase-shift distribution that gets the closest to the ideal

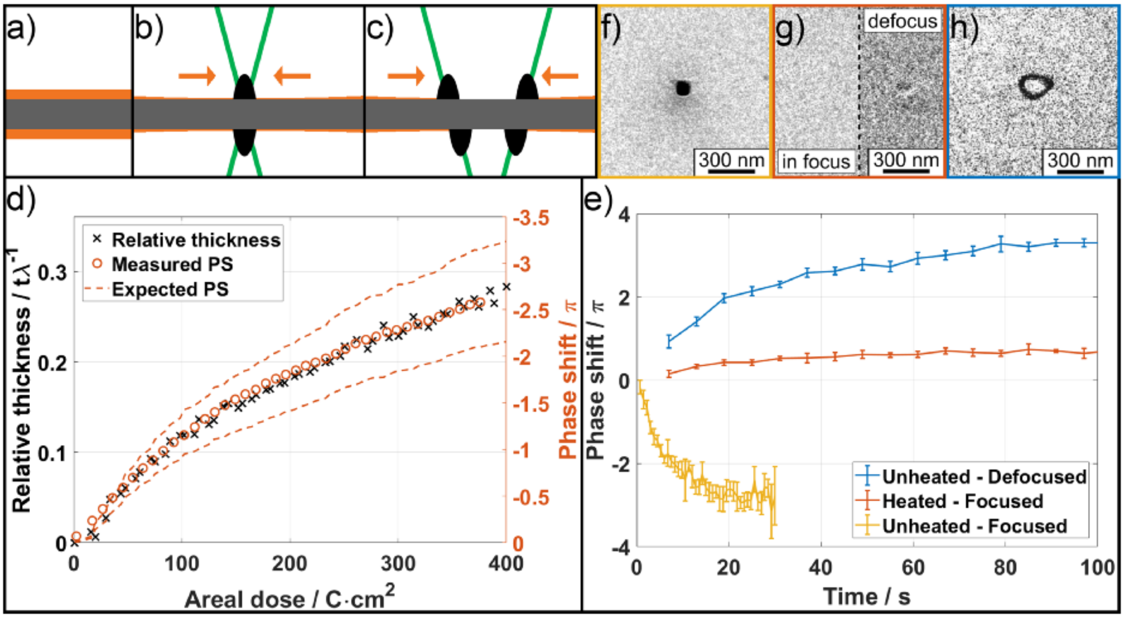

Fig. 11. Contamination and its impact on hole-free phase plates. (a–c) Schematic description of the build up of contamination on a thin film covered with adsorbed hydrocarbon molecules (orange) for (b) a highly focused electron beam, and (c) a larger beam. (d) Comparison of increasing thickness with measured phase shift showing a good agreement assuming a carbon-based material [74]. Note the negative sign on the right y-axis corresponding to a positive phase shift at $q = 0$ (see Table 2). (e) Phase shift evolution for a focused beam and an unheated, contaminated phase plate (yellow); a focused beam and a heated phase plate (red); and for a slightly defocused beam and an unheated, contaminated phase plate, with (f–h) the corresponding images of the hole-free phase plate after acquisition of the series adapted from [147].

since it almost perfectly matches the profile of the direct beam without the long-ranging tails from a charge distribution, and therefore leads to striking image contrast enhancement at low spatial frequencies [147].

This benefit is, however, outweighed by the significant drawbacks that result from the additional scattering of the direct beam in the deposited pillar and the accompanying damping of image intensity and resolution. Moreover, it is almost impossible to control the amount of phase shift if the phase-shifting pillar is grown by the direct beam itself. The reason is that the amount of adsorbents is difficult to control and fast and efficient ways to stop the growth once the necessary phase shift is reached are not yet available. Pre-structuring the deposit on the thin film [49] may help to define the phase shift but this makes a precise alignment necessary and again raises problems with contamination and charging effects.

Depending on the amount of adsorbed hydrocarbon molecules, the build up can be very fast, reaching several π and thus leading to an oscillating image contrast in a few seconds (Fig. 11d and e [74,147], or rather slow taking several minutes to reach the desired value of 0.5π (see analysis of data from [4] shown in Fig. 7 of [116]). The contamination rate is controlled by the beam current density and shape as well as by the vacuum and temperature history of the HFPP affecting the number of adsorbed hydrocarbon molecules.

A distinct situation happens when a slightly larger direct beam (>100 nm) impinges on the HFPP as it can easily occur in microscopes with only two condenser lenses. In these microscopes, a change of the condenser lens system, required for adjusting the illuminated sample area and the beam intensity in the sample plane, leads to a moving crossover position of the direct beam in the BFP in the beam direction and thus to an increase of the beam size on the HFPP maintained in a fixed position. Keeping in mind that the shape of the deposited contamination in case of a spread irradiation is ring-like [145], the deposited contamination actually may not affect the center of the direct beam at $q = 0$. Recent investigations show that although contamination is present, negative charging can occur in the central area of the direct beam (see Fig. 11e and h, Section 'Work function alteration' and [147]). Looking at the SE emission of the HFPP during the build up of the phase-shifting patch gives additional information on the underlying processes. In the case of contamination build up, an increasing signal is observed due to the increasing volume and surface of the material, and thus a larger number of generated SEs are able to leave the HFPP. This implies that, for the correct interpretation of an acquired SE trace, the corresponding thickness evolution must be known.

We also note that electron beam induced film sputtering takes place at the same time as contamination is deposited [159,166]. However, the rate of film drilling by electron beam induced sputtering tends to be lower than the deposition rate of contamination unless the contamination is severely suppressed, e.g. by high temperature.

Positive charge build up

Irradiation of a film by high energy electrons results in a SE emission [167–170]. Scanning electron microscopes (SEMs) rely on this mechanism to generate images. SE emission leaves a positively charged hole behind in the irradiated material. When a conducting film with a clean surface is irradiated, the positive hole is filled by a free electron within the film within attoseconds to a few tens of femtoseconds [171–173]. When the material is an insulator, semiconductor or a metal covered by an insulating (contamination) layer on its surface [174], the holes left behind by SE emission can last for a long time and lead to the trapping of a positive charge in the irradiated area. An equal amount of negative screening charge is induced on nearby conductors or within the conductive core of the film [1]. The presence of a few nm thick light element insulating contamination layer on a HFPP film may be difficult to observe in an image of the HFPP film. At the same time, the effect on the phase shift arising from the charge trapped in the insulating contamination and the electric field it generates in the vacuum outside the film can be large, when integrated along the fast electron beam path (see Fig. 9 and Section 'A brief theory of phase plate imaging') [1,38].

The positive charging due to SE emission has been studied extensively in the context of radiation damage [175], Auger electron spectroscopy, surface analysis and imaging [176–187]. The lateral distribution of SEs propagating within the irradiated film in the a perpendicular direction to the high energy electron beam is discussed, for example, [169,188].

Positive charging under high energy electron beam irradiation has also been studied by the cryo-TEM community, because of its detrimental effect on the quality of cryo-TEM images [189–191]. Recently, Harada *et al.* [143] and Russo and Henderson [192] pointed out that some of the emitted SEs may land back on the irradiated film some distance away from the irradiated area creating a ring of negative charge around a positively charged central area that is irradiated by the primary beam. The vitreous ice samples in cryo-TEM are known to be poor conductors with an embedded carbon or Au support film whose conductivity is higher than that of the ice, and this may possibly be an analogous to carbon film covered by an insulating surface layer [139,143,193].

The SE current, $I_{SE\alpha}$, which is defined by the number of electrons that leave the thin film, is proportional to the incident current I_0:

$$I_{SE\alpha} = Y_{SE\alpha}(t) * I_0 \tag{32}$$

Here, $Y_{SE\alpha}$ is the time-dependent SE yield, that decreases as the positive charge accumulates and the associated positive potential increases [177,183,194].

At a steady state, $I_{SE\alpha}$ is compensated by a current from the ground I_G. Therefore, $Y_{SE\alpha}$ can be estimated from measured I_G and I_0 obtained using the set up in Fig. 13. I_G measures the electron beam-induced current (EBIC) from the ground that compensates for the holes left behind the emitted SEs α. When the holes are trapped in an insulating surface layer the I_G has to pass through this layer either by dielectric breakdown, or by the tunneling or hopping of electrons. $I_{SE\alpha}$ and I_G both decrease with the irradiation dose due to the increasing number of positive holes and the increase in arising positive potential [176,175]. The surface potential increases as $\approx \log(\frac{t}{\tau})$ or $\approx (1 - e^{\frac{-t}{\tau}})$ with characteristic time τ which is affected by the film temperature [4,138,176] resulting in a corresponding rate of change of the contrast transfer function.[13]

We now turn to the mechanisms compensating for the charge left behind by the SE emission. Two conceptually different mechanisms can occur to compensate for the positive charge within the insulating layer or located on its surface: dielectric breakdown or, tunneling and hopping of electrons through the insulating surface layer.

Dielectric breakdown occurs when the electric field exceeds the dielectric strength of the insulator, typically $\approx 10^7$ Vm^{-1} but up to 10^9 Vm^{-1} for example, in diamond. The phase shift measured in HFPP experiments corresponds to a fraction of a Volt to slightly over 1 V potential [1,189,192,195]. Taking into account the dielectric strength of insulating layer, even a couple of nm thick layers could provide sufficient charge trapping capability to explain the positive potential corresponding to the measured phase shift without suffering dielectric breakdown. Large electric fields are known to induce damage of the irradiated film [175].

An alternative mechanism of charge compensation is the tunneling or hopping of the charge through the insulating contamination. There are many variations of the charge tunneling and charge hopping concepts, some of them more sensitive to temperature than others [196]. All of the tunneling and hoping mechanisms are highly asymmetric in the sense that a small increase in electric field across a barrier leads to a significant sometime exponentially larger increase in the current through the insulating barrier (see Fig. 12). While the details of the particular tunneling or hopping mechanism may not be critical, we note that a potential of a fraction of a Volt to a few Volts appear to be typical for the barrier thickness of a few nm [196] and would explain the phase shift observed in HFPP imaging.

Figure 12(a) illustrates the processes involved in the primary beam generated positively charged area. A film that is either a poor conductor or has a poorly conducting surface (contamination) layer can trap positively charged holes left behind following an SE emission [169,178,189,192,197]. The incident high energy electron beam generates two types of SEs: those that escape from the film to the vacuum (SEα) and those that travel in the plane of the film (SEβ). SEα change the charge balance in the film that is compensated for by the EBIC from ground I_G. The latter result in a redistribution of charge in the plane of the film, change in film electrical properties and additional SEα through cascade processes [169]. The SEα emission continues to build up charge and associated potential until the electric field becomes sufficiently strong to draw a compensating current I_G from the grounded part of the film, e.g. the conducting film core [193], (see Fig. 12b). The trapped holes within an SEα escape depth (the red layer in Fig. 12b) are compensated by a tunneling current I_{tunnel} (black vertical arrows) that combine to a total EBIC current from ground electrode I_G (green horizontal arrow).

Figure 12(c) draws sample I–V characteristics for possible scenarios involving, for example, Fowler–Nordheim, Poole-Frenkel and Schottky tunneling mechanisms [138,139,196]. The charged patch steady state corresponds to a SEα emission current equal to compensating I_G, that is the intersection of the SEα current (purple) with the corresponding tunneling current. While each of the various mechanisms result in somewhat different values of positive potential, they all require a fraction of a Volt to a few Volts across the

[13] Note that the effective SE yield $Y_{SE\alpha}$ decreases with the irradiation dose for *both* positive and negative primary beam-generated charges. Regarding positive primary beam generated charges (Section 'Positive charge build up'), the increasingly positive charge increases the potential that an SE needs to overcome by virtue of being trapped in the positive potential associated with the positive charge. In the case of negative surface potential (Section 'Work function alteration'), the increase of the work function arising from the removal of the water layer by ESD has the effect of increasing the energy barrier from the Fermi level to the vacuum level that an SE has to overcome to be released from the irradiated film. However, an insulating (contamination) layer covering a metallic film may have a higher intrinsic SEα yield than the metallic film it covers.

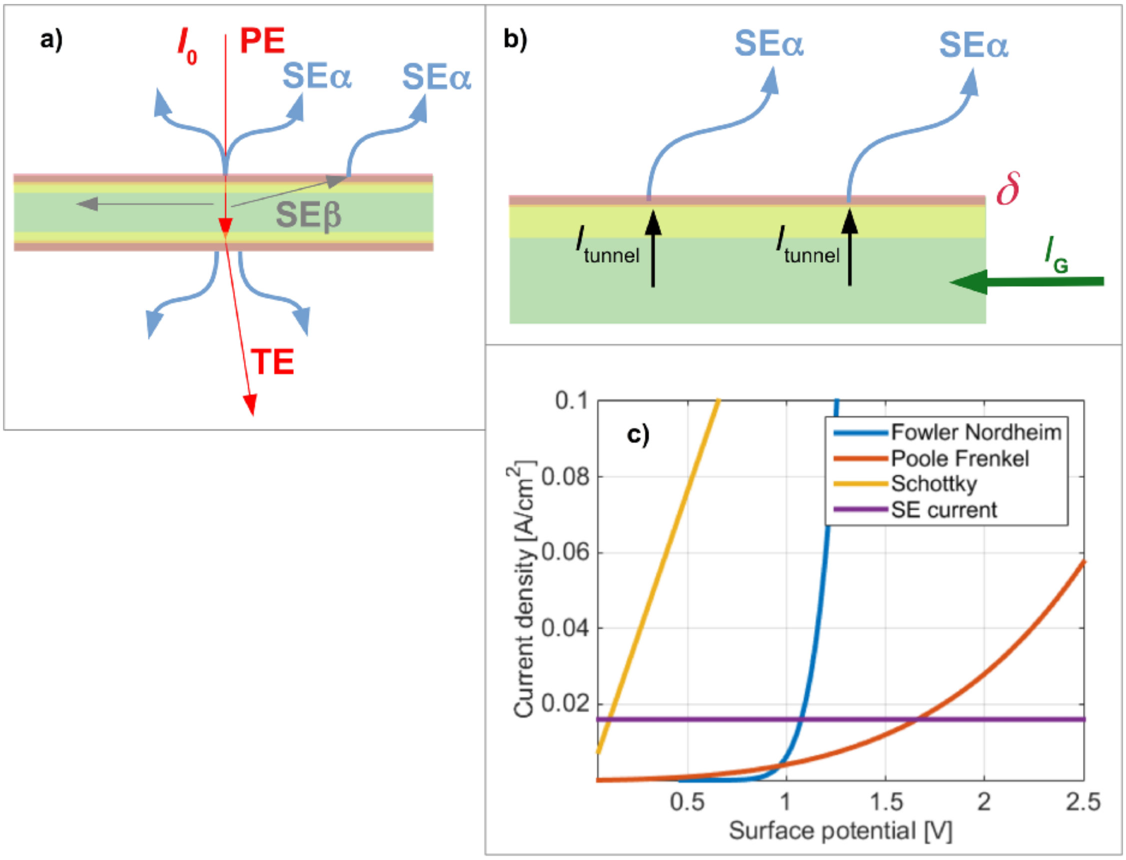

Fig. 12. Processes involved in generating and maintaining positive beam-generated charge in a film with an insulating surface layer. Primary electrons generate two types of secondary electrons, either escaping from the film into vacuum (SEα) or propagating within the film, called SEβ for some distance while possibly generating additional SEα away from the primary beam location. The primary electron then escapes as a transmitted electron [169,188]. (a) Indicates the electron labeling. As shown in (b) a SEα escapes from the sample. In the presence of an insulating layer (yellow) or if the film itself is an insulator, the SEα emission leaves a positively charged hole trapper within SEα escape depth. The positively charged holes attract mobile charges within the film (green) and, when sufficiently strong electric field builds up, the screening negative charge crosses the insulating barrier and compensates the positive hole. c) Plots of I–V characteristics for several possible processes involved in electron crossing of the insulating layer [139,196]. The intersection of the secondary electron current with the I–V characteristics for the various tunneling processes indicates the steady state potential [176].

insulating layer to operate. This potential range is in agreement with the potential needed to obtain the phase shift measured in an experiment [1,139,192]. The corresponding electric field for a fraction of a Volt to a few Volts applied over a few nm thick insulating layer [193] amounts to $\approx 10^7$ to 10^9 Vm^{-1} that is near the dielectric strength of a possible insulating layer. As was indicated above (Section 'Microscopic mechanisms responsible for hole-free phase plate operation' and Fig. 9), the charged patch is a charge neutral object, i.e. its trapped positive charge is exactly compensated by an induced screening charge.[14]

The experimental set up in Fig. 13a in a Hitachi HF-3300 TEM has been used extensively to study the effects of high energy electron beam irradiation on a thin film [74,116,137–139]. It allows collection of the time evolution traces of the SE emission current $I_{SE\alpha}$, of a time stack of EELS and of the phase shift $P_Z(q)$, which is extracted from a stack of images with a test sample placed above the HFPP film. Additionally, the incident beam current I_0 and the EBIC drawn from the ground electrode I_G to compensate SEα emission can be measured. The thin film can be biased up to several tens of Volts to investigate the effect of bias on SEα emission. The ratio of $Y_{SE\alpha} = \frac{I_G}{I_0}$ provides an estimate of SEα yield $Y_{SE\alpha}$.[15]

The experimental traces in Fig. 14 were collected using this set up. Fig. 13b shows a calculated distribution of number of SEs per energy interval $\frac{dN}{dE}$ for sample work functions $\Phi_W = 2.5$ eV and $\Phi_W = 6$ eV [169]. It indicates that even for $\Phi_W = 6$eV, the vast majority of the SEα are ejected with energies below ≈ 20eV and should be sensitive to the positive bias of a sample of comparable

---

[14] We note that at high current density $> 10^2$Acm^{-2} and high dose $> 10^3$Ccm^{-2} of the high energy electron beam, as often encountered at the beam cross over in HFPP imaging, a conducting sp^2 bonded rather than insulating carboneous contamination is deposited [74]. However, when the beam current density is not high, as in case of large cross over [3,4,12,140,141,165] an insulating layer trapping positive charge can develop. It is also possible, that the low current density within the tails of the high energy electron beam, including the scattered electrons at $q > 0$ is sufficiently low to deposit contamination that is initially insulating and could contribute to, for example to *aging* of thin film type ZPPs [43,165].

[15] The SEα are emitted from both top and bottom surfaces. A factor of two must be included to obtain the number of SEα per incident electron per surface.

magnitude. Fig. 13c shows a steady state SE yield $Y_{SE\alpha}$ measured as a function of the film bias between −45 V and +63 V relative to the microscope ground. Fig. 13c can be related to (b) by integration over the energy axis (x abscissa) in (b). Fig. 13d shows experimental confirmation of both positive and negative bias of aC HFPP. The upper two data sets (red solid symbols) correspond to two Thon ring time evolution acquired at 200°C, while the lower two data sets (blue, empty symbols) correspond to Thon rings acquired at room temperature (RT) under otherwise identical conditions [138].

The decrease in $Y_{SE\alpha}$ in Fig. 13c does not imply that the asymptotic local potential and phase shift of a HFPP can be controlled by biasing the entire PP film. On the contrary, it demonstrates that there is a fraction of high energy SEα that are emitted at high bias. Presumably, the bias of the HFPP film can affect the settling time as the decrease in $Y_{SE\alpha}$ at positive film bias implies a lower SEα current and therefore a slower approach to a steady state. The small difference in $Y_{SE\alpha}$ dependence on bias between the studied materials arises from the similarity of the $\frac{dN}{dE}$ in Fig. 13b and the possibility that a contamination of a similar nature may be present at the surface of the samples even at the $< 5 \times 10^{-8}$ torr residual pressure in the Hitachi HF-3300 TEM. A biased film placed in the column also acts as an additional electrostatic lens, similar to [16,198].

Figure 14b shows the measurement of the SE escape depth δ. The same experimental set up as used for Fig. 13a was utilized to obtain the data. In agreement with static measurements of Glaeser and Downing [193] in Fig. 14a the escape depth $\delta \approx 3$nm (see Fig. 12) was measured under 300 keV electron electron beam irradiation, Fig. 14b. The electrical properties of the same, ≈ 13 nm thick aC film, used as a HFPP were measured at LN$_2$ temperature, Fig. 14, see [137].

SEα emission and film charging is also thought to be responsible for aC aging in thin-film type ZPPs [43,165]. Essentially, the mechanisms that make it possible to operate a uniform thin film as a HFPP act in addition to the step in MIP× thickness used for thin-film type ZPP. Fig. 4 indicates that heating a carbon film above 350°C can perhaps improve the usability of thin film type ZPP, leaving only the challenges of hole alignment and bright field transmission electron microscopy-like transfer up to the cut on frequency q_C

Work function alteration

While positive charging HFPPs are in line with numerous studies of positive electron-beam induced charging (as discussed in Section 'Positive charge build up') the reported negative charging of a HFPP [4,6] may not be obvious. The underlying mechanism is based on a work-function change resulting from ESD that may be observed in the absence of (hydrocarbon) contamination and the (positive) charging of non-conductive layers of the PP.

Heating the carbon film to 150–250°C inside the vacuum of a TEM leads to desorption of the phyisisorbed hydrocarbon molecules responsible for the deposition of contamination due to their low adsorption energy (Section 'Contamination build up' and Fig. 10). Nevertheless, chemisorbed species can adsorb with energies significantly higher than the thermal energy available at moderate film temperatures (30–45 meV) and thus are not, or not completely, removed at these temperatures. It is a reasonable assumption that water, being the most abundant species in the residual gas atmosphere of a TEM, is the main component of this chemisorbed layer above ≈ 250°C.

Research conducted on water adsorption on clean metal surfaces has demonstrated that the water molecules tend to orient themselves with the positive charge (H$^+$) pointing in the direction of the vacuum thus forming a dipole layer on top of a carbon thin film [199]. This dipole layer forms a potential step δV for electrons passing through it whose value is negative and of the order of a few tenths of eV. This potential step can be considered as an effective decrease of the work function of the underlying metal [200–203].

Irradiation of the carbon thin film with highly focused electrons causes ESD of the adsorbed molecules [152] leading to a restoration of the original work function of the carbon film in the irradiated area. The cross section for primary electrons inducing ESD is very small and SEs are mainly responsible for ESD (Fig. 15a). The resulting situation is equivalent to a central patch near $q = 0$ being at a negative potential, which is caused by a corresponding charge redistribution in the carbon thin film as a result of change in the film work function (Fig. 15b).[16] The phase shift acquired by an electron propagating through this patch at negative potential, and the electric field in the vacuum near the film, is governed by two parameters, namely the change in work function caused by the adsorbed (water) layer δV, and the size of the patch with restored work function as represented by its radius R [116]:

$$\phi_{\mathrm{VPP}} = C_E R \delta V \tag{33}$$

An estimation of attainable values for δV can be obtained by calculating the potential step arising from a perfectly aligned monolayer of water on the HFPP film and a clean area of the film, leading to ≈ 4 V. Studies on the alteration of metal work functions caused by the adsorption of water showed a saturation once a monolayer is reached [199]. Therefore, the ≈ 4 V value can be seen as an upper limit. Under experimental conditions, δV is expected to be smaller due to only partial coverage and non-perfect orientation of the water molecules due to structural relaxation and HFPP film surface roughness.

The phase shift build up follows a double asymptotic evolution with two different time constants [4,116,137]. It is plausible, that the fast time constant can be linked to ESD of the adsorbed molecules in the area of the intense direct beam, which is the dominating process up to a dose q_1. The slow time constant is given by a subsequent increase in the size of the film patch cleaned by ESD, caused by electrons scattered to low angles, spatially located close to the direct beam (Fig. 15e-g).

Although this model leads to a simple dependence between the phase shift and model properties (δV and R), an experimental control of these properties is only indirectly achievable. The thin film temperature and vacuum in the column determine the coverage of the PP with adsorbed water molecules and thus δV, which is also affected by the thin film surface roughness. On the electron-optical side, the beam current determines the rate of the phase shift build up, while larger crossover size leads to an increased R and consequently to a higher phase shift. An impact on the second time constant may also be expected from the varying number of electrons scattered from the sample. In addition to these global parameters, the properties of the carbon thin film vary locally (e.g. surface roughness, impurities) and will slightly change the behavior of the HFPP

---

[16] As with the positive primary beam generated charge, an induced screening charge (in this case positive) forms near the irradiated patch. The difference in the spatial distribution of the primary beam generated (negative) charge and the induced (positive) screening charge sets up an electric field in the vacuum outside the film.

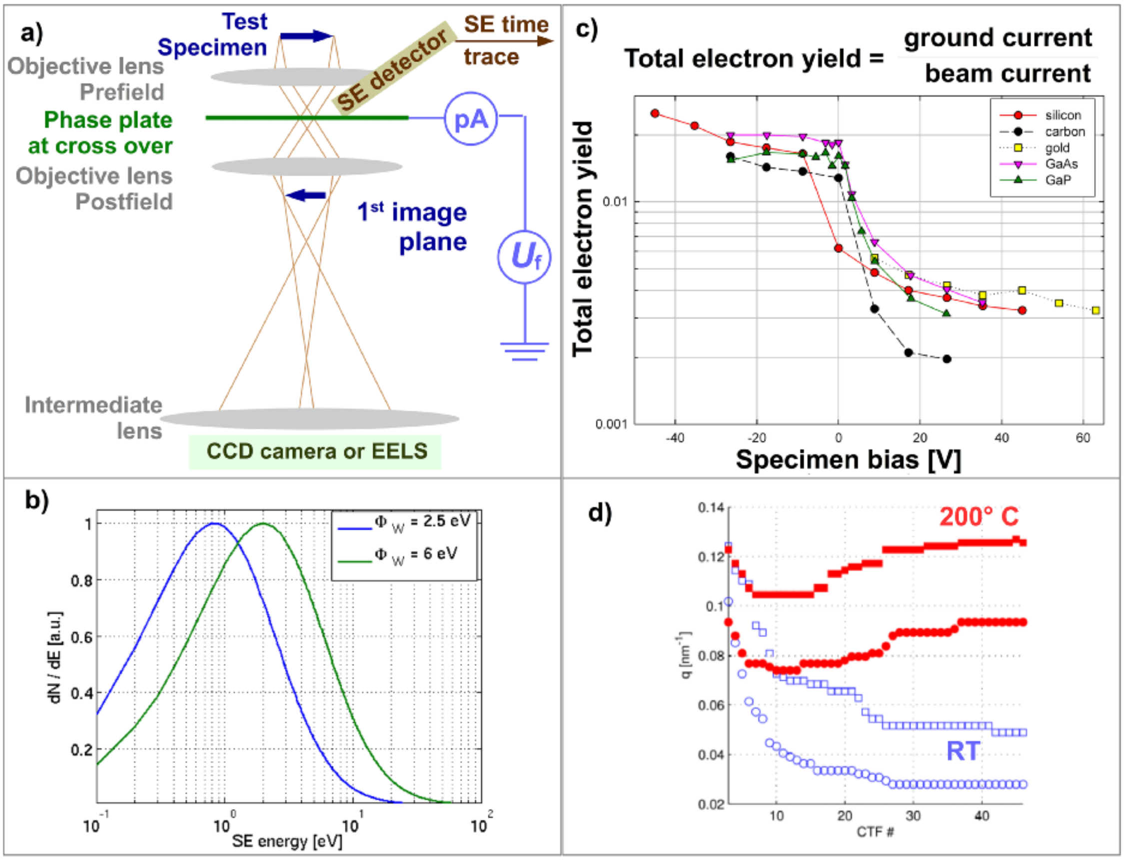

Fig. 13. (a) An experimental set up that allows us to *simultaneously* measure time series electron energy loss spectra, time trace of scanning electron emission intensity and the electron beam induced current from ground I_G compensating for the scanning electron emission current $I_0 \times Y_{SE\alpha}$. Alternatively, the electron energy loss spectra spectra time trace can be replaced by a time-evolution stack of images that provide contrast transfer function and the phase plate phase shift $P_Z(q)$. A bias voltage can also be applied to the phase plate while the measurements are performed. The incident current I_0 can be estimated from images or measured by a Keithley 6485 picoampere meter. (b) Simulated SEα emission energy distribution [169] for two example work function values $\Phi_W = 2.5$ eV and 6 eV. (c) scanning electron yield from both top and bottom surfaces of several thin films as a function of the film bias voltage relative to the ground. The scanning electron yield $Y_{SE\alpha}$ was taken as the electron beam induced current from the ground I_G divided by the total incident high energy 300 keV beam current I_0. (d) The evolution of Thon ring positions determined from image stacks acquired at room temperature (blue empty symbols) and at 200°C (red solid symbols). Second minimum (circles) and maximum (squares) are plotted at both temperatures. The change in direction of the Thon ring evolution with temperature indicates a change from positive to negative charging of the hole-free phase plate film [4,138].

depending on the location used on the film. We note that there may be large differences among aC thin films fabricated by various techniques. Finally, adsorption and desorption are not instantaneous processes, the behavior of the HFPP can also depend on the film history, e.g. microscope vacuum, temperature and previous irradiation. This complexity has led to a common approach to experimentally determine the settings that lead to the best suited phase-shifting profile [133].

Direct proof of this model has not been performed; it would be shown, for example, by a detection of desorbed water molecules during the build up or a scanning tunneling microscopy measurement of the reduced work function after the electron beam irradiation. However, the experimental studies reported so far strongly support it [4,116,137,147].

Figure 15c compares the measured phase shift evolution from published data for different experimental conditions [4,116,133,137]. Although the beam diameter on the HFPP might vary from one experiment to another, three general effects may be discerned:

- The phase shift obtained in cryo microscopes is higher than in microscopes with the sample at RT (red curves in Fig. 15c. This may be due to the larger amount of water vapor in the column and thus a resulting increase in δV.
- Porous thin films that typically have a large surface area, allow for higher observed phase shifts (dashed lines in Fig. 15c). A large surface area leads to a large number of adsorbed molecules and thus a higher phase shift.
- Although heating the HFPP is the usual way to obtain a negative phase shift, other techniques that inhibit contamination but do not remove adsorbed water molecules are also possible. They include cooling down to liquid nitrogen temperature (blue line), UV cleaning (solid black line) or defocusing the beam on the HFPP at RT (see blue line in Fig. 11e).

The measurement conducted with the HFPP at LN$_2$ temperature requires further discussion [137]. It confirms the presented mechanism because the low temperature leads to strong adsorption on the HFPP while also freezing surface diffusion and thus inhibiting

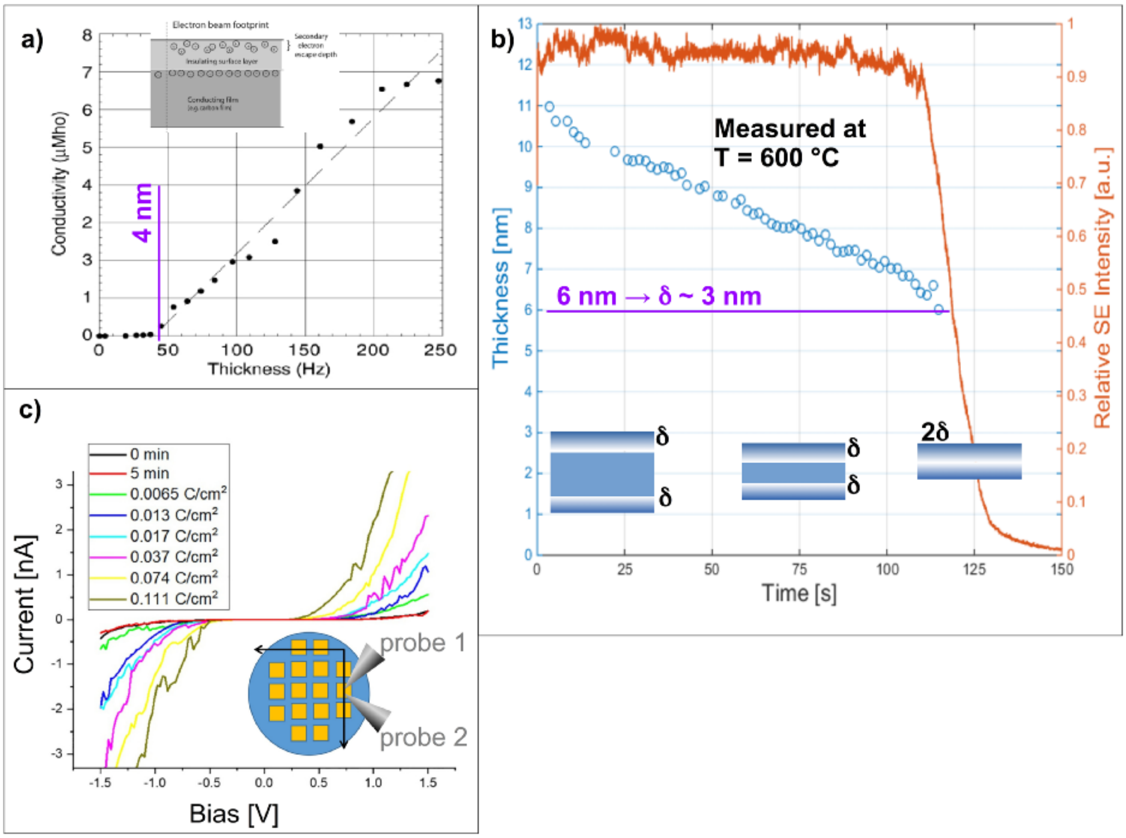

Fig. 14. Electrical properties of a thin amorphous carbon film. (a) Electrical properties measured *ex situ* indicate an insulating behavior of amorphous carbon thin films with thicknesses below 4 nm. Reprinted from [193]. b) *In-situ* measurement of SEα signal dependence on amorphous carbon film thickness. Thickness was measured by EELS while the SEα signal was measured by an Everhart–Thornley detector in the set up shown in Fig. 13. The thin film was held at 600° C to prevent film contamination. The film thickness decreases due to the electron beam film drilling [159,166]. The loss of SEα signal when the film thickness reaches $\approx$6 nm indicates about 3 nm SEα escape depth δ (Fig. 12, because the SEα escaping from both top and bottom surface is not affected until thickness becomes comparable to SEα escape depth δ [139]. (c) The I–V characteristics of an aC film at liquid nitrogen temperature for several values of a 10 keV electron irradiation dose [137]. The film becomes more conducting with an increase of the 10 keV beam irradiation dose. The conductivity becomes closer to Ohmic with an increasing irradiation dose.

(hydrocarbon) contamination buildup. The measured phase shift is thus strongly increased (larger δV) and even a slight decrease in the thickness of the film is observed that can be linked to the removal of the adsorbed molecules [137]. This approach seems to lead to a suitable phase shift evolution while avoiding the presence of a heated thin film in close proximity to a cryo sample. However, it requires a specific HFPP holder that allows cooling. Although long-term studies have not yet been reported, possible problems include continued buildup of adsorbed material with time making the control of the asymptotic phase shift difficult. Moreover, the continued buildup of adsorbed material could lead to a HFPP that more closely resembles a thin film embedded in ice, i.e. a cryo-TEM sample, where positive charging is observed [192].

The phase shift distribution of a negatively charged HFPP closely resembles the direct beam profile but has a larger spatial extension. A generic spatial distribution of the phase shift (dependent on R) resulting from calculations of the electric field is displayed in Fig. 15d [116]. The phase shift first drops fast with increasing distance from the direct beam at $q = 0$ and reaches a value of about 25% at $2R$, i.e. double the size of the patch with restored clean-film work function. This fast drop is followed by a slow decrease up to rather high spatial frequencies. Modeling the phase shift as a combination of a narrow Gaussian beam and a longer-ranging Lorentzian tail yielded an accurate description of the observed image contrast including the presence of halos at the edges of WPOs [147].

The fact that ESD is induced by SEs rather than PEs leads to R being significantly larger than the actual primary beam diameter on the HFPP due to the possibility of SEs traveling in the plane of the film (see Fig. 12). An estimation of the spatial extension of the phase-shifting distribution on the HFPP indicates that R is about 10–20 times larger than the actual beam diameter on the HFPP [116,147].

Monitoring the SEα trace during the build up of the negative potential leads to a rapid drop of the signal before reaching a plateau [116]. This trend can be attributed to the increasing work function in the central patch, which can be considered as an additional energy barrier for SEα. The number of escaping SEα thus decreases until the work function is completely restored in the vicinity of the direct beam.

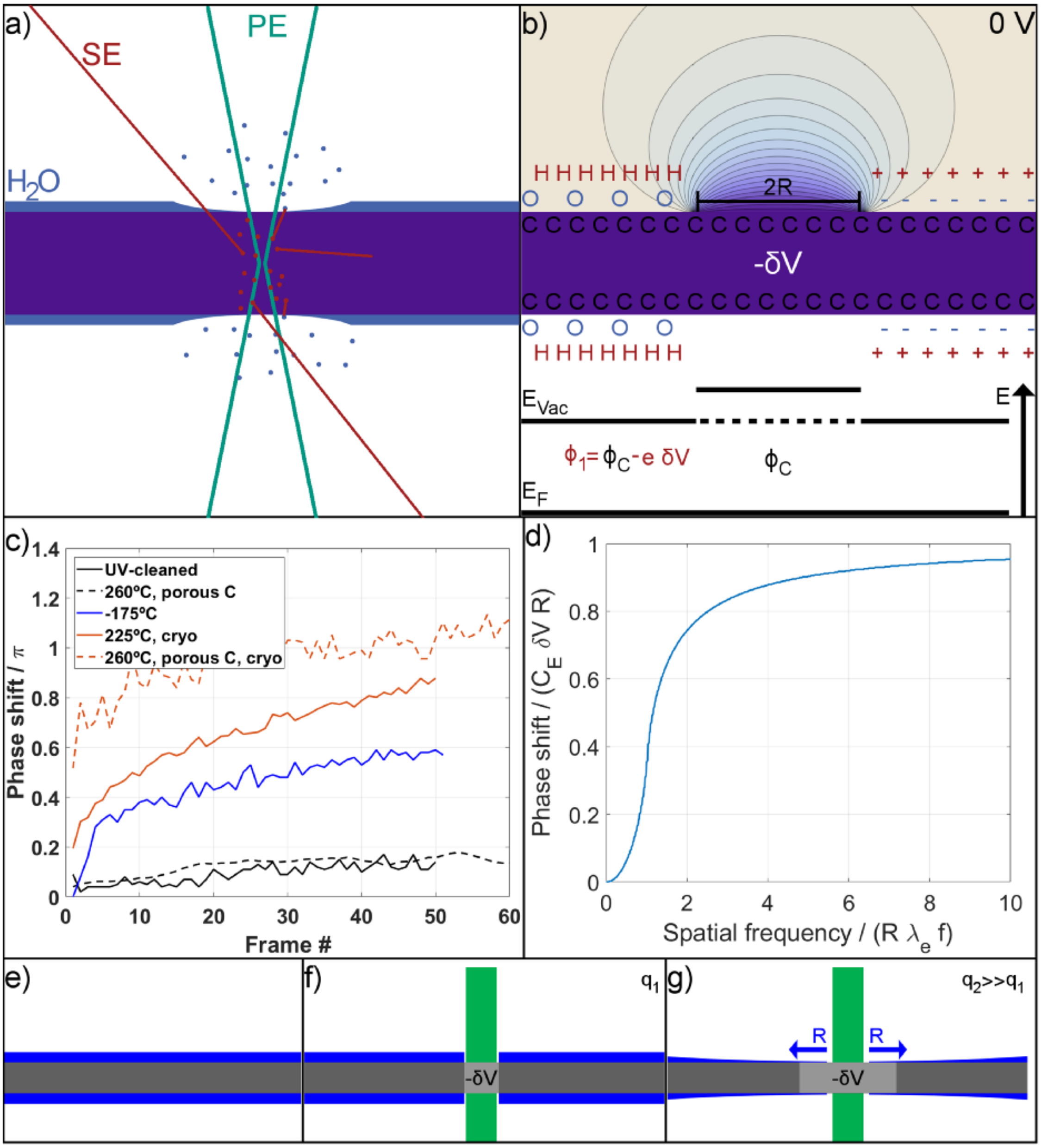

Fig. 15. (a,b) Schematic illustration of the mechanism responsible for negative charging of hole-free phase plates. (a) The hole-free phase plate is irradiated with the direct beam primary electrons (green), and generated secondary electrons (red) in the C thin film (purple) can initiate the desorption of adsorbed H_2O molecules from a surface layer (blue). (b) The adsorbed water layer is likely to form a dipole layer with the hydrogen (+) pole pointing to the vacuum which effectively reduces the work function (ϕ) by δV. The potential distribution (range from $-\delta V$ (purple) to 0 V (beige)) for a hole-free phase plate with a restored wave function in area $2R$ is shown in the upper half. (c) Comparison of published phase shift evolution from [137] (blue), [116] (black), [133] (dashed red) and [4] (solid red). (d) Generic phase shift profile of an electron passing through the potential depicted in (b). The phase shift is plotted in units of $C_E\ dVR$ over the spatial frequency in units of $R\lambda_e f$ with C_E being the interaction constant, dV the potential difference, R the patch radius, λ_e the electron wavelength and f the focal length. (e–g) Schematic illustration of the mechanisms responsible for the two time constants that correspond to (f) the restoration of the work function in the central patch at small doses q_1 and (g) the enlargement of R caused by scattered electrons, which remove water also outside the direct beam patch observed for a higher direct beam dose q_2.

Applications of HFPP

The HFPP was first demonstrated on elk fibrils, 10 nm diameter carboneous rods and ≈ 5 nm diameter CdTe nanoparticles [1] establishing suitability of HFPP for both biological and materials science applications. In the following sections, we summarize some of the ground-breaking demonstrations of HFPP applications. We discuss the initial demonstration for a particular application even if the current state of the art exceeds the performance demonstrated at that time. We do so mainly to include reports that contain, in our opinion, a correct interpretation or a detailed explanation of the experiment.

Following the first HFPP demonstration the aim (especially of the biological sciences community) has been increasing spatial resolution by means of the HFPP in its various implementations, e.g. Volta (V)PP.

It is well understood that a PP can reduce the irradiation dose allowing detection of objects by virtue of improved transfer of low spatial frequencies and consequently an improved signal to noise ratio [8]. The improved signal to noise ratio does not imply an improved electron-optical spatial resolution. However, the effective resolution for beam-sensitive specimens is the dose-limited resolution (DLR), which depends on the contrast in the image, as well as its collection efficiency and the electron dose [204]. By increasing image contrast, the HFPP improves the DLR. Increasing the signal to noise ratio at low spatial frequencies helps with accurate alignment of multiple images, as required in single-particle cryo-EM. This signal to noise ratio requirement leads to a comparison with electron tomography where sub-pixel alignment accuracy can be obtained using large fiducial markers [205].[17]

It is possible that the greatest impact can be achieved in applications where the HFPP enables observation of phenomena that are not observable by other means. It is also possible that new applications may arise in materials science and physics, when the ability to obtain contrast in the first place, e.g. long range magnetic fields together with sample microstructure, is more critical than improving spatial resolution. The ease of implementation and the ability to observe changes taking place in the TEM specimen could also prove to be more meaningful than a quest for incremental improvement of spatial resolution.

Biological sciences applications

The original motivation and the initial drive for the entire field of PP imaging in a TEM was the desire to image radiation sensitive biological samples [16,43,44,46,51,117,122,210–216]. The early successes of thin-film type ZPP devices led to extensive efforts to correct for its imaging artifacts and to develop new types of devices, e.g. the Börsch PP (Table 3) [21,22,25,62,88,217–219]. We briefly review the progress in the application of PP imaging in TEM to biological samples focusing on HFPP applications.

Examples of thin film type ZPP results that motivated the field of PP include imaging of GroEL protein molecules and T4 phage [44,212], imaging of liposomes [220], lipid nanotubes [221], cryo imaging of DNA complexes [222] and the study of influenza A virus particles using single particle analysis methods [223,224]. The samples are usually held near LN_2 temperature, although some of the early ZPP results were obtained using negative stained samples, e.g. horse spleen feritin [225]. A thin film type ZPP has been used successfully to image organic biomolecules in their native environment [84,226,227]. Alternative, non-centro-symmetric differential phase-contrast methods were also tested in the context of biological sample imaging [52]. An achievement of great importance was the demonstration that, despite the contrast ringing artifacts, a thin-film type (quoted from [46]): '*ZPP imaging is more effective as to particle identification and also sorting of orientations, conformations and compositions. Moreover, our analysis on image alignment indicates that ZPP can, in principle, reduce the number of particles required to attain near atomic resolution by 10-100 fold for proteins between 100 kDa and 500 kDa*'.

Despite aging and ringing issues, the thin film type ZPPs were sufficiently stable to demonstrate PP electron tomography of biological samples, including three-dimensional (3D) imaging of entire cells [45,54,85,131,228–238] and bacteriophagae [239]. Hosogi *et al.* imaged a flagellal motor in three dimensions using a ZPP [211,240]. However, a problematic issue in biological sample imaging is contrast ringing at the object boundaries in ZPP, which interferes with the true rendering of electron tomography results [89,241]. The challenges encountered in biological sciences applications of pre-HFPP generation of PPs and their solutions are extensively summarized in [242].

The results mentioned above indicated the huge potential of PP imaging in biology, but the artifacts arising from contrast ringing and issues of PP aging continued to frustrate efforts toward applications [43,95,117,243–245]. With the advent of HFPP, the contrast ringing artifacts and the issues of ZPP aging were resolved or, more precisely, put to good use (Fig. 5) [1,4]. Furthermore, artifacts specific to the HFPP, such as the lack of periodicity of contrast with PP-phase shift are understood [38]. These developments qualitatively improved (cryo-TEM) biological applications of PP imaging.

Figure 16 illustrates the impact of HFPP applied to biological samples. The HFPP allows elimination of the staining of histological tissue samples by toxic heavy metal salts, Fig. 16a. The increased contrast without the need for toxic staining may prove to be important for histology laboratories and hospitals. The ebolavirus images in Fig. 16b exhibit high contrast and do not exhibit the sometimes misleading high-pass filtered appearance typical of defocused bright field transmission electron microscopy. The resolution of the three-dimensional reconstruction of the ebolavirus was about 0.6 nm. Sub 0.3 nm resolution obtained with cryo-TEM, HFPP and a direct electron detector in Fig. 16c indicates that the HFPP does not have a detrimental effect on high resolution information transfer, and perhaps allows improved image alignment [134]. Single particle analysis methods were utilized with HFPP [246,247] and viral RNA structure has also been investigated [248]. HFPP electron tomography of entire cells utilizing an up to about 400 nm thick cryo-TEM sample by Fukuda *et al.* [131] (Fig. 16d) illustrates the improved 3D rendering of HFPP as compared to ZPP cryo tomography [229,239,249–251] and Hilbert PP tomography of entire cells [252].[18]

Danev *et al.* demonstrated that a HFPP does not affect high spatial frequencies and, as a matter of fact, fewer particles need to be averaged when HFPP rather than bright is used [134,209,253,254]. At the same time, the CTF damping envelope of HFPP imaging is reported to be similar to bright field transmission electron microscopy [255,255] (see Section 'A brief theory of phase plate imaging'). Thus, while the HFPP does not improve the spatial resolution as compared to bright field transmission electron microscopy

---

[17] To obtain resolution directly, methods that improve the transfer of high spatial frequencies, such as direct electron detectors, high order aberration correction [206,207], effective focal length modulation [198] or high voltage modulation [208] could prove more fruitful [209]. Indeed, current knowledge indicates that such methods can be combined with HFPP.

[18] Fukuda *et al.* also provide a detailed account of the microscope set up for low dose cryo-TEM imaging, including the adjustment of condenser pivot points for low and high magnification observation [131], also in [132]

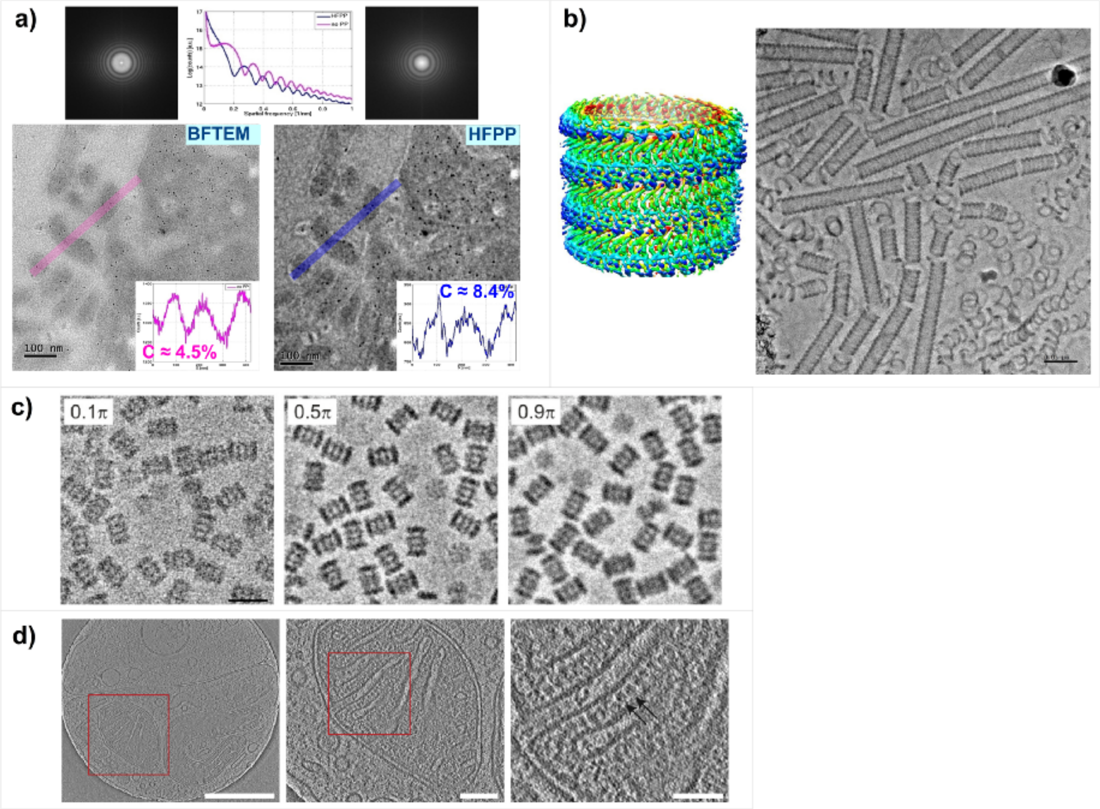

Fig. 16. (a) Images of unstained mouse kidney. The left panel shows a zero-loss filtered bright field transmission electro microscope while the right panel shows a zero-loss filtered hole-free phase plate image of the same area. The intensity profiles taken along the lines indicated in the images show a ≈2× increase in image contrast in the hole-free phase plate image compared to the bright field transmission electron microscope one. Data were collected in JEOL 2200 FS at 200 kV with the hole-free phase plate located at the selected area aperture plane [3,12] at at incident electron dose of 60 e^-/A^2 for both images *Sample courtesy Dr. Naoki Hosogi, JEOL Ltd.*). (b) An in-focus hole-free phase plate image of ebolavirus collected on an FEI Titan Krios equipped with a Gatan K2 direct electron detector. The thin spiderweb-like threads are RNA broken nucleoprotein-RNA helix and the curly structures are uncoiled NP-RNA complex. About 0.6 nm resolution has been obtained in the 3D reconstruction. The scale bar corresponds to 50 nm (right panel), and the color 3D visualization of the virus particle on the left is about 28 nm in diameter (*Image courtesy of Prof. Matthias Wolf, Okinawa Inst. for Science and Technology, Japan.*, see [285,286]). (c) Cryo hole-free phase plate image of 20S proteasome at various values of phase shift relative to q=0. Sub 0.3 nm resolution was demonstrated combining hole-free phase plate with single particle analysis methods and a small amount of defocus [134] (d) 4.2 nm thick slices extracted from a 3D tomographic reconstruction of a mitochondria at several magnifications. Arrows indicate F1 ATP synthase. The results were obtained using a zero-loss filtered hole-free phase plate tilt series collected using a K2 direct detection camera at 300 kV and a total dose 112 e^-/A^2. Scale bars: 500 nm in (a-left), 100 nm in (b-middle), 50 nm in (c-right) [131]

the use of HFPP does not appear to be detrimental to high resolution information transfer as compared to bright field transmission electron microscopy, and the object alignment can be improved by the transfer of low spatial frequencies. More recently, the focus in high resolution cryo-TEM imaging and structure investigation has shifted toward increasing the efficiency of high spatial frequencies information transfer. One avenue for improving such transfer utilizes an additional einzel lens as proposed by [198,256], based on the concept reported in [208]. It is possible that adding a time-variable bias to HFPP could have the same effect as, for example [198,256], while not blocking the beam with hardware that is not electron transparent. Simultaneous transfer of low spatial frequencies and high spatial frequencies should make it easier to align sub-images containing, for example, individual protein particles.

The most recent results indicate that atomic resolution of a protein structure is achievable, by reducing the high order aberration of the microscope imaging system and using either a cold field emission source or a monochromated Schottky electron source, corrected to high order aberrations of the imaging lens combined with a high quality direct electron detector but *without* a PP [206,207,257]. While the results mentioned above indicate that a HFPP does not have a detrimental effect on imaging at ≈0.2 nm resolution, the effect of HFPP at sub 0.2 nm imaging has not been reported at the time of writing.

Materials and physical sciences applications

The main advantages of HFPP compared to other approaches, see Table 3, are the ease of operation and the ability to transfer low ($q < 1\,\mathrm{nm}^{-1}$) spatial frequencies with minimal contrast ringing when correctly implemented [118]. Objects benefiting from the above advantages include long range magnetic and electric fields, layers inside semiconductor devices and increased visibility of very thin contamination layers. Practical samples include magnetic materials and associated imaging of fringing magnetic fields in a vacuum *outside* a sample. HFPP allows imaging of magnetic samples *in-focus* thus making it possible to observe *both* the magnetic field and the

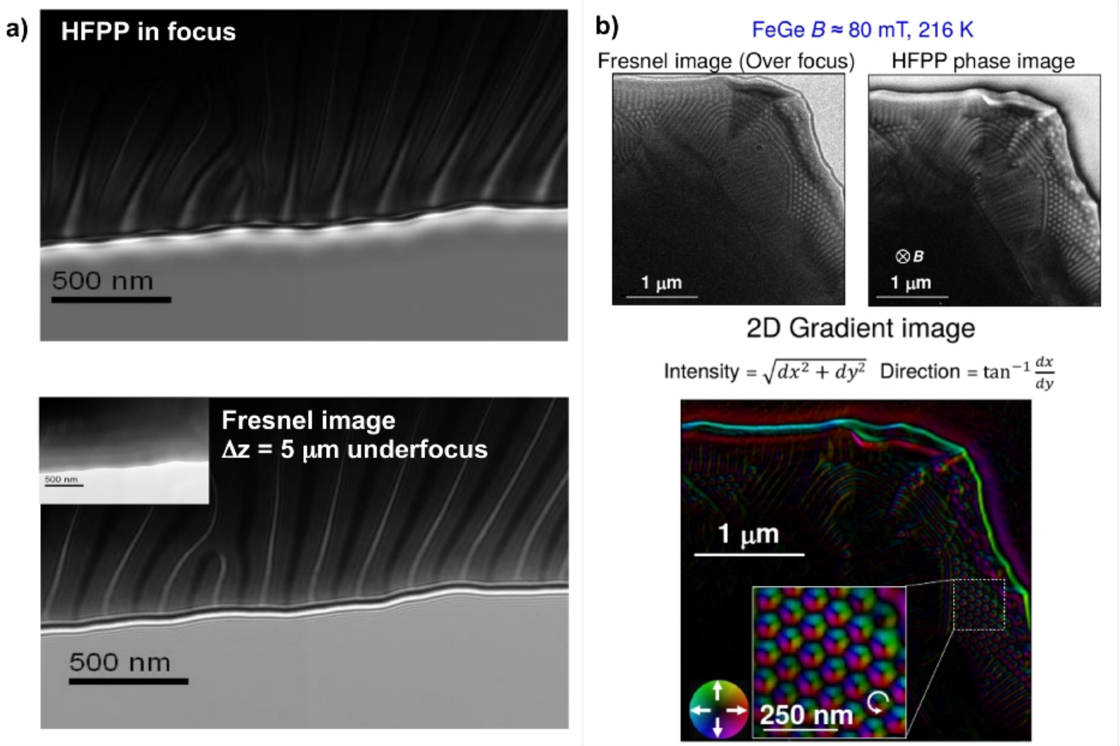

Fig. 17. Example applications of hole-free phase plate to imaging of magnetic materials. (a) hole-free phase plate image of a hard magnetic material obtained using a 10 nm thick carbon hole-free phase plate held at room temperature [258] in a JEOL 2100M with the sample outside the magnetic field of the objective lens [287]. (b) Images of magnetic skyrmion lattice imaged at 300 kV in a Hitachi HF-3300 at NRC-NANO with a home build hole-free phase plate placed at the selected area aperture plane. The imaging optics enabled imaging of the sample with the objective lens off [36].

sample microstructure of the same image at comparable, often sub 1 nm resolution. The sub 1 nm resolution is sufficient to image grains and defects of magnetic samples simultaneously with the magnetization of the sample at the same spatial resolution [258]. Since the HFPP images provide contrast without the need for off line processing, HFPP has the potential to image dynamic phenomena in magnetic samples.

Figure 17(a) shows an application of PP imaging to hard magnetic materials. It is also possibly the first time a magnetic sample was imaged using a PP TEM. The upper panel shows an *in-focus* HFPP image of a hard magnet (PrDyFeB) while the bottom panel shows a 5 µm underfocus image of the same area for comparison. The HFPP image shows not only the edge of the sample in-focus and therefore with only limited contrast delocalization, but also the magnetic field in the vacuum near the sample edge [258]. The experiment in [258] was compared to an image simulation achieving a qualitative agreement of the observed contrast and the anticipated properties of the sample. Fig. 17b is an example of a HFPP application to study skyrmion lattice in FeGe [36]. This weak phase object allowed *quantitative* linking of the measured HFPP contrast to magnetization within the sample, thus proving for the first time that HFPP can be a quantitative imaging tool (see Section 'Toward a quantitative interpretation'). More recently, the HFPP was used to study Sc-substituted M-type hexaferrite samples showing the coexistence of magnetic bubble and stripe domains [259].

In materials sciences, just as in biological sciences, many samples are either radiation sensitive or provide very weak contrast, or both. The weak contrast and radiation damage prevent the acquisition of the tilt series needed for tomographic reconstruction, and for alignment in the tilt series of images. The fact that HFPP offers sufficient stability for tilt series acquisition was shown in [136,260]. Fig. 18a illustrates applications of HFPP to organic electronics devices composed of carboneous organic molecules and carboneous contact layers with very little contrast observable in bright field transmission electron microscopy (left panel). In the HFPP image (right panel) the bromo-phenyl layer can be clearly observed [34]. In this case, the HFPP allowed not only visualization of the bromo-phenyl active layer in 3D, but also to evaluation the interface roughness of the bromo-phenyl layer buried in the device [261]. Fig. 18b shows the application of HFPP tomography to a 22 nm node computer processor chip [34]. The slice images from a 3D reconstructed volume with HFPP make it possible to visualize all layers within the device in 3D at a low irradiation dose, including the Si oxide layer between Si and poly-Si. The fact that a strongly diffracting crystalline sample can be imaged using a PP method may come as a surprise. However, because 60 images in 3° tilt increments comprise a tilt series means that only a small fraction of the images are collected near strongly diffracting conditions and their effect on the reconstructed volume is not critical [34]. ZPP was also successfully used to image block copolymers [262] as was HFPP [263].

Figure 19 shows imaging of contamination on graphene. The HFPP image makes it possible to detect a thin contamination layer on graphene that is difficult to achieve using energy filtering bright field transmission electron microscopy and log-ratio thickness mapping in EELS [121]. Combining the HFPP and log-ratio mapping using energy-filtering images may improve the detection limit. These log-ratio EELS thickness measurements obtained using energy filtered HFPP images retain the possibility for quantitative and absolute

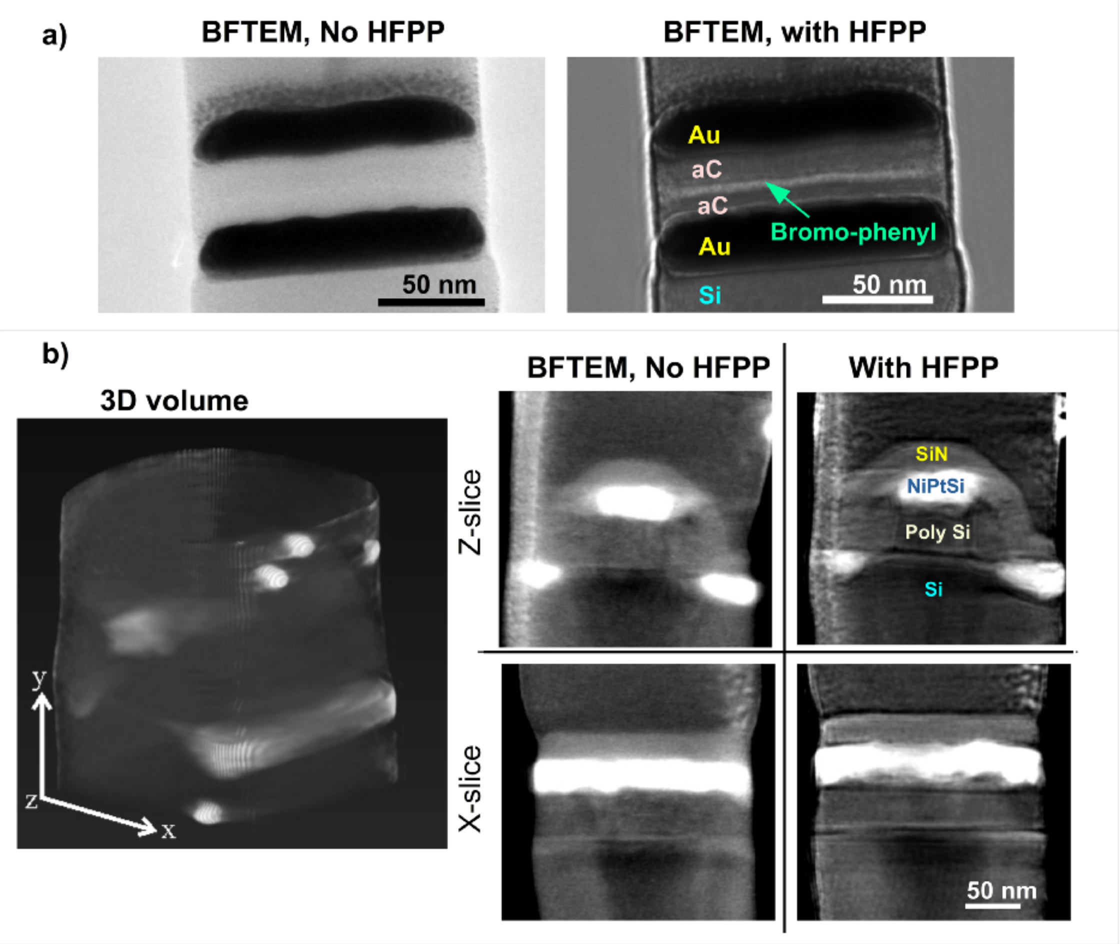

Fig. 18. Rod-shaped samples for hole-free phase plate electron tomography in materials science. (a) Bright field transmission electron microscope images of molecular electronics device with and without hole-free phase plate. (b) A 3D reconstructed volume of a 22 nm node computer processor chip from a tilt series of images acquired with a hole-free phase plate in a JEOL 2200 FS. The slice images are from the 3D reconstructed volumes with and without hole-free phase plate. [34] and [288]. The phase plate was heated to about 250 °C and was placed in an objective area aperture, unlike the earlier experiments in the same microscope where the hole-free phase plate was placed in a selected area aperture [3]. A tilt series of the same area was also acquired without hole-free phase plate.

thickness measurements. It is, however, necessary to subtract the thickness of the HFPP film from the total measured thickness. This can be easily done by taking a reference thickness map where the HFPP is present in the beam while the sample is removed from the beam path. We note that the t/λ for the HFPP film has to be evaluated using the collection angle applicable to an object at the HFPP plane (e.g. BFP). Typically, the collection angle at the HFPP plane is much smaller than that of an object placed in the sample plane and can be measured by observing the diffraction pattern from a film placed at the HFPP plane.

Toward a quantitative interpretation

In this section, we look at the progress made toward *quantitative* imaging using (hole-free) phase plates ((HF)PPs). In this context, *quantitative* refers to obtaining the sample phase (and amplitude) distribution. This can be done by single images, assuming the presence of pure phase contrast, or by the acquisition of several complementary images to reconstruct the object exit wave, comparable to EH. The first approach is discussed in Section 'Quantitative interpretation of single phase plate images,' while methods for object-wave reconstruction based on PPs are briefly presented in Section 'Object-wave reconstruction using phase plates'. Once obtained, the sample-induced phase shift or the complete object exit wave, can serve to determine sample properties such as magnetization, local thickness or chemical composition.

Quantitative interpretation of single PP images

An imaging method that enables a quantitative link to the object phase, that is easy to implement and provide a wide field of view, could have an enormous impact on electron microscopy in both materials science and biological sciences. However, the phase resolution and traceability of HFPP does not compare favorably with interferometric methods, such as EH [264,265]. In EH, the phase shift difference between sample and reference waves takes place in real space making it possible to locate the interfering wavefronts and

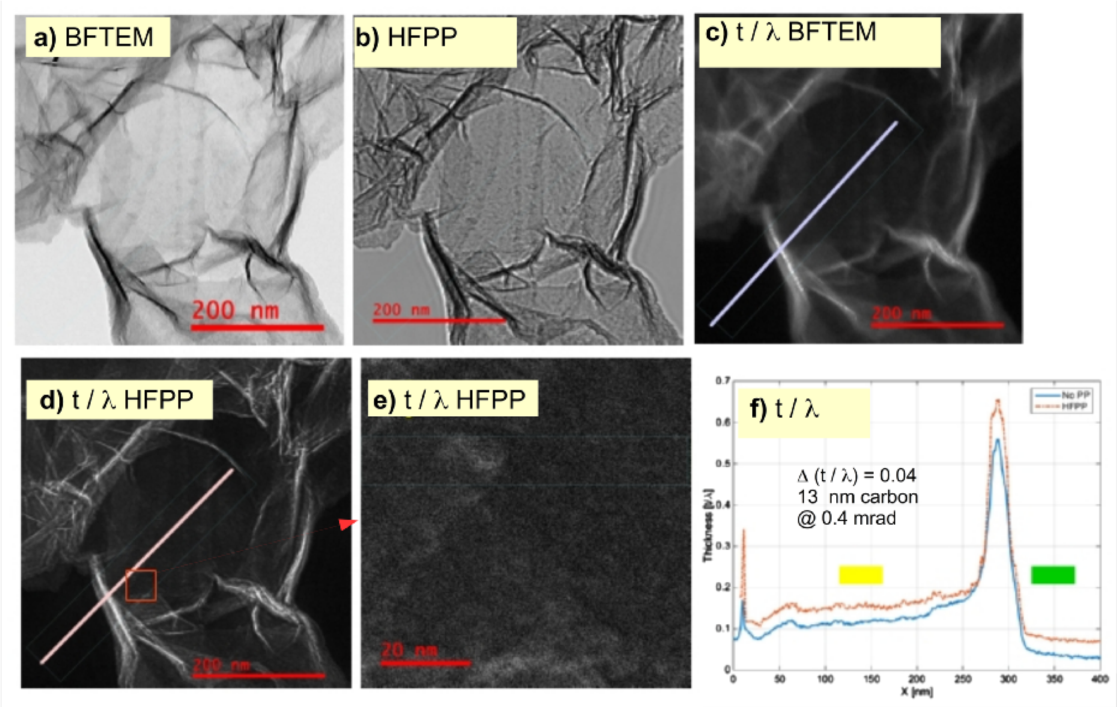

Fig. 19. Hole-free phase plate imaging of contamination on graphene [289] (a) indicates that adding hole-free phase plate while performing a log ratio electron energy loss spectroscopy thickness measurement increases the apparent image contrast, but does not affect relative thickness measurements. The addition of hole-free phase plate only adds the thickness of the hole-free phase plate film to the sample thickness measured by the electron energy loss spectroscopy log-ratio method [121]. The electron energy loss spectroscopy collection angle for a hole-free phase plate at the back focal plane may be very small resulting in a very long inelastic mean free path [121]. a) Shows a bright field transmission electron microscope image of a heavily contaminated graphene film; (b) shows a hole-free phase plate image of the same sample area; (c) is a thickness map obtained by the electron energy loss spectroscopy log-ratio method using bright field transmission electron microscope images; (d) is an electron energy loss spectroscopy log-ratio mass thickness map obtained using hole-free phase plate images with the area marked by the red square shown in (e); (f) is an electron energy loss spectroscopy log-ration thickness map profile, indicated in (c) and (d), obtained from bright field transmission electron microscope and hole-free phase plate images. The upper (orange) profile is from the hole-free phase plate images and the lower (blue) profile is from the bright field transmission electron microscope images. The hole-free phase plate was kept in the beam for both zero-loss filtered and unfiltered images for the hole-free phase plate electron energy loss spectroscopy log-ratio thickness map. Fig. 19a–f was obtained in a JEOL 2200 FS at NRC-NANO with an Ω in-column energy filter operated at 200 kV and a commercial graphene sample held at room temperature without sample cleaning prior to the experiment.

their relation to the sample. In HFPP, it is interference in the reciprocal (Fourier) space where the direct and diffracted beam can originate from any location of the sample or nearby vacuum.

Under ideal conditions that is, no aberrations and an ideal phase shift distribution, the image contrast is directly proportional to the sample-induced phase shift of WPOs (Eq. (28)). However, imaging conditions and the phase shift distribution of the PP cannot be assumed to be ideal. Nevertheless, a first approximation is that the contrast in an in-focus PP image is a pure phase contrast. Based on this assumption, it is possible to extract semi-quantitative phase information from the sample. For a full quantitative link, image simulations considering the phase-shift distribution are necessary.

An initial study on magnetic sample imaging [258] reported a qualitative or perhaps semi-quantitative match of the image intensity profiles with simulations. The simulations were rather simplistic and did not include magnetization direction changes close to the edge of the sample. Nevertheless, the experimental image intensity profile corresponded well with the simulation results.

A major step toward a quantitative interpretation of HFPP images was reported by Kotani *et al.* [36]. The authors assumed a WPO, i.e. the sample phase shift is smaller than the phase shift induced by the PP, and an ideal PP phase shift distribution resulting in a linear relation between the image contrast and the sample-induced phase shift (Eq. (28)). This relation was then used to extract the sample phase shift distribution and to calculate the magnetization map in a FeGe skyrmion sample.

In a more recent report, the authors demonstrate that it is possible to extract both the phase shift of the direct and diffracted beams of a strong phase object as well as the phase shift induced on them by the PP [37]. Using a specifically structured sample, the direct and diffracted beams are well separated at the HFPP plane. Besides obtaining a quantitative link between the image contrast and the sample and PP phase shift, the work gives insights into the phase shift evolution of the HFPP with irradiation dose, its stability and the effect of the phase shift difference among diffracted beams.

When attempting a fully quantitative interpretation of HFPP images, it is necessary to perform simulations considering the *shape* of the phase shift profile or at least to consider whether assuming a step-like or δ function-like profile of the HFPP acting only at the direct beam $q = 0$ is adequate for a quantitative interpretation of a particular sample. Strictly speaking, the δ function-like phase shift profile applies only for well separated discrete direct and diffracted beams, as reported in [37].

Object-wave reconstruction using PPs

The ultimate information obtainable from a sample by transmission electron microscopy images is the spatial distribution of amplitude and phase in the object wave. Several holographic formulations exist to reconstruct the object exit wave, including off-axis and inline EH [264–271]. We refer to the literature on details, drawbacks and advantages on these techniques and will only briefly introduce the reconstruction methods using PPs.

Nagayama proposed reconstruction of the object phase and amplitude via a 'complex observation' scheme, involving the acquisition of three images: a bright field transmission electron microscopy image, a PP image and a dark-field image obtained by blocking the direct beam only [272]. This complex observation was applied using the Zernike [273] and the Hilbert PP in a variant of the scheme [52]. With the availability of PPs with tunable phase shifts, reconstruction is possible using three phase-contrast images acquired at different phase shifts [42,274] and was realized using the Zach PP [28,275–280]. A reconstruction scheme considering non-linear image formation based on Zernike or Hilbert PPs was developed that allows for correction of damping in the thin film [56].

In practical applications, all of the PP reconstruction schemes rise and fall with the PP performance, so both the drawbacks and advantages of the PPs have to be considered (Table 3). The closer the phase shift distribution is to the ideal case, the better will be the results of the reconstruction. Although some effects may be corrected or recuperated using additionally acquired images, the technique that is closest to being perfect will yield the best results, be the easiest to use and thus will have the biggest impact. In general, PPs that allow a fast control of the applied phase shift (e.g. electrostatic PPs) are advantageous for the reconstruction procedure as the acquisition of the necessary images can be performed much faster posing fewer demands on microscope and PP stability. Although not ideally suited, HFPPs might also serve to reconstruct the complete object wave by the acquisition of several images during the build-up of the phase shift.

Summary and outlook

Significant progress has been made in PP imaging in TEMs over the past decade. This progress was largely enabled by the progress in microfabrication of devices and thin films. Initially, thin film type ZPPs suitable for practical applications were demonstrated by Prof. Nagayama's team. The progress on thin film type ZPPs motivated the rapid development of Börsch and Zach PPs.

Arguably, the invention of HFPPs (sometimes referred to as 'Volta PPs') led to a widespread use of PP technology. The proliferation of the HFPP appears to be driven primarily by its convenient implementation and operation and its provision of a qualitative increase in image contrast. The development of applications of PP imaging, including the HFPP, is in its early stages. Significant effort has been dedicated toward improving the resolution limit of single particle analysis in structural biology by improving the DLR.

A HFPP can also improve the alignment accuracy by virtue of increased contrast at low spatial frequencies.[19]

The most significant impact of PP imaging might result from the imaging of signals impossible or difficult to image by other means. For example, the opportunity arises to image magnetic and electric fields in-focus while eliminating sample staining in histology, and visualizing the internal morphology of samples with minuscule difference in MIP. Furthermore, contrast enhancement together with adequate stability, reproducibility and repeatability could be utilized for electron tomography of extremely low contrast materials, e.g. organic electronics devices.

It is possible that (hole-free) PP imaging can eventually become a quantitative method, in the sense that it could become routinely possible to quantitatively link the measured image contrast to the sample properties, such as the sample's electric and magnetic fields. The feasibility of quantitative interpretation has already been demonstrated in a few specific circumstances. However, it is unlikely that PP imaging can approach the phase measurement accuracy and spatial resolution of interferometric methods, such as EH.

On the conceptually straightforward side, it is hard to imagine a method that is simpler and more convenient than the hole-free (Volta) PP. The ability to observe the time evolution of a sample and utilize the time evolution of the PP during its settling period could offer new opportunities.

On the conceptually complicated and technically challenging side is laser phase-plate imaging, led by Glaeser. The laser PP is appealing as it does not include hardware that blocks the electron beam, nor does it reduce counts due to inelastic scattering in the PP film. Providing that technical challenges can be resolved, the laser PP could be an important development; these challenges include the stability of a high power laser field in a resonance cavity and automated alignment, e.g. its alignment with the laser field nodes, the shape of the phase profile arising from the laser field, etc. The laser PP is unlikely to be retrofitable to existing microscopes, requiring instead a dedicated column design.

PPs requiring beam-obscuring hardware and bright-field TEM-like transfer of low spatial frequencies, such as the Börsch PP, can be rather complicated to align and operate. Their niche maybe in applications where control and modulation of the PP phase shift is needed e.g. to quantitatively measure the sample phase shift. In this context, the Zach PP appears to suffer the least from beam blocking and alignment difficulties while providing convenient phase shift control.[20]

Methods that are either complementary or a direct replacement for PP imaging include EH, differential phase contrast in STEM, Lorentz and Foucault imaging in TEM. Each of these could provide

---

[19] Directions currently pursued to improve the resolution in (protein) structure determination by cryo electron microscopy include improved spherical aberration correctors (B-CORR) [206], high brightness cold field emission electron sources or a Schottky electron source with a monochromator and fast, high quantum efficiency detectors [207,257,281,282]. Focus modulation can improve the image interpretability at high spatial frequencies [198,208].

[20] The detrimental effect of spurious device charging can perhaps be reduced by holding the device at an elevated temperature. For carbon film-based devices, the lowest temperature that allows for operation without spurious charging is $\approx 350^\circ$C. It is possible that heating above $\approx 350^\circ$C would also apply for Zach and Börsch PPs, if they are covered by thin carbon film.

advantages over PP imaging. For example, a PP is unlikely to be able to measure an atomic scale phase shift as is done by EH and differential phase contrast. But at the same time PP imaging can easily image slowly varying long range electric and magnetic fields, including fields in a vacuum outside the sample, a task difficult for other methods. As mentioned above, PP imaging is unlikely to increase the electron-optical resolution. But the effective, DLR is increased by a (hole-free) PP. A (hole-free) PP can be advantageous when imaging a small number or individual protein or virus particles at modest (≈ 1 nm) resolutions. This arises from the fact that the transfer of low spatial frequencies (below (≈ 1 nm)) reduces the irradiation dose needed to detect an object, e.g. a virus or a protein particle.

As seen throughout this manuscript, the simple solution afforded by the HFPP makes it amenable to wide acceptance by the research community. More complicated schemes do have their niche, although the potential reward in terms of access to new signals has to be weighed against the experimental difficulties involved.

A possible direction that has not been explored is to operate the HFPP at cryo temperature as the PP film does not contaminate at low temperatures [137]. A HFPP operated at cryo temperature could improve the stability of imaging and reduce the sample heat load from a traditional, heated HFPP.

At present, it appears that the niche for PP imaging of biological samples could be modest-resolution imaging of objects that are located only infrequently in a sample, i.e. objects where single particle averaging analysis methods cannot be used due to low availability of the particles, or because variations between individuals or small groups of individuals need to be made.

Acknowledgement

Our extensive thanks belong to Dr. Masahiro Kawasaki, who has been one of the main forces driving the development of hole-free phase plate. The team at JEOL Ltd., Dr. Yoshi Okura, Dr. Shohei Motoki, Dr. Isamu Ishikawa, Dr. Yuji Konyuba and Dr. Naoki Hosogi, made the development of phase plate at NRC-NANO possible. Their ongoing support, kind advice and involvement in instrument development and modifications were critical for our work on hole-free phase plate at NRC-NANO. Brian Legge from JEOL Canada solved our often self inflicted technical challenges from the early days of our phase plate imaging. Dr. Hiromitsu Furukawa and Miyoko Shimizu of Systems In Frontier Inc. were crucial for the first demonstration of stability and suitability of early generation of hole-free phase plate for electron tomography. The progress toward quantitative imaging using hole-free phase plate has been motivated and often driven by Dr. Ken Harada (RIKEN), Dr.Atsuhiro Kotani and Dr. Shigeo Mori (Osaka Prefecture University). Dr. Yoshifumi Taniguchi from Hitachi High Technologies Corp. (HHT) helped us to implement measurement of SE emission, EELS and transfer function evolution in the Hitachi HF-3300 at NRC-NANO. Dr. Toshie Yaguchi and Dr. Takashi Fujii of HHT continue to support our efforts in advancing various aspects of electron microscopy at NRC-NANO. Our thanks to Dr. Kai Cui and Dr. Jian Chen for their support of the Hitachi HF-3300 and JEOL 2200 FS laboratories at NRC-NANO. We are grateful to Dr. Matthias Wolf and Dr. Cathal Cassidy (Okinawa Institute for Science and Technology, Japan) for motivating discussion on the biological and materials science applications of HFPP. S.H. acknowledges funding by the Deutsche Forschungsgemeinschaft (HE 7675/1-1)

Funding

Primary source of funding for this work was NRC-NANO research centre of National Research Council, Canada.

References

1. Malac M, Beleggia M, Kawasaki M, Li P, and Egerton R (2012) Convenient contrast enhancement by a hole-free phase plate. *Ultramicroscopy* 118: 77–89.
2. Malac M, Beleggia M, Kawasaki M, and Egerton R (2014) Charging of hole-free thin film phase plate. US patent 8,785,850.
3. Malac M, Kawasaki M, Beleggia M, Li P, and Egerton R (2010) Convenient contrast enhancement by hole free phase plate in a TEM. *Microsc. Microanal.* 16: 527–527.
4. Danev R, Buijsse B, Khoshouei M, Plitzko J, and Baumeister W (2014) Volta potential phase plate for in-focus phase contrast transmission electron microscopy. *PNAS* 111: 15635–15640.
5. Glaeser R M (2019) How good can single-particle cryo-em become? what remains before it approaches its physical limits?. *Annu. Rev. Biophys.* 48: 45–61.
6. Danev R, Glaeser R, and Buijsse B (2012) Properties and behavior of amorphous carbon films related to phase plate applications. *Microsc. Microanal.* 18: 482–483.
7. Marko M, and Hsieh C (2015) Initial experience with the Volta phase plate. *Microsc. Microanal.* 21: 1579–1580.
8. Malac M, Beleggia M, Egerton R, and Zhu Y (2008) Imaging of radiation-sensitive samples in transmission electron microscopes equipped with Zernike phase plates. *Ultramicrosc.* 108: 126–140.
9. Nagayama K, and Danev R (2009) Phase-plate electron microscopy: a novel imaging tool to reveal close-to-life nano-structures. *Biophys. Rev.* 1: 37–42.
10. Zernike F (1942) Phase contrast, a new method for the microscopic observation of transparent objects. *Physica* 9: 686–698.
11. Boersch H (1947) Uber die kontraste von atomen im elektronenmikroskop. *Z. Naturforsch.* 2a: 615–633.
12. Kawasaki M, Malac M, Li P, Qian H, and Egerton R (2009) Convenient electron optics set up for Zernike phase microscopy in TEM. *Microsc. Microanal.* 15: 1234–1235.
13. Kanaya K, Kawakatsu H, Itō K, and Yotsumoto H (1958) Experiment on the electron phase microscope. *J. Appl. Phys.* 29: 1046–1049.
14. Badde H G, and Reimer L (1970) Der einfluss einer streuenden phasenplatte auf das elektronenmikroskopische bild. *Z. Naturforsch.* 25a: 760–765.
15. Parsons D, and Johnson H (1972) Possibility of a phase contrast electron microscope. *Appl. Opt.* 11: 2840–2843.
16. Unwin P N T (1971) Phase contrast and interference microscopy with the electron microscope. *Philos. Trans. R. Soc. Lond. B, Biol. Sci.* 261: 95–104.
17. Matsumoto T, and Tonomura A (1996) The phase constancy of electron waves traveling through Boersch's electrostatic phase plate. *Ultramicroscopy* 63: 5–10.
18. Nagayama K (2011) Another 60 years in electron microscopy: development of phase-plate electron microscopy and biological applications. *J. Electron Microsc.* 60: S43–S62.
19. Danev R, and Nagayama K (2001) Transmission electron microscopy with Zernike phase plate. *Ultramicroscopy* 88: 243–252.
20. Schultheiss K, Pérez-Willard F, Barton B, Gerthsen D, and Schroeder R R (2006) Fabrication of a Boersch phase plate for phase contrast imaging in a transmission electron microscope. *Rev. Sci. Instrum.* 77: 033701.
21. Majorovits E, Barton B, Schultheiß K, Pérez-Willard F, Gerthsen D, and Schröder R (2007) Optimizing phase contrast in transmission electron microscopy with an electrostatic (Boersch) phase plate. *Ultramicroscopy* 107: 213–226.
22. Majorovits E, and Schröder R (2002) Improved information recovery in phase contrast em for non-two-fold symmetric Boersch phase plate geometry. *Microsc. Microanal.* 8: 540–541.
23. Gerthsen D, Schultheis K, Barton B, and Schröder R (2007) Effect of a physical phase plate on contrast transfer in an aberration-corrected transmission electron microscope. *Microsc. Microanal.* 13: 126–127.

24. Hsieh W, Anderson E, Benner G, Park M, Gomez E, Balsara N, and Kisielowski C (2007) Contrast transfer function design by an electrostatic phase plate. *Microsc. Microanal.* 13: 1216–1217.
25. Majorovits E, Barton B, Benner G, Dietl C, Kuhlbrandt W, Lengweiler S, Mandler T, Matijevic M, Niebel H, and Schroder R (2010) Phase contrast aberration corrected electron microscope for phase plate imaging. *Microsc. Microanal.* 16: 534–535.
26. Walter A, Barton B, Rhinow D, and Kühlbrandt W (2011) Towards in-focus phase-contrast electron cryo-microscopy. *Microsc. Microanal.* 17: 974–975.
27. Cambie R, Downing K H, Typke D, Glaeser R M, and Jin J (2007) Design of a microfabricated, two-electrode phase-contrast element suitable for electron microscopy. *Ultramicroscopy* 107: 329–339.
28. Schultheiss K, Zach J, Gamm B, Dries M, Frindt N, Schröder R R, and Gerthsen D (2010) New electrostatic phase plate for phase-contrast transmission electron microscopy and its application for wave-function reconstruction. *Microsc. Microanal.* 16: 785–794.
29. Schröder R, Barton B, Rose H, and Benner G (2007) Contrast enhancement by anamorphotic phase plates in an aberration corrected TEM. *Microsc. Microanal.* 13: 8–9.
30. Müller H, Jin J, Danev R, Spence J, Padmore H, and Glaeser R M (2010) Design of an electron microscope phase plate using a focused continuous-wave laser. *New J. Phys.* 12: 073011.
31. Edgcombe C J, Ionescu A, Loudon J C, Blackburn A M, Kurebayashi H, and Barnes C (2012) Characterisation of ferromagnetic rings for Zernike phase plates using the Aharonov–Bohm effect. *Ultramicrosc.* 120: 78–85.
32. Schwartz O, Axelrod J J, Campbell S L, Turnbaugh C, Glaeser R M, and Müller H (2019) Laser phase plate for transmission electron microscopy. *Nat. Methods* 16: 1016–1020.
33. Malac M, Beleggia M, Egerton R, and Zhu Y (2007) Bright-field TEM imaging of single molecules: dream or near future?. *Ultramicroscopy* 107: 40–49.
34. Hayashida M, Cui K, Najarian A M, McCreery R, Jehanathan N, Pawlowicz C, Motoki S, Kawasaki M, Konyuba Y, and Malac M (2019) Hole free phase plate tomography for materials sciences samples. *Micron* 116: 54–60.
35. Malac M, Bergen M, Egerton R, Kawasaki M, Beleggia M, Furukawa H, and Shimizu M (2012) Practical hole-free phase plate imaging: principles, advantages and pitfalls. *Microsc. Microanal.* 18: 484–485.
36. Kotani A, Harada K, Malac M, Salomons M, Hayashida M, and Mori S (2018) Observation of fege skyrmions by electron phase microscopy with hole-free phase plate. *AIP Adv.* 8: 055216.
37. Harada K, Malac M, Hayashida M, Niitsu K, Shimada K, Homeniuk D, and Beleggia M (2020) Toward the quantitative the interpretation of hole-free phase plate images in a transmission electron microscope. *Ultramicroscopy* 209: 112875.
38. Malac M, Hettler S, Hayashida M, Kawasaki M, Konyuba Y, Okura Y, Iijima H, Ishikawa I, and Beleggia M (2017) Computer simulations analysis for determining the polarity of charge generated by high energy electron irradiation of a thin film. *Micron* 100: 10–22.
39. Kohl H, and Reimer L (2008) *Transmission electron microscopy: physics of image formation*, (Springer).
40. Hettler S, Wagner J, Dries M, Oster M, Wacker C, Schröder R R, and Gerthsen D (2015) On the role of inelastic scattering in phase-plate transmission electron microscopy. *Ultramicroscopy* 155: 27–41.
41. Beleggia M (2008) A formula for the image intensity of phase objects in Zernike mode. *Ultramicroscopy* 108: 953–958.
42. Gamm B, Dries M, Schultheiss K, Blank H, Rosenauer A, Schröder R, and Gerthsen D (2010) Object wave reconstruction by phase-plate transmission electron microscopy. *Ultramicroscopy* 110: 807–814.
43. Danev R, Glaeser R M, and Nagayama K (2009) Practical factors affecting the performance of a thin-film phase plate for transmission electron microscopy. *Ultramicroscopy* 109: 312–325.
44. Danev R, and Nagayama K (2011) Optimizing the phase shift and the cut-on periodicity of phase plates for TEM. *Ultramicroscopy* 111: 1305–1315.
45. Murata K, Liu X, Danev R, Jakana J, Schmid M F, King J, Nagayama K, and Chiu W (2010) Zernike phase contrast cryo-electron microscopy and tomography for structure determination at nanometer and subnanometer resolutions. *Structure* 18: 903–912.
46. Chang W-H, Chiu M T-K, Chen C-Y, Yen C-F, Lin Y-C, Weng Y-P, Chang J-C, Wu Y-M, Cheng H, Fu J, and Tu I-P (2010) Zernike phase plate cryoelectron microscopy facilitates single particle analysis of unstained asymmetric protein complexes. *Structure* 18: 17–27.
47. Dai W, Fu C, Khant H A, Ludtke S J, Schmid M F, and Chiu W (2014) Zernike phase-contrast electron cryotomography applied to marine cyanobacteria infected with cyanophages. *Nat. Protoc.* 9: 2630–2642.
48. Rochat R H, Liu X, Murata K, Nagayama K, Rixon F J, and Chiu W (2011) Seeing the portal in herpes simplex virus type 1 b capsids. *J. Virol.* 85: 1871–1874.
49. Rhinow D (2016) Towards an optimum design for thin film phase plates. *Ultramicroscopy* 160: 1–6.
50. Marko M, Meng X, Hsieh C, Roussie J, and Striemer C (2013) Methods for testing Zernike phase plate and a report on silicon-based phase plates with reduced charging and improved ageing characteristics. *J. Struct. Biol.* 184: 237–244.
51. Danev R, Okawara H, Usuda N, Kametani K, and Nagayama K (2002) A novel phase-contrast transmission electron microscopy producing high-contrast topographic images of weak objects. *J. Biol. Phys.* 28: 627–635.
52. Danev R, and Nagayama K (2004) Complex observation in electron microscopy: Iv. reconstruction of complex object wave from conventional and half plane phase plate image pair. *J. Phys. Soc. Jpn.* 73: 2718–2724.
53. Kaneko Y, Danev R, Nitta K, and Nagayama K (2005) In vivo subcellular ultrastructures recognized with Hilbert differential contrast transmission electron microscopy. *J. Electron Microsc.* 54: 79–84.
54. Kaneko Y, Danev R, Nagayama K, and Nakamoto H (2006) Intact carboxysomes in a cyanobacterial cell visualized by hilbert differential contrast transmission electron microscopy. *J. Bacteriol.* 188: 805–808.
55. Barton B, Joos F, and Schröder R R (2008) Improved specimen reconstruction by Hilbert phase contrast tomography. *J. Struct. Biol.* 164: 210–220.
56. Dries M, Schultheiss K, Gamm B, Rosenauer A, Schröder R R, and Gerthsen D (2011) Object-wave reconstruction by carbon film-based Zernike- and Hilbert-phase plate microscopy: a theoretical study not restricted to weak-phase objects. *Ultramicroscopy* 111: 159–168.
57. Dries M, Hettler S, Gamm B, Müller E, Send W, Müller K, Rosenauer A, and Gerthsen D (2014) A nanocrystalline Hilbert phase-plate for phase-contrast transmission electron microscopy. *Ultramicroscopy* 139: 29–37.
58. Dries M, Hettler S, Schulze T, Send W, Müller E, Schneider R, Gerthsen D, Luo Y, and Samwer K (2016) Thin-film phase plates for transmission electron microscopy fabricated from metallic glasses. Microsc. Microanal. Off. J. Microsc. Soc. Am. (Microbeam Analysis Society, Microscopical Society of Canada) 22: 955–963.
59. Koeck P J (2015) Improved Hilbert phase contrast for transmission electron microscopy. *Ultramicroscopy* 154: 37–41.
60. Edgcombe C J (2017) Imaging with straight-edge phase plates in the TEM. *Ultramicroscopy* 182: 124–130.
61. Chen K-F, Chang C-S, Shiue J, Hwu Y, Chang W-H, Kai J-J, and Chen F-R (2008) Study of mean absorptive potential using lenz model: toward quantification of phase contrast from an electrostatic phase plate. *Micron* 39: 749–756.
62. Alloyeau D, Hsieh W, Anderson E, Hilken L, Benner G, Meng X, Chen F, and Kisielowski C (2010) Imaging of soft and hard materials using a Boersch phase plate in a transmission electron microscope. *Ultramicroscopy* 110: 563–570.

63. Barton B, Rhinow D, Walter A, Schröder R, Benner G, Majorovits E, Matijevic M, Niebel H, Muller H, Haider M, Lacher M, Schmitz S, Holik P, and Kuhlbrandt W (2011) In-focus electron microscopy of frozen-hydrated biological samples with a Boersch phase plate. *Ultramicroscopy* 111: 1696–1705.
64. Tamaki H, Kasai H, Harada K, Takahashi Y, and Nishi R (2013) Development of a contact-potential-type phase plate. *Microsc. Microanal.* 19: 1148–1149.
65. Zach J (2011) Phase plate, imaging method, and electron microscope. note US Patent 7,928,379.
66. Hettler S, Gamm B, Dries M, Frindt N, Schröder R R, and Gerthsen D (2012) Improving fabrication and application of Zach phase plates for phase-contrast transmission electron microscopy. *Microsc. Microanal.* 18: 1010–1015.
67. Frindt N, Oster M, Hettler S, Gamm B, Dieterle L, Kowalsky W, Gerthsen D, and Schröder R R (2014) In-focus electrostatic Zach phase plate imaging for transmission electron microscopy with tunable phase contrast of frozen hydrated biological samples. *Microsc. Microanal.* 20: 175–183.
68. Hettler S, Dries M, Zeelen J, Oster M, Schröder R R, and Gerthsen D (2016) High-resolution transmission electron microscopy with an electrostatic Zach phase plate. *New J. Phys.* 18: 053005.
69. Obermair M, Marko M, Hettler S, Hsieh C, and Gerthsen D (2018) Physical phase plates for cryo-electron microscopy of biological specimens: comparison of hole-free phase plates and Zach electrostatic phase plates. *Microsc. Microanal.* 24: 892–893.
70. Frindt N, Gamm B, Dries M, Schultheis K, Gerthsen D, and Schröder R (2009) Simulating Hilbert phase contrast produced by an anamorphotic electrostatic phase plate. In: *MC 2009. Microscopy Conference*, p 61.
71. Rose H (2010) Design of an obstruction-free phase-shifter yielding maximum contrast over a large range of spatial frequencies. *Microsc. Microanal.* 16: 548–549.
72. Frindt N, Schultheiss K, Gamm B, Dries M, Zach J, Gerthsen D, and Schröder R (2010) The way to an ideal matter-free Zernike and Hilbert TEM phase plate: anamorphotic design and first experimental verification in isotropic optics. *Microsc. Microanal.* 16: 518–519.
73. Koeck P J (2019) Design of a charged particle beam phase plate for transmission electron microscopy. *Ultramicroscopy* 205: 62–69.
74. Hettler S, Dries M, Hermann P, Obermair M, Gerthsen D, and Malac M (2017) Carbon contamination in scanning transmission electron microscopy and its impact on phase-plate applications. *Micron* 96: 38–47.
75. Tavabi A H, Beleggia M, Migunov V, Savenko A, Öktem O, Dunin-Borkowski R E, and Pozzi G (2018) Tunable ampere phase plate for low dose imaging of biomolecular complexes. *Sci. Rep.* 8: 1–5.
76. Buijsse B, van Laarhoven F M, Schmid A K, Cambie R, Cabrini S, Jin J, and Glaeser R M (2011) Design of a hybrid double-sideband/single-sideband (schlieren) objective aperture suitable for electron microscopy. *Ultramicroscopy* 111: 1688–1695.
77. Glaeser R M, Sassolini S, Cambie R, Jin J, Cabrini S, Schmid A K, Danev R, Buijsse B, Csencsits R, Downing K H, Larson D M, Typke D, and Han B (2013) Minimizing electrostatic charging of an aperture used to produce in-focus phase contrast in the TEM. *Ultramicroscopy* 135: 6–15.
78. Cullis A G, and Maher D M (1975) Topographical contrast in the transmission electron microscope. *Ultramicroscopy* 1: 97–112.
79. Koeck P J B (2017) An aperture design for single side band imaging in the transmission electron microscope. *Ultramicroscopy* 182: 81–84.
80. Minoda H, Okabe T, and Iijima H (2011) Contrast enhancement in the phase plate transmission electron microscopy using an objective lens with a long focal length. *J. Electron Microsc.* 60: 337–343.
81. Hosokawa F, Danev R, Arai Y, and Nagayama K (2005) Transfer doublet and an elaborated phase plate holder for 120 kv electron-phase microscope. *J. Electron Microsc.* 54: 317–324.
82. Motoki S, Hosokawa F, Arai Y, Danev R, and Nagayama K (2005) 200 Kv TEM with a Zernike phase plate. *Microsc. Microanal.* 11: 708–709.
83. Majorovits E, Nagayama K, and Schroder R R (2002) Enhancing contrast of weak phase objects using a Zernike-type phase plate in phase contrast TEM. *Microsc. Microanal.* 8: 864–865.
84. Inayoshi Y, Minoda H, Arai Y, and Nagayama K (2012) Direct observation of biological molecules in liquid by environmental phase-plate transmission electron microscopy. *Micron* 43: 1091–1098.
85. Fukuda Y, Fukazawa Y, Danev R, Shigemoto R, and Nagayama K (2009) Tuning of the Zernike phase-plate for visualization of detailed ultrastructure in complex biological specimens. *J. Struct. Biol.* 168: 476–484.
86. Koeck P J B (2015) Improved Zernike-type phase contrast for transmission electron microscopy. *J. Microsc.* 259: 74–78.
87. Iijima H, Motoki S, Hosokawa F, and Ohkura Y (2012) Aberration corrected Zernike phase contrast TEM. *Microsc. Microanal.* 18: 492–493.
88. Typke D, Glaeser R, Downing K, Tiemeijer P, Cambie R, and Jin J (2008) Aspects of using a Boersch type phase shifting device for contrast enhancement in macromolecular electron microscopy. *Microsc. Microanal.* 14: 74–75.
89. Kishchenko G P, Danev R, Fisher R, He J, Hsieh C, Marko M, and Sui H (2015) Effect of fringe-artifact correction on sub-tomogram averaging from Zernike phase-plate cryo-TEM. *J. Struct. Biol.* 191: 299–305.
90. Kurth P, Pattai S, Rudolph D, Overbuschmann J, Wamser J, and Irsen S (2014) Artifact-free, long-lasting phase plate. *Microsc. Microanal.* 20: 220–221.
91. Barton B, Joos F, and Schröder R R (2008) Improved specimen reconstruction by Hilbert phase contrast tomography. *J. Struct. Biol.* 164: 210–220.
92. Dries M, Gamm B, Hettler S, Müller E, Send W, Gerthsen D, and Rosenauer A (2012) A nanocrystalline Hilbert-phase plate for phase-contrast transmission electron microscopy of amorphous objects. *Microsc. Microanal.* 12: 496–497.
93. Dries M, Hettler S, Gamm B, Müller E, Send W, Gerthsen D, Müller K, and Rosenauer A (2014) A nanocrystalline Hilbert phase-plate for phase-contrast transmission electron microscopy. *Microsc. Microanal.* 20: 236–237.
94. Kuo P-C, Chen I-H, Chen C-T, Lee K-P, Chen C-W, Lin C-C, Chiu S. W.-Y., Hsieh Y-F, Wang Y-L, and Shiue J (2012) On-chip thin film Zernike phase plate for in-focus transmission electron microscopy imaging of organic materials. *ACS nano* 7: 465–470.
95. Marko M, Leith A, Hsieh C, and Danev R (2011) Retrofit implementation of Zernike phase plate imaging for cryo-TEM. *J. Struct. Biol.* 174: 400–412.
96. Dries M, Hettler S, Schulze T, Send W, Müller E, Schneider R, Gerthsen D, Luo Y, and Samwer K (2015) Thin-film-based phase plates for transmission electron microscopy fabricated from metallic glasses. *Microsc. Microanal.* 21: 1575–1576.
97. Walter A, Steltenkamp S, Rhinow D, and Kühlbrandt W (2015) Another phase plate in the zoo: reducing charging and optimizing the design of electrostatic phase plates. *Microsc. Microanal.* 21: 1941–1942.
98. Shiue J, Chang C-S, Huang S-H, Hsu C-H, Tsai J-S, Chang W-H, Wu Y-M, Lin Y-C, Kuo P-C, Huang Y-S, Hwu Y, Kai J-J, Tseng F-G, and Chen F-R (2009) Phase TEM for biological imaging utilizing a Boersch electrostatic phase plate: theory and practice. *J. Electron Microsc.* 58: 137–145.
99. Tamaki H, Kasai H, Harada K, Takahashi Y, and Nishi R (2013) Development of a contact-potential-type phase plate. *Microsc. Microanal.* 19: 1148–1149.

100. Walter A, Muzik H, Vieker H, Turchanin A, Beyer A, Gölzhäuser A, Lacher M, Steltenkamp S, Schmitz S, Holik P, Kühlbrandt W, and Rhinow D (2012) Practical aspects of Boersch phase contrast electron microscopy of biological specimens. *Ultramicroscopy* 116: 62–72.
101. Walter A, Steltenkamp S, Schmitz S, Holik P, Pakanavicius E, Sachser R, Huth M, Rhinow D, and Kühlbrandt W (2015) Towards an optimum design for electrostatic phase plates. *Ultramicroscopy* 153: 22–31.
102. Koeck P J (2018) Design of an electrostatic phase shifting device for biological transmission electron microscopy. *Ultramicroscopy* 187: 107–112.
103. Aharonov Y, and Bohm D (1959) Significance of electromagnetic potentials in the quantum theory. *Phys. Rev.* 115: 485.
104. Tanji T, Niimi H, Usukura J, Yamamoto Y, and Ohta S (2015) Electron differential phase microscopy with an a-b effect phase plate. *Microsc. Microanal.* 21: 1945–1946.
105. Edgcombe C J (2015) Evolution of magnetic ring designs for phase plates. *Microsc. Microanal.* 21: 2299–2230.
106. Xu M, Sohr E, Shevitski B, Glaeser R, and Muller H (2013) Development of a laser phase plate for Zernike phase contrast in electron microscopy. *Microsc. Microanal.* 19: 1146–1147.
107. Kapitza P, and Dirac P (1933) The reflection of electrons from standing light waves. *Math. Proc. Camb. Philos. Soc.* 29: 297.
108. Barwick B, and Batelaan H (2008) Aharonov–Bohm phase shifts induced by laser pulses. *New J. Phys.* 10: 083036.
109. Feist A, Bach N, da Silva N R, Danz T, Möller M, Priebe K E, Domröse T, Gatzmann J G, Rost S, Schauss J, Strauch S, Bormann R, Sivis M and Schäfer S (2017) Ultrafast transmission electron microscopy using a laser-driven field emitter: femtosecond resolution with a high coherence electron beam. *Ultramicroscopy* 176: 63–73.
110. Arbouet A, Caruso G M, and Houdellier F (2018) Chapter one – ultrafast transmission electron microscopy: historical development, instrumentation, and applications. In: Hawkes P W (ed.), *Advances in Imaging and Electron Physics, volume 207 of Advances in Imaging and Electron Physics*, pp 1–72 (Elsevier).
111. Schwartz O, Axelrod J J, Campbell S L, Turnbaugh C, Herman A, Planz E, Glaeser R M, and Muller H (2019) Laser-based phase contrast for transmission electron microscopy. *Microsc. Microanal.* 25: 982–983.
112. Hettler S, Gamm B, Dries M, Schultheiss K, Frindt N, Schröder R, Zach J, and Gerthsen D (2012) Electrostatic Zach phase plates: optimization of properties for applications. *Microsc. Microanal.* 18: 466–467.
113. Harada K, Kawaguchi A, Kotani A, Fujibayashi Y, Shimada K, and Mori S (2019) Hollow-cone Foucault imaging method. *Appl. Phys. Express* 12: 042003.
114. Buijsse B, van Laarhoven F, Schmid A, Cambie R, Cabrini S, Jin J, and Glaeser R (2016) A 'tulip aperture' providing in-focus phase-contrast. *Microsc. Microanal.* 18: 472–473.
115. Wang H-W, and Fan X (2019) Challenges and opportunities in cryo-em with phase plate. *Curr. Opin. Struct. Biol.* 58: 175–182.
116. Hettler S, Kano E, Dries M, Gerthsen D, Pfaffmann L, Bruns M, Beleggia M, and Malac M (2018) Charging of carbon thin films in scanning and phase-plate transmission electron microscopy. *Ultramicroscopy* 184: 252–266.
117. Nagayama K (2005) Phase contrast enhancement with phase plates in electron microscopy. *Adv. Imag. Electron Phys.* 138: 69–146.
118. Iijima H, Konyuba Y, Hosogi N, Ohkura Y, Jinnai H, and Higuchi T (2016) Contrast enhancement of long-range periodic structures using hole-free phase plate. *Microsc. Microanal.* 22: 60–61.
119. Konyuba Y, Iijima H, Hosogi N, Ishikawa I, Ohkura Y, and Abe Y (2015) Development of amorphous carbon thin film phase plate. *Microsc. Microanal.* 21: 1573–1574.
120. Minoda H, Yada A, Kawana Y, Iijima H, and Konyuuba Y (2013) Development of a new type of thin film phase plate and its application for in-situ observation. *Microsc. Microanal.* 19: 478–479.
121. Egerton R F (2011) *Electron Energy Loss Spectroscopy in Electron Microscope*. Springer New York Dordrecht Heidelberg London.
122. Nagayama K (2008) Development of phase plates for electron microscopes and their biological application. *Eur. Biophys. J.* 37: 345–358.
123. Nagayama K, Danev R, Shigematsu H, Kayama Y, Okawara H, Ohara M, Itoh T, Sugitani S, and Kitayama A (2010) Phase plates free from contaminant charging. *Microsc. Microanal.* 16: 516–517.
124. Striemer C, Gaborski T, Roussie J, Hsieh C, Meng X, and Marko M (2012) Microfabricated Zernike phase plates for cryo-TEM. *Microsc. Microanal.* 18: 490–491.
125. Marko M, Meng X, Hsieh C, Kishchenko G, and Leith A (2014) Evaluation of the quality of Zernike phase plates. *Microsc. Microanal.* 20: 212–213.
126. Konyuba Y, Iijima H, Abe Y, Suga M, and Ohkura Y (2014) High throughput fabrication process of a Zernike phase plate. *Microsc. Microanal.* 20: 222–223.
127. Marko M, Hsieh C, Leith E, Mastronarde D, and Motoki S (2016) Practical experience with hole-free phase plates for cryo electron microscopy. *Microsc. Microanal.* 22: 1316–1328.
128. Marko M, and Leith A (2012) Automatic phase-plate centering for cryo-TEM. *Microsc. Microanal.* 18: 486–487.
129. Kurth P, Pattai S, and Irsen S H (2012) Modular nano-positioning system for phase plates. *Microsc. Microanal.* 18: 504–505.
130. Cowley J (1986) Electron diffraction phenomena observed with a high resolution stem instrument. J. Electron Microsc. Tech. 3 25–44.
131. Fukuda Y, Laugks U, Lučić V, Baumeister W, and Danev R (2015) Electron cryotomography of vitrified cells with a Volta phase plate. *J. Struct. Biol.* 190: 143–154.
132. Danev R (2017) Biological sciences tutorial: cryo-EM with phase plates. *Microsc. Microanal.* 23: 1398–1399.
133. Marko M, Hsieh C, Leith E, Mastronarde D, and Motoki S (2016) Practical experience with hole-free phase plates for cryo electron microscopy. *Microsc. Microanal.* 22: 1316–1328.
134. Danev R, Tegunov D, and Baumeister W (2017) Using the Volta phase plate with defocus for cryo-em single particle analysis. *Elife* 6: e23006.
135. Gamm B, Schultheiss K, Gerthsen D, and Schroder R R (2007) Optimisation of phase contrast in a transmission electron microscope with a physical phase plate and CS-corrector. *Microsc. Microanal.* 13: 10–11.
136. Malac M, Bergen M, Egerton R, Kawasaki M, Beleggia M, Furukawa H, and Shimizu M (2012) Practical hole-free phase plate imaging: principles, advantages and pitfalls. *Microsc. Microanal.* 18: 484–485.
137. Hettler S, Onodab J, Wolkow R, Pitters J, and Malac M (2019) Charging of electron beam irradiated amorphous carbon thin films at liquid nitrogen temperature. *Ultramicroscopy* 196: 161–166.
138. Malac M, Beleggia M, Egerton R, Kawasaki M, Bergen M, Okura Y, Ishikawa I, and Motoki K (2014) Charging of thin film phase plates under electron beam irradiation. *Microsc. Microanal.* 20: 230–231.
139. Malac M, Beleggia M, Rowan T, Egerton R, Kawasaki M, Okura Y, and McLeod R A (2015) Electron beam-induced charging and modifications of thin films. *Microsc. Microanal.* 21: 1385–1386.
140. Danov K, Danev R, and Nagayama K (2002) Reconstruction of the electric charge density in thin films from the contrast transfer function measurements. *Ultramicroscopy* 90: 85–95.
141. Danov K, Danev R, and Nagayama K (2001) Electric charging of thin films measured using the contrast transfer function. *Ultramicroscopy* 87: 45–54.
142. Egerton R F (2012) Mechanisms of radiation damage in beam-sensitive specimens, for TEM accelerating voltages between 10 and 300 kv. *Microsc. Res. Techn.* 75: 1550–1556.
143. Harada K, Shimada K, Niitsu K, Katsuta T, Ohno T, and Shindo D (2017) Transmission electron microscope observation of charge distribution on insulating thin films by hydro-carbon deposition. *Microsc. Microanal.* 23: 1826–1827.
144. Ennos A (1953) The origin of specimen contamination in the electron microscope. *British J. Appl. Phys.* 4: 101.

145. Hren J (1978) Specimen contamination in analytical electron microscopy: sources and solutions. *Ultramicroscopy* 3: 375–380.
146. Mitchell D R (2015) Contamination mitigation strategies for scanning transmission electron microscopy. *Micron* 73: 36–46.
147. Pretzsch R, Dries M, Hettler S, Spiecker M, Obermair M, and Gerthsen D (2019) Investigation of hole-free phase plate performance in transmission electron microscopy under different operation conditions by experiments and simulations. *Adv. Struct. Chem. Imag.* 5: 5.
148. Ennos A E (1954) The sources of electron-induced contamination in kinetic vacuum systems. *Brit. J. Appl. Phys.* 5: 27–31.
149. Fourie J T (1978) High contamination rates from strongly adsorbed hydrocarbon molecules and a suggested solution. *Optik* 52: 91–95.
150. Kumao A, Hashimoto H, and Shiraishi K (1981) Studies on specimen contamination by transmission electron microscopy. *J. Electron. Microsc.* 30: 161–170.
151. Wall J (1980) Contamination in the stem at ultra high vacuum. Scanning electron microscopy (1980) 99–106.
152. Ramsier R D, and Yates J T (1991) Electron-stimulated desorption: principles and applications. *Surf. Sci. Rep.* 12: 243–378.
153. van Dorp W F, Hansen T W, Wagner J B, and De Hosson J T (2013) The role of electron-stimulated desorption in focused electron beam induced deposition. *Beilstein J. Nanotech.* 4: 474–480.
154. Amman M, Sleight J, Lombardi D, Welser R, Deshpande M, Reed M, and Guido L (1996) Atomic force microscopy study of electron beam written contamination structures. *J. Vac. Sci. Technol. B: Microelectron. Nanometer Struct. Process. Meas. Phenom.* 14: 54–62.
155. Isabell T C, Fischione P E, O'Keefe C, Guruz M U, and Dravid V P (1999) Plasma cleaning and its applications for electron microscopy. *Microsc. Microanal.* 5: 126–135.
156. Hoyle D, Malac M, Trudeau M, and Woo P (2011) UV treatment of TEM/STEM samples for reduced hydrocarbon contamination. *Microsc. Microanal.* 17: 1026–1027.
157. Egerton R, and Rossouw C (1976) Direct measurement of contamination and etching rates in an electron beam. *J. Phys. D: Appl. Phys.* 9: 659.
158. Hirsch P, Kassens M, Puttmann M, and Reimer L (1994) Contamination in a scanning electron microscope and the influence of specimen cooling. *Scanning* 16(2): 101–110.
159. Egerton R F, Li P, and Malac M (2004) Radiation damage in the TEM and SEM. *Micron* 35: 399–409.
160. Broers A, Molzen W, Cuomo J, and Wittels N (1976) Electron-beam fabrication of 80-å metal structures. *Appl. Phys. Lett.* 29: 596–598.
161. Tanaka M, Shimojo M, Mitsuishi K, and Furuya K (2004) The size dependence of the nano-dots formed by electron-beam-induced deposition on the partial pressure of the precursor. *Appl. Phys. A* 78: 543–546.
162. Malac M, Egerton R, Freeman M, Lau J, Zhu Y, and Wu L (2005) Electron-beam patterning with sub-2 nm line edge roughness. *J. Vac. Sci. Technol. B* 23: 271–273.
163. Van Dorp W, and Hagen C W (2008) A critical literature review of focused electron beam induced deposition. *J. Appl. Phys.* 104: 10.
164. Cambie R, Downing K H, Typke D, Glaeser R M, and Jin J (2007) Design of a microfabricated, two-electrode phase-contrast element suitable for electron microscopy. *Ultramicroscopy* 107: 329–339.
165. Nagayama K, Danev R, Shigematsu H, Kayama Y, Okawara H, Ohara M, Itoh T, Sugitani S, and Kitayama A (2010) Phase plates free from contaminant charging. *Microsc. Microanal.* 16: 516–517.
166. Egerton R, McLeod R A, Wang F, and Malac M (2010) Basic questions related to electron-induced sputtering in the TEM. *Ultramicroscopy* 110: 991–997.
167. Sharman C (1929) Secondary electron emission from solid metal surfaces. *Math. Proc. Camb. Philos. Soc.* 25: 237–254.
168. Seiler H (1984) Secondary electron emission. In: *Electron Beam Interactions with Solids*, pp 33–42 (Scanning Electron Microscopy, Inc.).
169. Reimer L (1998) *Scanning Electron Microscopy; Physics of Image Formation and Microanalysis*.
170. Howe J, Hoyle D, Ueda K, Dogel S, Hosseinkhannazer H, Reynolds M, Veillette R, Trudeau M L, and Joy D (2015) Secondary electron yield at high voltages up to 300 kev. *Microsc. Microanal.* 21: 1705–1706.
171. Bauer M, and Aeschlimann M (2002) Dynamics of excited electrons in metals, thin films and nanostructures. *J. Electron Spectrosc. Relat. Phenom.* 124: 225–243.
172. Roth F, Arion T, Kaser H, Gottwald A, and Eberhardt W (2018) Angle resolved photoemission from Ag and Au single crystals: final state lifetimes in the attosecond range. *J. Electron Spectrosc. Relat. Phenom.* 224: 84–92.
173. Burgi L, Brune H, Jeandupeux O, and Kern K (2000) Quantum coherence and lifetimes of surface-state electrons. *J. Electron Spectrosc. Relat. Phenom.* 109: 33–49.
174. Glaeser R M, and Downing K H (2004) Specimen charging on thin films with one conducting layer: discussion of physical principles. *Microsc. Microanal.* 10: 790–796.
175. Cazaux J (1995) Correlations between ionization radiation damage and charging effects in transmission electron microscopy. *Ultramicroscopy* 60: 411–425.
176. Cazaux J (1999) Mechanisms of charging in electron spectroscopy. *J. Electron Spectrosc. Relat. Phenom.* 105: 155–185.
177. Cazaux J (2006) e-induced secondary electron emission yield of insulators and charging effects. *Nucl. Instr. Meth. Phys. Res. Sec. B: Beam Interact. Mater. Atoms* 244: 307–322.
178. Cazaux J (1986) Some considerations on the electric field induced in insulators by electron bombardment. *J. Appl. Phys.* 59: 1418–1430.
179. Cazaux J (2010) Secondary electron emission and charging mechanisms in auger electron spectroscopy and related e-beam techniques. *J. Electron Spectrosc. Relat. Phenom.* 176: 58–79.
180. Cazaux J (2008) On some contrast reversals in SEM: application to metal/insulator systems. *Ultramicroscopy* 108: 1645–1652.
181. Baragiola , R A (2012). *Ionization of Solids by Heavy Particles*, volume 306: (Springer Science & Business Media).
182. Cazaux J (1986) Some considerations on the electric field induced in insulators by electron bombardment. *J. Appl. Phys.* 59: 1418–1430.
183. Cazaux J (1999) Some considerations on the secondary electron emission, δ, from e- irradiated insulators. *J. Appl. Phys.* 85: 1137–1147.
184. Cazaux J (2008) About the secondary electron emission from solid hydrogens: H2, hd, d2 and t2. *J. Electron Spectrosc. Relat. Phenom.* 162: 36–43.
185. Cazaux J, and Lehuede P (1992) Some physical descriptions of the charging effects of insulators under incident particle bombardment. *J. Electron Spectrosc. Relat. Phenom.)* 59: 49–71.
186. Cazaux J (2010a) Secondary electron emission and fundamentals of charging mechanisms in XPS. *J. Electron Spectrosc. Relat. Phenom.* 178: 357–372.
187. Cazaux J (2010b) Secondary electron emission and charging mechanisms in auger electron spectroscopy and related e-beam techniques. *J. Electron Spectrosc. Relat. Phenom.* 176: 58–79.
188. Egerton R F, and Malac M (2004) The lateral range and energy deposition of fast secondary electrons. *Microsc. Microanal.* 10: 1382–1383.
189. Brink J, Sherman M, Berriman J, and Chiu W (1998) Evaluation of charging on macro- molecules in electron cryomicroscopy. *Ultramicroscopy* 72: 41–52.
190. Downing K H, McCartney M, and Glaeser R M (2004) Experimental characterization and mitigation of specimen charging on thin films with one conducting layer. *Microsc. Microanal.* 10: 783–789.
191. Glaeser R (2016) Specimen behavior in the electron beam. *Meth. Enzymol.* 579: 19–50.
192. Russo C J, and Henderson R (2018) Charge accumulation in electron cryomicroscopy. *Ultramicrosc.* 187: 43–49.

193. Glaeser R M, and Downing K H (2004) Specimen charging on thin films with one conducting layer: discussion of physical principles. *Microsc. Microanal.* 10: 790–796.
194. Cazaux J (2004) Scenario for time evolution of insulator charging under various focused electron irradiations. *J. Appl. Phys.* 95: 731–742.
195. Brink J, Sherman M B, Berriman J, and Chiu W (1998) Evaluation of charging on macromolecules in electron cryomicroscopy. *Ultramicroscopy* 72: 41–52.
196. Chiu F-C (2014) A review on conduction mechanisms in dielectric films. *Adv. Mater. Sci. Eng.* 2014: 1687–8434.
197. Dries M, Janzen R, Schulze T, Schundelmeier J, Hettler S, Golla-Schindler U, Jaud B, Kaiser U, and Gerthsen D (2016) The role of secondary electron emission in the charging of thin-film phase plates. *Microsc. Microanal.* 22: 64–65.
198. Danev R, Iijima H, Matsuzaki M, and Motoki S (2019) Fast and accurate defocus for improved tunability of cryo-EM experiments. *IUCrJ* 7: 566–574.
199. Heras J, Estiú G, and Viscido L (1997) The interaction of water with clean palladium films: a thermal desorption and work function study. *Appl. Surf. Sci.* 108: 455–464.
200. Heras J M, and Viscido L (1980) Work function changes upon water contamination of metal surfaces. *Appl. Surf. Sci.* 4: 238–241.
201. Thiel P A, and Madey T E (1987) The interaction of water with solid surfaces: fundamental aspects. *Surf. Sci. Rep.* 7: 211–385.
202. Heras J M, Estiú G, and Viscido L (1990) Annealing behaviour of clean and oxygen covered polycrystalline palladium films: a work function and electrical resistance study. *Thin Solid Films* 188: 165–172.
203. Henderson M A (2002) The interaction of water with solid surfaces: fundamental aspects revisited. *Surf. Sci. Rep.* 46: 1–308.
204. Egerton R (2014) Choice of operating voltage for a transmission electron microscope. *Ultramicroscopy* 145: 85–93.
205. Hayashida M, Malac M, Bergen M, and Li P (2014) Nano-dot markers for electron tomography formed by electron beam-induced deposition: nanoparticle agglomerates application. *Ultramicroscopy* 144: 50–57.
206. Yip K M, Fischer N, Paknia E, Chari A, and Stark H (2020) Breaking the next cryo-em resolution barrier-atomic resolution determination of proteins!, BioRxiv.
207. Kato T, Makino F, Nakane T, Terahara N, Kaneko T, Shimizu Y, Motoki S, Ishikawa I, Yonekura K, and Namba K (2019) Cryotem with a cold field emission gun that moves structural biology into a new stage. *Microsc. Microanal.* 25: 998–999.
208. Ando T, Taniguchi Y, Takai Y, Kimura Y, Shimizu R, and Ikuta T (1994) Development of real-time defocus-modulation-type active image processing (DMAIP) for spherical-aberration-free TEM observation. *Ultramicroscopy* 54: 261–267.
209. Danev R, Yanagisawa H, and Kikkawa M (2019) Cryo-electron microscopy methodology: current aspects and future directions. *Trends Biochem. Sci.* 44: 837–848.
210. Hosogi N, Sen A, and Iijima H (2015) Comparison of cryo TEM images obtained with zernike and hole-free phase plates. *Microsc. Microanal.* 21: 1389–1390.
211. Hosogi N, Shigematsu H, Terashima H, Homma M, and Nagayama K (2011) Zernike phase contrast cryo-electron tomography of sodium-driven flagellar hook-basal bodies from vibrio alginolyticus. *J. Struct. Biol.* 173: 67–76.
212. Danev R, and Nagayama K (2008) Single particle analysis based on Zernike phase contrast transmission electron microscopy. *J. Struct. Biol.* 161: 211–218.
213. Shigematsu H, Sokabe T, Danev R, Tominaga M, and Nagayama K (2010) A 3.5-nm structure of rat trpv4 cation channel revealed by Zernike phase-contrast cryoelectron microscopy. *J. Biol. Chem.* 285: 11210–11218.
214. Fukuda Y, Fukazawa Y, Danev R, Shigemoto R, and Nagayama K (2010) Application of Zernike phase-contrast electron microscopy for vitrified complex biological specimens. *Microsc. Microanal.* 16: 556–557.
215. Wright E R, Guerrero-Ferreira R C, Kiss G, Strauss J D, and Hampton C M (2014) Zernike phase contrast cryo-electron tomography of bacteria and viruses. *Microsc. Microanal.* 20: 204–205.
216. Chiu W, Rochat R, Liu X, Murata K, Khant H, Nagayama K, and Rixon F (2012) Zernike phase contrast cryo-electron microscopy of virus particles. *Microsc. Microanal.* 18: 462–463.
217. Typke D (2010) Zernike phase contrast electron microscopy with a spherically corrected foil lens. *Microsc. Microanal.* 16: 441–444.
218. Motoki S, Fukuda T, Suga H, Okura Y, Danev R, Brink J, and Armbruster B (2010) Design evolution of the Zernike phase contrast transmission electron microscope. *Microsc. Microanal.* 16: 530–531.
219. Frindt N, Hettler S, Oster M, Gamm B, Dries M, Schultheiss K, Gerthsen D, and Schröder R (2012) Tunable phase contrast of vitrified macromolecular complexes by an obstruction minimized electrostatic phase plate. *Microsc. Microanal.* 18: 468–469.
220. Shimada A, Niwa H, Tsujita K, Suetsugu S, Nitta K, Hanawa-Suetsugu K, Akasaka R, Nishino Y, Toyama M, Chen L, Liu Z-J, Wang B-C, Yamamoto M, Terada T, Miyazawa A, Tanaka A, Sugano S, Shirouzu M, Nagayama K, Takenawa T and Yokoyama S (2007) Curved EFC/F-BAR-domain dimers are joined end to end into a filament for membrane invagination in endocytosis. *Cell* 129: 761–772.
221. Yui H, Minamikawa H, Danev R, Nagayama K, Kamiya S, and Shimizu T (2008) Growth process and molecular packing of a self-assembled lipid nanotube: phase-contrast transmission electron microscopy and XRD analyses. *Langmuir* 24: 709–713.
222. Furuhata M, Danev R, Nagayama K, Yamada Y, Kawakami H, Toma K, Hattori Y, and Maitani Y (2008) Decaarginine-PEG-artificial lipid/DNA complex for gene delivery: nanostructure and transfection efficiency. *J. Nanosci. Nanotechnol.* 8: 2308–2315.
223. Danev R, and Nagayama K (2008) Single particle analysis based on Zernike phase contrast transmission electron microscopy. *J. Struct. Biol.* 161: 211–218.
224. Yamaguchi M, Danev R, Nishiyama K, Sugawara K, and Nagayama K (2008) Zernike phase contrast electron microscopy of ice-embedded influenza a virus. *J. Struct. Biol* 162: 271–276.
225. Danev R (2001) N. K. Transmission electron microscopy with Zernike phase plate. *Ultramicroscopy* 88: 243–252.
226. Inayoshi Y, and Minoda H (2011) First direct observation of biological molecules in liquid by environmental phase contrast transmission electron microscopy. *Microsc. Microanal.* 17: 530–531.
227. Inayoshi Y, and Minoda H (2012) Bio-imaging in liquid using environmental phase plate transmission electron microscopy. *Microsc. Microanal.* 18: 1138–1139.
228. Murata K, Liu X, Danev R, Jakana J, Schmid M F, King J, Nagayama K, and Chiu W (2010) Zernike phase contrast cryo-electron microscopy and tomography for structure determination at nanometer and sub- nanometer resolutions. *Structure* 18: 903–912.
229. Fukuda Y, and Nagayama K (2012) Zernike phase contrast cryo-electron tomography of whole mounted frozen cells. *J. Struct. Biol.* 177: 484–489.
230. Guerrero-Ferreira R C, and Wright E R (2014) Zernike phase contrast cryo-electron tomography of whole bacterial cells. *J. Struct. Biol.* 185: 129–133.
231. Danev R, Kanamaru S, Marko M, and Nagayama K (2010) Zernike phase contrast cryo-electron tomography. *J. Struct. Biol.* 171: 174–181.
232. Danev R, and Nagayama K (2006) Applicability of thin film phase plates in biological electron microscopy. *Biophysics* 2: 35–43.
233. Fukuda Y, Asano S, Laugks U, Beck F, Aufderheide A, Forster F, Lucic V, Baumeister W, and Danev R (2015) In situ studies of cellular architecture by electron cryo-tomography with Volta phase plate. *Microsc. Microanal.* 21: 1835–1836.

234. Marko M, Hsieh C, Leith A, and Mannella C (2010) Requirements for phase-plate cryo-electron tomography. *Microsc. Microanal.* 16: 546–547.
235. Marko M, Hsieh C-E, Dunn K, Typke D, Mannella C, and Frank J (2005) Use of the Zernike phase plate for electron tomography of frozen-hydrated specimens. *Microsc. Microanal.* 11: 310–311.
236. Marko M (2007) Universal phase-plate imaging for cryo-electron tomography. Microsc. Microanal. 13: 1212–1213.
237. Wright E R, and Guerrero-Ferreira R C (2013) Developments in the application of Zernike phase contrast technologies to cryo-electron tomography studies of bacteria. *Microsc. Microanal.* 19: 548–549.
238. Fukuda Y, Danev R, and Nagayama K (2012) Application of Zernike phase-contrast electron microscopy and electron tomography for frozen hydrated complex biological specimens. *Microsc. Microanal.* 18: 498–499.
239. Danev R, Kanamaru S, Marko M, and Nagayama K (2010) Zernike phase contrast cryo-electron tomography. *J. Struct. Biol.* 171: 174–181.
240. Hosogi N, Shigematsu H, Terashima H, Homma M, and Nagayama K (2010) Zernike phase contrast cryo-electron tomography of flagellar hook-basal bodies from vibrio alginolyticus. *Microsc. Microanal.* 16: 558–559.
241. Sui H, Kishchenko G, Danev R, He J, Fisher R, Hsieh C, and Marko M (2014) Artifact correction for Zernike phase-plate cryo-electron tomography. *Microsc. Microanal.* 20: 234–235.
242. Danev R, and Nagayama K (2010) Phase plates for transmission electron microscopy. In: *Methods in enzymology*, volume 481, pp 343–369, (Elsevier).
243. Kurth P, Pattai S, Rudolph D, Overbuschmann J, Wamser J, and Irsen S (2014) Artifact-free, long-lasting phase plate. *Microsc. Microanal.* 20: 220–221.
244. Danev R, and Nagayama K (2010) Fringing and strong object effects with the phase plate. *Microsc. Microanal.* 16: 528–529.
245. Dries M, Gamm B, Schultheiss K, Rosenauer A, Schröder R, and Gerthsen D (2010) Object-wave reconstruction by carbon film-based Zernike- and Hilbert-phase plate microscopy: a theoretical study not restricted to weak-phase objects. *Microsc. Microanal.* 16: 552–553.
246. Danev R, Khoshouei M, and Baumeister W (2016) Single particle analysis with the Volta phase plate. *Microsc. Microanal.* 22: 82–83.
247. Danev R, Khoshouei M, and Baumeister W (2019) Single particle imaging with the Volta phase plate. *Microsc. Microanal.* 25: 7–8.
248. Zhou Z H, Hui W H, Zhang J, Atanasov I, Celma C C, and Roy P (2016) In situ structure of viral rna by cryo electron tomography with Volta phase plate, energy filtering and direct electron counting. *Microsc. Microanal.* 22: 74–75.
249. Khoshouei M, Danev R, Gerisch G, Ecke M, Plitzko J, and Baumeister W (2014) Phase contrast cryo-electron tomography and single particle analysis with a new phase plate. *Microsc. Microanal.* 20: 232–233.
250. Fukuda Y, Beck F, Nagy I, Danev R, and Baumeister W (2017) Exploring cellular morphology of thermoplasma acidophilum by cryo-electron tomography with Volta phase plate. *Microsc. Microanal.* 23: 1234–1235.
251. Khoshouei M, Gerisch G, Ecke M, Ortiz J, Plitzko J M, Danev R, and Baumeister W (2015) Combination of different techniques in cryo-electron tomography with a Volta phase plate. *Microsc. Microanal.* 21: 1393–1394.
252. Barton B, and Schroder R (2007) Electron tomography of unstained cell sections using a half-plane (Hilbert) phase plate. *Microsc. Microanal.* 13: 1312–1313.
253. Bart B, Piet T, Veli A, Radostin D, and Robert G (2020) Spectral DQE of the Volta phase plate. *Ultramicrosc.* 218: 113079.
254. von Loeffelholz O, Papai G, Danev R, Myasnikov A G, Natchiar S K, Hazemann I, Ménétret J-F, and Klaholz B P (2018) Volta phase plate data collection facilitates image processing and cryo-em structure determination. *J. Struct. Biol* 202: 191–199.
255. Li K, Sun C, Klose T, Irimia-Dominguez J, Vago F S, Vidal R, and Jiang W (2019) Sub-3å apoferritin structure determined with full range of phase shifts using a single position of Volta phase plate. *J. Struct. Biol* 206: 225–232.
256. Chen F-R, Tsai C-Y, Wu W-J, Dyck D V, Tsai J-S, Huang T-W, Chuang Y-J, Tseng F, and Chang C-S (2012) New phase microscopy for advanced soft materials imaging using tunable Boersch electrostatic phase plate. *Microsc. Microanal.* 18: 470–471.
257. Bammes B, Spilman M, Streetley J, and Bhella D (2019) Initial results from the cryoarm300 and de-64 counting. *Microsc. Microanal.* 25: 1000–1001.
258. Pollard S, Malac M, Beleggia M, Kawasaki M, and Zhu Y (2013) Magnetic imaging with a Zernike-type phase plate in a transmission electron microscope. *Appl. Phys. Lett.* 102: 192401.
259. Kotani A, Harada K, Malac M, Nakajima H, Kurushima K, and Mori S (2019) Magnetic textures in a hexaferrite thin film and their response to magnetic fields revealed by phase microscopy. *Japanese J. Appl. Phys.* 58: 065004.
260. Qian H, Furukawa H, Shimizu M, Kawasaki M, and Shiojiri M (2012) Study for automated imaging with phase plate electron microscopy and suggestions for the future instrumentation. *Microsc. Microanal.* 18: 500–501.
261. Homeniuk D, Malac M, and Hayashida M (2018) Wavelet transform-based electron tomography measurement of buried interface roughness. *Ultramicroscopy* 194: 64–77.
262. Tosaka M, Danev R, and Nagayama K (2005) Application of phase contrast transmission microscopic methods to polymer materials. *Macromol.* 38: 7884–7886.
263. Malac M, Motoki S, Konyuba Y, Okura Y, Ishikawa I, Iijima H, Hosogi N, Hayashida M, and Jinnai H (2019) Applications of hole-free phase plate: imaging of block copolymers.
264. Lichte H, and Lehmann M (2007) Electron holography—basics and applications. *Rep. Prog. Phys.* 71: 016102.
265. Koch C T, and Lubk A (2010) Off-axis and inline electron holography: a quantitative comparison. *Ultramicroscopy* 110: 460–471.
266. Kirkland E J (1984) Improved high resolution image processing of bright field electron micrographs. *Ultramicroscopy* 15: 151–172.
267. Cowley J M (1992) Twenty forms of electron holography. *Ultramicroscopy* 41: 335–348.
268. Coene W, Thust A, op de Beeck M, and van Dyck D (1996) Maximum-likelihood method for focus-variation image reconstruction in high resolution transmission electron microscopy. *Ultramicroscopy* 64: 109–135.
269. Bajt S, Barty A, Nugent K, McCartney M, Wall M, and Paganin D (2000) Quantitative phase-sensitive imaging in a transmission electron microscope. *Ultramicroscopy* 83: 67–73.
270. Hsieh W-K, Chen F-R, Kai J-J, and Kirkland A (2004) Resolution extension and exit wave reconstruction in complex HREM. *Ultramicroscopy* 98: 99–114.
271. Koch C T (2008) A flux-preserving non-linear inline holography reconstruction algorithm for partially coherent electrons. *Ultramicroscopy* 108: 141–150.
272. Nagayama K (1999) Complex observation in electron microscopy. i. basic scheme to surpass the scherzer limit. *J. Phys. Soc. Jpn.* 68: 811–822.
273. Danev R, and Nagayama K (2001) Complex observation in electron microscopy. ii. Direct visualization of phases and amplitudes of exit wave functions. *J. Phys. Soc. Jpn.* 70: 696–702.
274. Van Dyck D (2010) Wave reconstruction in TEM using a variable phase plate. *Ultramicroscopy* 110: 571–572.
275. Gamm B, Dries M, Schultheiss K, Blank H, Rosenauer A, Schröder R, and Gerthsen D (2010) Wave-function reconstruction by phase-plate transmission electron microscopy. *Microsc. Microanal.* 16: 538–539.
276. Schultheiss K, Zach J, Gamm B, Dries M, Frindt N, Schröder R, and Gerthsen D (2010) New electrostatic phase plate for transmission

electron microscopy and its application for wave-function reconstruction. *Microsc. Microanal.* 16: 536–537.

277. Hettler S, Wagner J, Dries M, and Gerthsen D (2014) Inelastic phase contrast using electrostatic Zach phase plates. *Microsc. Microanal.* 20: 216–217.
278. Hettler S, Dries M, Schulze T, Oster M, Wacker C, Schroder R R, and Gerthsen D (2015) High-resolution transmission electron microscopy with Zach phase plate. *Microsc. Microanal.* 21: 1581–1582.
279. Hettler S, Wagner J, Dries M, Oster M, Schröder R, and Gerthsen D (2014) Application of zach phase plates for phase-contrast transmission electron microscopy: status and future experiments. *Microsc. Microanal.* 20: 214–215.
280. Obermair M, Hettler S, Dries M, and Gerthsen D (2017) Electrostatic Zach phase plates for transmission electron microscopy: status and future investigations. *Microsc. Microanal.* 23: 828–829.
281. Spilman M S, Guo H, Bammes B E, Jin L, and Bilhorn R B (2015) Boosting contrast of cryo-EM images without a phase plate. *Microsc. Microanal.* 21: 911–912.
282. Murata K, Miyazaki N, and Nagayama K (2015) Zernike phase contrast electron microscopy: observation of the image formation and improvement of the image quality using direct detector. *Microsc. Microanal.* 21: 2141–2142.
283. Alloyeau D, Hsieh W, Anderson E, Benner G, Gomez E, Balsara N, and Kisielowski C (2009) New developments in phase contrast transmission electron microscopy with electrostatic phase plate. *Microsc. Microanal.* 15: 1086–1087.
284. Muller H, Gerheim V, Zach J, and Haider M (2012) A quadrupole optics with large aspect ratio for an anamorphotic electrostatic phase plate without beam blocking. *Microsc. Microanal.* 18: 494–495.
285. Sugita Y, Kawaoka Y, Noda T, and Wolf M (2016) Structure of the Ebola virus nucleocapsid core by single particle cryo-electron microscopy. *Microsc. Microanal.* 22: 66–67.
286. Sugita Y, Matsunami H, Kawaoka Y, Noda T, and Wolf M (2018) Cryo-EM structure of the Ebola virus nucleoprotein RNA complex at 3.6 Å resolution. *Nature* 563: 137–140.
287. Schofield M, Beleggia M, Zhu Y, and Pozzi G (2008) Characterization of Jeol 2100f Lorentz-TEM for low-magnification electron holography and magnetic imaging. *Ultramicroscopy* 108: 625–634.
288. Hayashida M, Najarian A M, McCreery R, and Malac M (2018) Hole free phase plate electron tomography in material sciences. *Microsc. Microanal.* 24: 2224–2225.
289. Malac M, Kano E, Hayashida M, Kawasaki M, Motoki S, Egerton R, Ishikawa I, Okura Y, and Beleggia M (2017) Hole-free phase plate energy filtering imaging of graphene: toward quantitative hole-free phase plate imaging in a TEM. *Microsc. Microanal.* 23: 842–843.